

Process Design for the Forming of Organically Coated Sheet Metal

Von der Fakultät Maschinenbau
der Technischen Universität Dortmund
zur Erlangung des Grades
Doktor-Ingenieur
vorgelegte Dissertation

von
Ha-Duong Pham

aus
Hanoi, Vietnam

April 2011

Berichter: Prof. Dr.-Ing. A. Erman Tekkaya
Mitberichter: Prof. Dr.-Ing. Werner Homberg
Tag der mündlichen Prüfung: 31. Mai 2011

Acknowledgements

I am indebted to many people for their long-lasting support and encouragement which was invaluable for the successful completion of this research work.

Firstly, I would like to gratefully acknowledge the German Academic Exchange Service (DAAD) for their financial support. I would also like to thank Mrs. Elke Burbach and other DAAD staff members, who have been beside me during my stay in Germany.

I wish to express my deepest appreciation to Prof. Dr.-Ing. Matthias Kleiner for granting me the opportunity to work with the Institute of Forming Technology and Lightweight Construction (IUL).

I also wish to express my deepest gratitude to Prof. Dr.-Ing. A. Erman Tekkaya for giving me the chance to work under his supervision as well as for his kindness and patience during the many years of my research work.

Furthermore, I would like to extend my sincerest thanks to Prof. Dr.-Ing. Werner Homberg. He was always available, whenever I needed help.

My research work was also supervised by Dr.-Ing. Michael Trompeter, to whom I wish to express my sincerest gratitude for his never-ending enthusiasm and guidance. Under his instruction, I have developed many useful research skills and he was always available, kind and supportive when I needed help from him.

To Mrs. Gabriele Bach I would also like to express my warmest appreciation for her help in acquiring my family reunion visa. Without her help, my wife and my daughter would not have been allowed to join me in Germany in 2008.

My sincere thanks also go to Dr.-Ing. Marco Schikorra, Jun. Prof. Dr.-Ing. Alexander Brosius, Dr.-Ing. Hossein Karbasian, Mr. Jörg Witulski, Mr. Gerd Sebastiani, Mr. Tim Cwiekala for helping me with the FEM simulation at the beginning of my work. I also greatly thank all my colleagues for their kind direct or indirect co-operation and help which created an excellent working atmosphere. I am also indebted to all technicians – Mr. Ulrich Wornalkiewicz, Mr. Werner Feurer, Mr. Dirk Hoffmann, Mr. Andreas Herdt, and Mr. Frank Volk – for their coordinative technical support in my experiments. I am also sincerely grateful to Ms. Andrea Hallen for her valuable proofreading.

On the Vietnamese side, I specially thank Prof. Dr.-Ing. Nguyen Tat Tien, Dr.-Ing. Nguyen Dac Trung who enthusiastically encouraged me to apply for the DAAD grant. I also greatly appreciate the assistance from my friend in Germany - Dr.-Ing. Nguyen Nhu Huynh.

Almost last, but by no means least, I would like to express my hearty gratitude towards my parents in Vietnam for their care, love and support during my quite long stay in Germany.

Finally, my special hearty appreciation goes to my wife and my daughter for their support, patience and loving understanding all the time.

Dortmund, April 2011

Ha-Duong Pham

Kurzzusammenfassung

Titel: Prozessauslegung zur Umformung von organisch beschichteten Blechen

Der Einsatz organisch beschichteter Bleche hat viele Vorteile im Vergleich zu konventionellen Blechhalbzeugen, wie z.B. die Reduzierung der Anzahl der notwendigen Fertigungsschritte, die Verringerung der Produktionskosten und die Vermeidung umweltbelastender Lackierbearbeitungsschritte. Während der Umformung verändern sich die Eigenschaften der dünnen und relativ weichen Beschichtung abhängig von den Umformbedingungen, wie z.B. Werkzeugradialen sowie Reibungskoeffizient zwischen dem Blech und dem Werkzeugsystem. Bei großen Formänderungen des Blechwerkstoffs kann es beispielsweise zu einer Änderung der Oberflächentopografie des Substrates führen. Dies kann bis zu einer Beschädigung der Beschichtung und somit zu einem Versagen des Produktes führen. Daher ist es wesentlich, die Formänderungsgrenzen der Beschichtung zu kennen, um die ursprüngliche Funktionalität der Beschichtung, beispielsweise die optischen Eigenschaften und den Korrosionsschutz, nach der Umformoperation zu erhalten. Das bedeutet, dass unerwünschte Defekte wie bzw. eine Rissbildung oder eine Delamination der Schicht vom Substrat durch die Anwendung geeigneter Umformverfahren und durch die Ermittlung optimaler Prozessparameter vermieden werden müssen. Hierzu ist eine Methodik zur Prognose der Änderung der funktionalen Schichteigenschaften in Abhängigkeit von Formänderungszuständen notwendig.

In dieser Arbeit wird die Umformung von organisch beschichteten Blechen grundlegend untersucht. Zunächst werden experimentelle Untersuchungen zur Umformbarkeit organisch beschichteter Bleche durchgeführt und der Einfluss der Prozessparameter auf die Produkteigenschaften (insbesondere des Glanzgrades) von organisch beschichteten Blechformteilen geklärt. Darauf aufbauend werden Einsatzmöglichkeiten der FE-Simulation zur Vorhersage der Veränderung der Oberflächeneigenschaften bei der Umformung beschichteter Bleche untersucht. Die FE-Modellierung ermöglicht schließlich eine halbzeuggerechte Auslegung und Optimierung des Umformprozesses.

Die Untersuchungsergebnisse zeigen, dass die Umformung organisch beschichteter Bleche grundsätzlich einen Abfall des Glanzgrades der Beschichtung bewirkt, wobei der Glanzverlust sowohl von der Höhe des Umformgrades als auch von den auftretenden Formänderungszuständen abhängt. Um das Versagen der Beschichtung sicher prognostizieren zu können, wird ein Grenzformänderungsdiagramm für die Beschichtung aufgenommen, um das Formänderungsvermögen des organisch beschichteten Blechs bei der Auslegung des Umformprozesses zu berücksichtigen. Ferner wird auch die Abhängigkeit der optischen Eigenschaften, wie die Glanzabnahme, von den Formänderungszuständen berücksichtigt. Die gewonnenen Erkenntnisse werden schließlich anhand des hydromechanischen Tiefziehens für eine praxisrelevante Bauteilgeometrie überprüft. Hierzu wird zunächst eine analytische Beschreibung des Einflusses von Geometrie- und Prozessparametern auf die Formänderungszustände durchgeführt. Auf Basis dieser Erkenntnisse wird die Prozessführung des hydromechanischen Tiefziehens hinsichtlich der Erzielung günstiger Oberflächeneigenschaften der Beschichtung der Blechformteile optimiert.

Abstract

The application of organically coated sheet metal (OCSM) possesses many advantages in comparison to the conventional sheet metal such as reducing the number of necessary manufacturing steps, reducing the production costs and a more environmental friendly production process. During forming processes, original properties of thin and relatively soft coating layers may be altered depending on forming conditions such as die radii and friction coefficient between blank and die components. Additionally, the forming processes induce large strains in materials that lead to topographical surface changes of steel substrate. As a result, the coating layer may be easily damaged and this is one of the major reasons which unexpectedly lead to the loss of protective and optical properties of the OCSM products. Therefore, it is essential to know the formability of OCSM in order to maintain all original functions i.e. optical and corrosion properties of the coating layer after forming processes. That means the undesirable defects such as cracking or delamination must be avoided by choosing an appropriate forming technique and by determining optimal process parameters. Furthermore, if these coating failures can be predicted, the process parameters of the processing may be adjusted in advance in order to prevent those damages. Therefore, a methodology for prediction of the change of functional coating layer properties as a function of plastic deformation is necessary.

In this research work, the process design for forming of organic coated sheet metal has been investigated. The project aims firstly at the investigation of the forming behavior of the OCSM, focusing on changes of the optical properties i.e. gloss degree depending on process parameters. Consequently, the application of Finite Element Method (FEM) to simulate the forming process of the OCSM and to predict the change of the surface properties is discussed. The FE modeling allows, finally, a material-based process design and optimization of forming process.

The experimental results indicate that the gloss reduction of the coated surface is basically caused by the strain states and strain level imposed on both steel substrate and the coating layer. In order to predict exactly the coating failures the forming limit diagram of coating (FLDC) should be used instead of the forming limit diagram (FLD) of steel substrate. By using FLDC, the formability concerning the optical property of the coating layer is considered in the process design of OCSM. Furthermore, the dependence of the gloss reduction on the strain states can also be taken into account.

The obtained results are finally validated by hydro-mechanical deep drawing (HDD) for forming of complex practice-oriented geometry. The influences of process parameters on the surface property of OCSM products in HDD process are also investigated. For this purpose, an analytical model is first investigated in order to evaluate the influences of geometrical and process parameters on the strain states and strain distributions over the forming part. Based on the conclusions obtained by the analytical results, the process design for the HDD process using OCSM can be optimized with regard to the best surface characteristics of organically coated layers.

Contents

Contents.....	i
Notations and Symbols	iii
Abbreviations	v
1 Introduction.....	1
2 State of the art.....	3
2.1 Basic characteristics and application domains of OCSM.....	3
2.1.1 Basic characteristics	3
2.1.2 Application domains.....	6
2.2 Forming of organic coated sheet metals.....	8
2.2.1 General requirements	8
2.2.2 Coating performance and formability of OCSM.....	10
2.2.3 Hydroforming technique and OCSM.....	20
2.3 Conclusion	26
3 Research aims and objectives	28
4 Influence of strain states and strain level on surface properties of OCSM	30
4.1 Materials used	30
4.2 Forming limit diagram (FLD) and forming limit diagram of coating (FLDC)	30
4.3 Gloss reduction depending on plastic deformation	34
4.3.1 Principle of gloss measurement	34
4.3.2 Relationship of gloss reduction to strain magnitude and strain states.....	35
4.4 Deformation induced changes in substrate and coating.....	40
4.5 Correlation between gloss reduction, plastic strain and roughness.....	45
4.6 Evaluation of the obtained results by means of practice-oriented test	46
4.7 Gloss recovery effect.....	50
4.8 Conclusion	53
5 Simulation of the forming process with OCSM.....	54
5.1 Modeling.....	54
5.1.1 FE model.....	54
5.1.2 Elements used and meshing.....	56
5.2 Material modeling for the coating layer.....	59
5.2.1 Energy function.....	59
5.2.2 Categories of hyperelastic model.....	60
5.2.3 Material data for organic coated material.....	63
5.3 Material model for steel substrate.....	64
5.4 Simulation set-up and results.....	65
5.4.1 Simulation set-ups	66
5.4.2 Simulation results and validations	68
5.4.3 Benefit assessment of modeling with coating layer	76
5.5 Prediction of surface quality based on FEM and experiment	79
5.5.1 Gloss reduction.....	79

5.5.2	Cracking of the coating layer.....	83
5.6	Conclusion	85
6	Material-specific process design of hydro-mechanical deep drawing for organically coated sheet metal	87
6.1	Manufacturing of parabolic reflector part by means of HDD technique.....	87
6.2	Experimental set-up for HDD process	88
6.3	Analytical model for HDD process.....	90
6.3.1	Strain and stress analysis in the flange region (Region I).....	92
6.3.2	Strain and stress analysis in the unsupported region (Region II).....	94
6.3.3	Analysis of strain and stress in the punch head (Region III)	97
6.3.4	Algorithm and analytical result.....	99
6.4	Investigation of HDD process by FEA and experiments.....	105
6.4.1	Simulation set-up.....	105
6.4.2	FE results and validations	107
6.4.3	Influence of counter pressure on the strain distribution.....	110
6.4.4	Influence of BHF on the strain distribution.....	112
6.5	Experimental validations	114
6.5.1	Validation of the influence of the counter pressure profile	114
6.5.2	Validation of the influence of the BHF.....	115
6.5.3	Gloss reduction.....	117
6.6	Conclusion	119
7	Conclusions and future developments	121
	References	123

Notations and Symbols

Symbol	Unit	Description
A	mm ²	Current cross-section area
A_0	mm ²	Initial cross-section area
A_g	MPa	Fracture elongation
b	mm	Current width of specimen
b_0	mm	Initial width of specimen
C_{ij}		Material constant of the hyperelastic material
D_p	mm	Punch diameter
D_D	mm	Die diameter
E	MPa	Young's modulus
F	N	Force
G	MPa	Shear modulus
G_0	GU	Initial gloss value
G_i	GU	Updated gloss value
k_f	MPa	Flow stress
l	mm	Current length of specimen
l_0	mm	Initial length of specimen
n		Hardening exponent
p	MPa	Pressure
r_p	mm	Radius of punch edge
$r_{p,1}$	mm	Punch radius
r_D	mm	Die radius
R_p	MPa	Yield strength
$R_{p0.2}$	MPa	Tensile yield strength
t	mm	Current thickness
t_0	mm	Initial thickness
$t_{Sub.}$	mm	Thickness of steel substrate
$t_{coat.}$	mm	Thickness of coating layer
W	J	Energy function
W_p	mm	Width of punch
W_D	mm	Width of die
μ		Friction coefficient
σ_r	MPa	Radial stress

σ_θ	MPa	Tangential stress
σ_e	MPa	Equivalent stress
σ_0	MPa	Initial flow stress
φ_1		Major strain
φ_2		Minor strain
$\bar{\varphi}$		Effective strain
φ_r		Radial strain
φ_θ		Hoop strain
φ_l		Strain in longitudinal direction
φ_b		Strain in wide direction
φ_s		Strain in thick direction
$Sgn(x)$		+ or – sign of scalar x
μ, λ	MPa	Lamé coefficients
ρ	g/mm ³	Mass density
ν		Poisson ratio
γ_{ij}		Shear strain
$\lambda_1, \lambda_2, \lambda_3$		Principal stretches
$d\mathbf{X}$	mm	Position vector in un-deformed configuration
$d\mathbf{x}$	mm	Position vector in deformed configuration
\mathbf{F}		Deformation gradient
\mathbf{E}		Green-Lagrange strain vector
\mathbf{C}		Right Cauchy-Green strain tensor
I_1, I_2, I_3		First, second and third invariants of the right Cauchy-Green strain tensor
\mathbf{S}	MPa	Second Piola-Kirchhoff stress tensor
\mathcal{C}	MPa	Constitutive tensor

Abbreviations

Abbreviation	Meaning
BHF	Blank holder force
BH	Blank holder
BT	Bottom of the cup
EP	Epoxide
GRD	Gloss reduction diagram
HDD	Hydro-mechanical deep drawing
HDP	High durable polymer
FLD	Forming limit diagram
FLDC	Forming limit diagram of coating
FE	Finite element
FEM	Finite element method
G	Gloss value
GR	Gloss reduction
LG	Loss of gloss
OCSM	Organic coated sheet metal
PR	Punch radius
2D	Two-dimensional
3D	Three-dimensional
PUR	Polyurethane
PUR-PA	Polyamide modified polyurethane
PVC (F)	Polyviyl chloride
PVC (P)	Polyvinyl chloride plastisol
PVDF	Polyvinylidene fluoride
PVF (F)	Polyvinyl fluoride
PES/PS	Polyester
SW	Sidewall

1 Introduction

Nowadays, the amount of products which are made of organic coated sheet metal (OCSM) is increased. In comparison to conventional sheet metal materials, the use of the OCSM possesses many advantages such as reducing the number of necessary manufacturing steps, reducing the production costs and a more environmental friendly production process. Considering the design of the OCSM, the thickness of the organic coating layers are quite thin compared to the steel substrate, and they often range from 1:2.5 to 1:50, *Thyssen (2003)*. Additionally, the organic material and steel substrate have substantially different properties, especially when these materials are in large deformation states. The thin and relatively soft coating layer is extremely “sensitive” to the forming conditions such as tool radii, friction between blank and die components. Moreover, the imposed plastic deformations on the steel substrate also have a significant influence on the coating performances. The results of plastic strains in the steel substrate lead to topographical surface changes of the steel substrate. As a result, the coating layer may be easily damaged and this is the one of the main reasons, which unexpectedly leads to failures of the products, *Wang & Vayeda (2007)*, *Van den Bosch et al. (2007)*. The typical coating failures such as delamination, cracking or roughening are depicted in Fig. 1- 1.

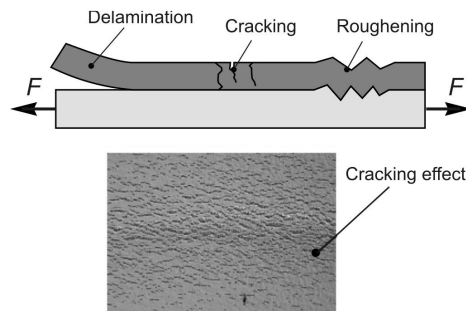


Fig. 1- 1: Typical failures of coating layers, *Schikorra et al. (2002)*, *Van den Bosch et al. (2007)*

The coating failures lead to a loss of protective and to a worsening of optical properties of the OCSM. Therefore, a crucial requirement for the forming of OCSM is to maintain all the original functionalities i.e. optical and corrosion properties of the coating layer. That means the undesirable defects such as cracking or delamination must be avoided by choosing an appropriate forming technique and by determining optimal process parameters. Furthermore, if these coating failures can be adequately predicted, the processing parameters and conditions of the manufacturing process may be adjusted in advance in order to prevent those damages.

Therefore, the aim of this research work is to evaluate the surface quality of OCSM depending on different deformation states and to optimize the forming process of OCSM on the basis of this knowledge and numerical methods.

The research work was categorized into different areas and it was structured in the following dissertation chapters. An intensive literature review was carried out in the second chapter

before starting the research work. The state of the art clearly indicates remaining problems requiring further research. The identified challenges together with the research vision confirmed the research work areas. Based on these identifications, the aims and objectives of the studies were specified in the third chapter. In order to achieve the research goals, fundamental investigations of the forming behavior of the OCSM are presented in the fourth chapter. The fifth chapter deals with the simulation strategy for the computation of the industrial forming process of the OCSM. In this chapter, the prediction of changing optical properties based on the experimental and numerical results are also presented. In chapter six, the influences of processing parameters of the Hydro-mechanical Deep Drawing (HDD) process such as the counter pressure, the Blank Holder Force (BHF) on the surface quality i.e. gloss reduction of OCSM products are investigated numerically and experimentally. In the last chapter, the main results of this study are summarized. Based on these research outcomes, the process scope is reported. Finally, in the seventh chapter, overall conclusions are drawn and recommended for further research works.

2 State of the art

2.1 Basic characteristics and application domains of OCSM

2.1.1 Basic characteristics

The organic coated sheet metal (OCSM) is generally composed of a steel substrate (cold rolled or with a zinc-based metallic coating) with a surface treatment layer, a paint prime coating and a topcoat, *Arcelor (2004)*, for more details see Fig. 2- 1.

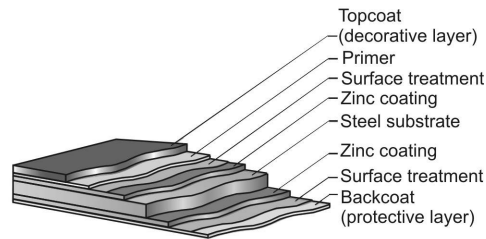


Fig. 2- 1: Structure of OCSM, *Arcelor (2004)*

The use of the primer layer results in enhancement of the adherence of the top coat, improvement of flexibility and corrosion resistance of the coating layer. The topcoat acts as decorative layer. The use of the topcoat is to provide the desired surface characteristics such as color, gloss, etc. The back coat is considered as protective layer. Depending on the required performance a single (primer) or double (primer + topcoat) coating layer can be applied on one or both sides of the sheet, *Arcelor (2004)*. Generally, a continuous coil coating line consists of three main sections i.e. the entry section, the central section and the exit section. In Fig. 2- 2 the typical system schematic of the coil coating line according to *colofer (2008)* is illustrated. In the entry section, the coil or individual strip steel is placed on a pay-off reel (8) and welded by using a laser welding machine (9) in order to ensure the continuous process. A band accumulator system (4) is utilized to maintain a constant speed. The strip cleaning and pre-treatment system (10) is employed afterward in order to prepare the strip or coil surface before coating.

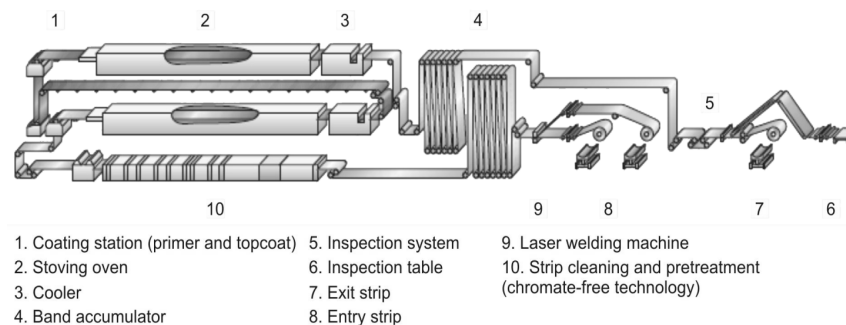


Fig. 2- 2: Schematic illustration of the coil coating line, *colofer (2008)*

The first coating process is carried out in station (1). In this station, the primer, the back coat and the topcoat are applied on the topside and the reverse side of the strip. The coated material used is normal baking enamel. Thus, a stoving oven system (3) is utilized in order to network the coating layer at about 220 – 250°C, *colofer (2008)*. Afterward, the coated coil is cooled using a cooler system (3). The coated coil is then passed through an inspection zone (5), (6) and finally reaches the coiler (7).

For the OCSM, the steel substrate has a direct influence on the processing performance and corrosion resistance of the product. It is suggested that a relatively thick zinc-based metallic coating should be chosen for good corrosion resistance. On the other hand, thin and flexible crack resistant zinc coatings are utilized to sustain original functionalities during the forming process i.e. without cracking or any other failures. The surface treatment is carried out at the beginning of the process prior to coating in order to ensure bonding between layers, *Arcelor (2004)*. The thickness of the surface treatment layer is generally smaller than 1 µm. The type of steel substrate used depends on the requirements with respect to durability and forming demands. An overview of the common steel substrates is tabulated in Table 2- 1.

Table 2- 1: Overview of the most common substrates used in coil coating, *Thyssen (2003)*

Steel grades	Name	Thickness in mm
Cold rolled sheet - Mild unalloyed steels to En 10130 - Structural steels to DIN 1623 part 2	DC01 - DC06	0.4 – 3.0
Electro-galvanized sheet - Mild unalloyed steels to En 10152 - Structural steels to DIN 1623 part 2	DC01 – DC06 + ZE	0.4 – 3.0
Hot dip galvanized sheet - Mild unalloyed steels to En 10327 - Structural steels to EN 10326	DX51D+Z – DX57D+Z	0.4 – 3.0
Hot dip zinc aluminium (ZA) coated sheet (GALFAN®) - Mild unalloyed steel to EN 10327 - Structural steels to EN 10326	DX51D+ZA – DX57D+ZA	0.4 – 3.0
Hot dip aluminium zinc (AZ) coated sheet (GALVALUME®) - Mild unalloyed steel to EN 10327 - Structural steels to EN 10326	DX51D+AZ – DX54D+AZ	0.4 – 2.0
Hot dip aluminized sheet - Mild unalloyed steels to EN 10327 - Structural steels to EN 10326		

The classification of the OCSM depends on the number of the coating layers on the top side. Accordingly, the OCSM product is classified into single-coat, two-coats or multiple-coat system. The top side of the strip is subjected to continuous check during manufacture or in further processing such as forming or rolling. This side has normally to meet the highest demand in terms of appearance and corrosion resistance. The reverse side is usually given a backing coat or protective layer. The back coat is normally a zinc coating with a single layer protective coated, *colofer (2008)*. The possible coating system is schematically illustrated in Table 2-2.

Table 2- 2: Possible coating system, *colofer (2008)*

Nr.	Type of coating system	Construction
1	Single coat	<p>Top side</p> <ul style="list-style-type: none"> Single coat Surface treatment (< 1µm) Zinc coating <p>Reverse side</p> <ul style="list-style-type: none"> Zinc coating protective film
2	Two coat system	<p>Top side</p> <ul style="list-style-type: none"> optional: protective film Top coat Primer Surface treatment (< 1µm) Zinc coating <p>Reverse side</p> <ul style="list-style-type: none"> Zinc coating protective film
3	Multiple coat system	<p>Top side</p> <ul style="list-style-type: none"> Top coat 2 Top coat 1 Interlayer Primer Surface treatment (< 1µm) Zinc coating <p>Reverse side</p> <ul style="list-style-type: none"> Zinc coating protective film

For the single coat system, only one topcoat on the topside is used as decorative layer. There is normally no primer in this case. The two-coat system consists of an additional primer and optionally protective film beside zinc coating and surface treatment. The multi-coat system includes primer, interlayer and one or two topcoats on the top side. Similar to the case of the two-coat system, the multi-coat system is suitable for further forming processing. Both systems satisfy the formability, performance and also corrosion requirements.

For the OCSM, the choice of coating system depends on decorative and functional requirements. Functional properties take into account formability, corrosion behavior and thermal resistance. Decorative properties consist of color, gloss degree and surface structure,

Arcelor (2004). In addition, the selection of the coating system also depends on the intended purpose i.e. indoor or outdoor application. In Table 2- 3 the most common coating materials used and the main properties are shown.

Table 2- 3: Properties of coil coated sheet, Thyssen (2003)

Properties	Coating material								
	EP	PES	PUR	PUR_PA	HDP	PVDF	PVC(P)	PVC(F)	PVF(F)
Common coating thickness μm	10	25	25	25	25	25	100 - 200	100 - 200	38
Surface hardness	A	B	C	A	B	C	E	D	D
Heat resistance to max. $^{\circ}\text{C}$	80	80	80	80	80	110	60	60	110
Formability/bending	E	C	B	C	B	A	A	A	A
Formability/roll forming	D	B	B	B	B	A	A	A	A
Formability/deep drawn.	F	C	A	B	B	A	B	B	B
Abrasion resistance	D	D	E	B	D	C	A	A	B

Remarks:

- A = excellent, B = very good, C = good, D = satisfactory, E = adequate, F = not usable or not suitable
- Heat resistance = not constant exposure

2.1.2 Application domains

The main idea behind the use of OCSM in all sectors of industry from beverage can manufacturing to the automotive field is “Finish first, fabricate later”.

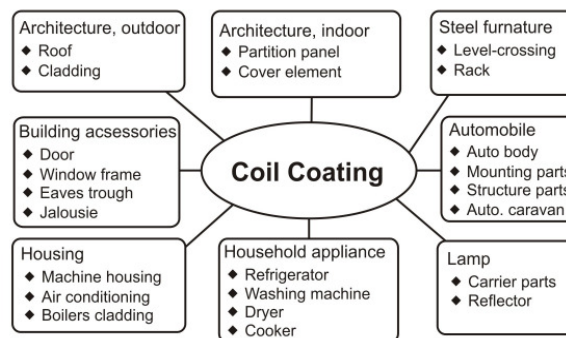


Fig. 2- 3: Application fields of OCSM, Meuthen & Jandel (2005)

The application domains of OCSM are depicted in Fig. 2- 3. In civil engineering, for example, these products are used for wall cladding, roofing and also for applications such as suspended

ceiling, lighting, etc. In the domestic appliance market, the advantages of organic coated steel are used for white goods such as refrigerators, washing machines and also for small kitchen appliances like microwave oven and anti-sticky pan, etc., *Thyssen (2003)* see Fig. 2- 4. In automotive industry, the organically coated sheets are used for the production of body parts, inner parts, etc. *Arcelor (2004)*.

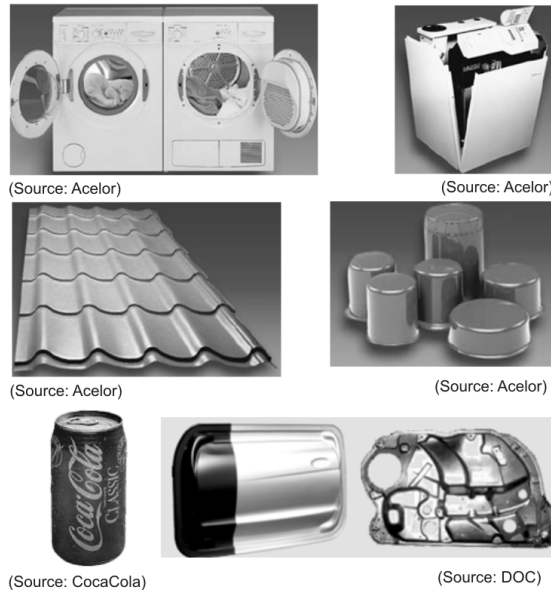


Fig. 2- 4: Organically coated products

By utilizing this kind of material, the numbers of necessary manufacturing steps as well as production costs have been significantly reduced and the product quality has been significantly improved. In comparison to the traditional sheet metal materials, this material possesses many advantages in terms of economical, ecological and technological aspects. From the economical point of view, coil coating lines provide high productivity and reduce the cost of applying an additional coating system. For the users, there is no need to invest in an additional system such as decreasing installations or other surface treatment equipment in their paint-shop, *Meuthen & Jandel (2005)*. From the ecological point of view, the working conditions are significantly improved by eliminating the use of solvents and the handling as well as storage of chemical products, *Thyssen (2003)*.

From the technical point of view, the main advantage of organic coated steel is consistent quality. The flexibility of the coil coating process allows producing a range of different surfaces such as smooth, orange peel, grained, textured or embossed, which can be obtained in a wide range of color and the required degree of gloss, from matt to high gloss, *colofer (2008)*. The advantage of using OCSM compared to traditional sheet metal in the automobile industry is shown in Fig. 2-5.

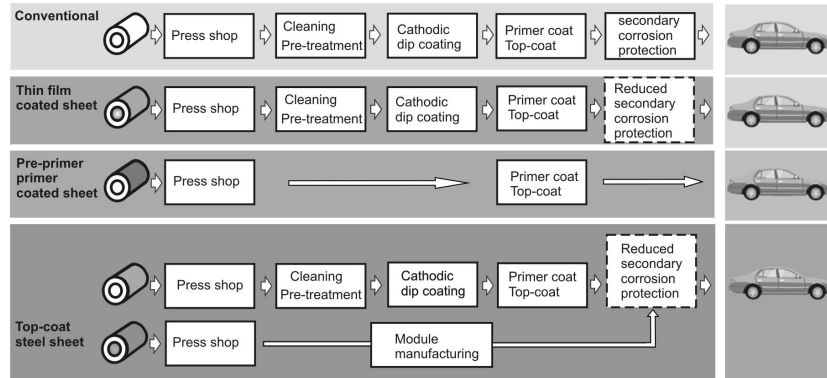


Fig. 2-5: Advantage of organic coated steel compared to traditional steel sheet, *Wolfhard (2003)*

2.2 Forming of organic coated sheet metals

2.2.1 General requirements

The most important requirement on OCSM and their processing technologies is maintaining all the original properties i.e. corrosion resistance and optical appearance of the coating layer during processing, without any failures. That means, excessive deformation and the occurrence of surface damage must be avoided. These requirements can be achieved by observing a few basic rules, *Arcelor (2004)*:

- Use of dedicated processing lines and storage facilities
- Using an appropriate working temperature.

In Fig. 2-6 the effect of working temperature on the physical properties of the coating layer is shown.

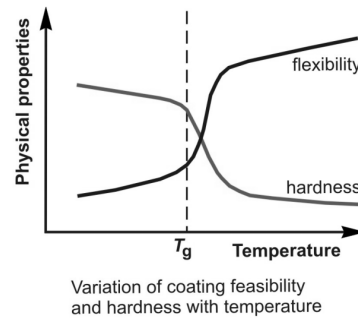


Fig. 2-6: Working temperature of OCSM, *Arcelor (2004)*

It is suggested that the OCSM must be deformed at a temperature above the glass transformation point T_g , *Arcelor (2004)*. This is the reversible transition of amorphous materials from a hard state into a molten or rubber-like state, *Schulze (1994)*. The ideal temperature is suggested to be about 20°C . If it is colder in the warehouse, the OCSM should be transferred to a warmer location with a temperature of around 20°C , 24 hours before

processing. This procedure ensures that the coating has excellent formability, *Arcelor (2004)*. Furthermore, the OCSM need to be handled carefully. Equipment for handling coils should have a protective layer. These tools must be used with great care to avoid any hard impact which could leave a mark on the contact surface of the product, *Thyssen (2003)*.

During the forming process, the sensitive coating layer is in direct contact with the forming tools i.e. punch, die and blank holder. For this reason, it is recommended to use extremely clean forming tools. In order to avoid scratches or tearing of a coating layer, the contact area of the forming tools should be polished. This procedure can consequently reduce the friction coefficient. The OCSM have a very low friction coefficient with steel tools, often less than 0.05, *Meuthen & Jandel (2005)*. In some cases, a temporary protective film may be added to protect the coating layer.

In the deep-drawing process, the steel substrate and the coating layer are subjected to different deformation modes, *Marciniak & Duncan (1991)*. The different deformation modes i.e. compression, stretching, plane strain, uniaxial tension and shearing each have specific effects. The compressive mode must be controlled since it causes an increase in thickness which can cancel out the permitted tooling clearances. It is recommended that the die entry radius should be increased as far as possible. The clearances between the punch and the die must be equal to the total thickness of the OCSM plus 5 to 10%, *Arcelor (2004)*.

In the roll forming process, similar requirements are considered. It is suggested that the diameter of rolls should be as large as possible. Additionally, all sharp angles on the roll must be replaced by fillets. The roughness and hardness of the rolls require particular attention. The best materials for the roll are low or high alloy steels quenched ground. The application of a layer of chrome is the ideal solution in this case. A temporary protective film is an additional solution for roll forming to ensure the original properties of organic coatings, *Meuthen & Jandel (2005)*.

For the bending process, the control process is similar to the one of the roll forming process. For V-bending, for instance, it should be noted that the die opening used is normally 6 to 12 times of the total thickness of the coated sheet. The higher value of this parameter is preferable for the bending of OCSM. Force or impact bending in a V-die is not suitable for organic coated steel, *Thyssen (2003)*. It is recommended that folding is the best suitable method.

In the spinning process, the roller must have a large diameter and a perfectly polished surface in order to avoid damage of the coating layer. The surface of the mandrel must also be well polished to ensure easy sliding of the OCSM. In some cases, the feed rates must be reduced to prevent overheating that may lead to coating failures, *colofer (2008)*.

For joining of the OCSM, one solution is adhesion bonding. However, it is recommended that clinching is an extremely suitable method. This technique allows to join very different materials without using additional materials. In order to guarantee the attractive appearance of the clinching points, local lubrication with volatile oil should be used, *Mende (2006)*. Consequently, this will reduce friction between the punch, the surface of the OCSM and the die.

2.2.2 Coating performance and formability of OCSM

2.2.2.1 Coating performance

Coating performance and formability are the critical criteria when forming organically coated sheet metal. The forming of OCSM can be considered as a forming process of a complex metal–polymer composite material on account of the different mechanical properties of the steel substrate and the coated material, *Strauß (2008)*. Typically, the steel sheet metal has a much higher elasticity modulus and a lower yield strain than the polymer. In addition to that, the mechanisms for plastic deformation in both materials are also entirely different.

The material behavior of the steel substrate can be successfully described by means of established methods like tensile test, hydraulic bulge test etc. Among these, the tensile test can be used to provide the flow curve. The well known *Nakajima test* contributes the forming limit diagram (FLD) that is useful to predict the formability of the steel substrate, *Marciniak & Duncan (1991)*. In contrast to the metal substrate, the coating material shows viscoelastic properties. The inherent network structure of the coated material itself determines the material properties. The low network density coating material results in relatively low mechanical strength but very good flexibility and high formability. The higher network density provides a good chemical and corrosion resistance and a higher mechanical strength, Fig. 2- 7.

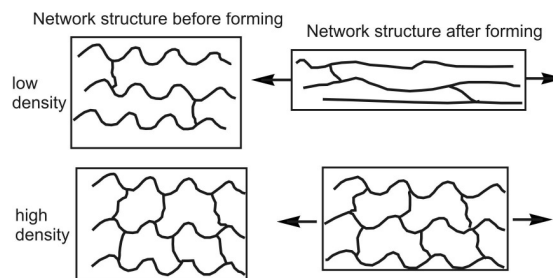


Fig. 2- 7: Network structure of organically coated material, *Strauß (2008)*

During plastic deformation this mismatch in mechanical properties may lead to compatibility problems for the microscopic deformation at the interface, *Van Tijum (2006)*. The plastic deformation involves, thus, a complicated structure evolution in both metal substrate and coating layer. Basically, the imposed plastic strain on the metal substrate induces dislocation movement on favorably oriented slip-systems within grains, *Kopp (1999)*. This can result in topography changes i.e. roughening at the interface area as the dislocation escapes the grains, *Van Tijum (2006)*. The resulting roughness may lead to a loss of adhesion and consequently, coating failures in further processing.

As a result of the existence of adherence between the coating layer and the steel substrate, it can be concluded that the roughening at the interface determines the deformation of the polymer near the interface, *Ward (1983)* and *Van Tijum (2006)*. The coating layer has to adapt to the imposed displacement by the metal at the interface as shown in Fig. 2- 8, *Van Tijum (2006)*.

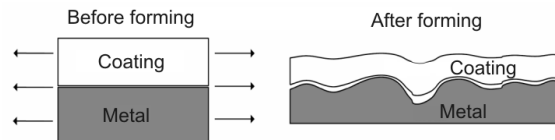


Fig. 2- 8: Deformation behavior of polymer and steel substrate, Van Tijm (2006)

Additionally, the steel substrate is subjected to complex axial and shear deformation during the forming processes. The occurring strain distributions cause the externally applied stresses on the coating layer. The differences in mechanical behavior of both steel substrate and coating layer when these materials are in large deformation, on the one hand and the non-uniformity imposed strains, on the other hand, are also the cause of additional residual stresses in the coating, *Polyakova et al. (2000)*. Among these, the compressive stresses may cause the coating layer to buckle up off the steel substrate while the tensile stresses may force the coating layer to peel off as indicated in Fig. 2-9. These processes occur when the elastic strain energy exceeds the required energy to remove the coating layer from the substrate. The strain energy increases with increasing coating thickness. Therefore, these failure modes are more often encountered in thick coating layers with high residual stress, *Hohlfelder (1999)*.

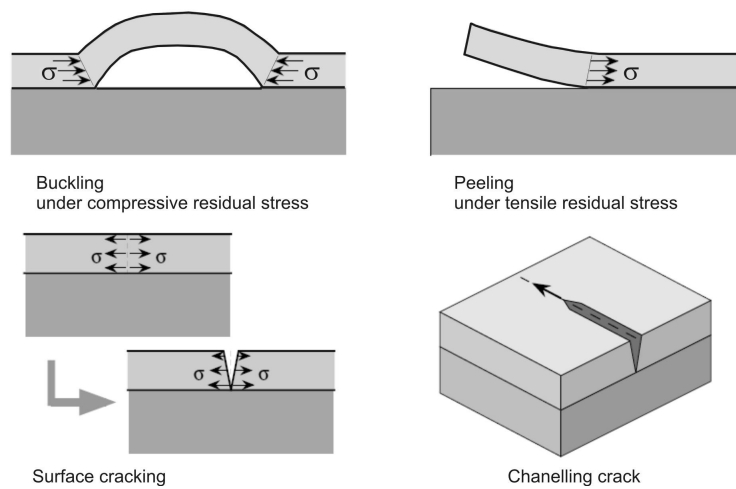


Fig. 2- 9: Possible coating failures according to Hohlfelder (1999)

Under tensile stress, the coating layer may experience cracking in the surface. Then, it propagates through the coating thickness. The driving force for surface crack propagation is relaxation of elastic strain energy. If the stress is sufficiently high, these cracks may propagate laterally through the coating thickness in a channelling process as shown in Fig. 2- 9, *Hohlfelder (1999)*.

Basically, the coating failures can be divided into three types. The first one relates to the optical properties such as inadmissible gloss reduction or several color deviations that are affected by the change of the molecular structure of the coating material itself and surface roughness of the steel substrate. The second one such as delamination and buckling are the results of a defect of coherence at the interface. The third one, i.e. cracking and roughness, concerns the fracture toughness and relates to the mechanical strength of the coated material. The coating failures lead to a loss of protective and attractive properties. If the coating failures can be predicted, the process parameters and conditions of the manufacturing process can be adjusted in advance to prevent the unexpected failures, *Schreurs et al. (2009)*. Therefore, the fundamental understanding of the relations between the deformation behaviors and coating appearance of the OCSM products is crucial.

With regard to the coating performance after the forming process, *Lawrenz (1978)* investigated the deep-drawing behavior of organic coated sheet metals and tested the surface quality of the products. By using analytical method and experimentations, the influences of the main technological parameters such as forming rate, tool geometries on the deep drawing and hydro-mechanical forming process were investigated. The relation between quality such as gloss reduction and roughness depending on the effective strain in case of the tensile test and the deep drawing process were experimentally evaluated. These investigations have shown first results regarding the influence of the coating layer on the friction coefficient, and the increase of gloss reduction with higher effective strains on flat part surfaces were investigated.

The relation between the coating failures and the imposed plastic deformations on the steel substrate is the key challenge when forming OCSM. In another contribution, *Polyakova et al. (2000)* investigated two failure modes that occur on deep drawing cups. Mode I related to the coating delamination at the top of the cup due to the buckling instability. Mode II concerned loss of adhesion along the cup wall due to elastic retraction of the unconstrained cup at the end of the deep drawing process. The deformations of the steel substrate were characterized by the macroscopic appearance and strain distributions and were correlated with the mode of coating failures afterwards. The failure mode I dominated in the buckled valley regions of the cup, while the failure mode II occurred at the very end of the forming process, when the entire cup lost the constraint of the blank holder and slipped into the gap between die ring and punch. Clearly, the buckling instability is deeply related to the earing phenomenon of the deep drawing cup. It is obvious that the coating failures occur at the uncritical area of the cup.

The mechanism of defect growth of polymer coated packing is studied by *Boelen et al. (2004)*, and *Bjerke'n et al. (2006)*. In these investigations, the main factors that influence the initiation and propagation of defects are experimentally determined. It was shown that a number of effects are responsible for either the initiation of a defect and the propagation of the initial small defect into large blisters. Important aspects here are the chromium metal and chromium oxide levels, the presence of oxygen and the deformation process. Furthermore, crystallization effects during sterilization and the related oversaturation of the coating with water are important factors. In another research, *Boelen et al. (2004a)* explained the changes in the coating of polymer coated steel during sterilization by using electrochemical

measurements. According to this, the polymer coating layer is locally thinned during deep drawing due to roughening of both surfaces (the substrate and the coating surface), that leads to a reduction of the coating thickness. The thickness reduction is due to the fact that the coating is stretched during deformation and therefore oriented in one direction.

Aiming at the analysis of forming and friction characteristics of pre-coated sheet metal on die materials, rectangular deep drawing processes were experimentally conducted by *Kim et al. (2002)*. According to *Kim*, the coating's defects, i.e. scratching, cracking, should be used as forming limit of the pre-coated sheet metal. During the forming process, the coating layer acted as lubricant under non-lubricated conditions. The correspondent friction coefficient in this case was relatively low. Furthermore, it was found that the surface roughness of the coating layer strongly depends on its thickness. The thin coating layer results in the better surface roughness.

The physical relationships between the molecular structures of the polymer coating, the deformation behavior and appearance of the coil coated sheets were presented by *Buder-Stroisznigg et al. (2004)*. The tensile test using single- and two-coat systems was conducted. The coated surface before and after forming was analyzed by means of a confocal microscope. It was found that the increase of the deformation level causes the topographical change of the coating performance. The waviness of the surface increased with increasing deformation level.

The basic prerequisite for the organic coated or pre-painted sheet metal to be deployed in the automobile industry is crack-freeness and, furthermore, remaining excellent adhesion. The term adhesion is a property of material interfaces, i.e. refers to an interface capacity to resist mechanical separation. In the context of the coating layer, it describes a film's ability to remain attached to the surface on which it is deposited. The quality of adhesion is related to the strength of chemical bonding across the interface. The adhesion is strongly affected by interfacial cleanliness and surface roughness, *Van Tijum (2006)*.

The characterization of the adhesion is a complex problem, *Hohlfelder (1999)*. A useful objective for an adhesion characterization is to measure the amount of required energy per unit area to debond a coating layer from its substrate. The employed techniques to measure the adhesion are tape test, peel test, pull-off test, scratch test, blister test and beam bending test as shown in *Hohlfelder (1999) and Hult et al. (1999)*.

For the forming of OCSM, the adhesion of the coating to the sheet metal is the key factor that influences directly the coating failures such as the delamination phenomenon. If the adhesion force is not sufficiently high, delamination may occur and that leads to a loss of protective and optical properties, *Schreurs et al. (2005)* and *Schreurs et al. (2009)*. The delamination modes of the coated sheet metal can be either uniform, mixed-mode uniform, non-uniform or mixed-mode non-uniform as shown in Fig. 2- 10.

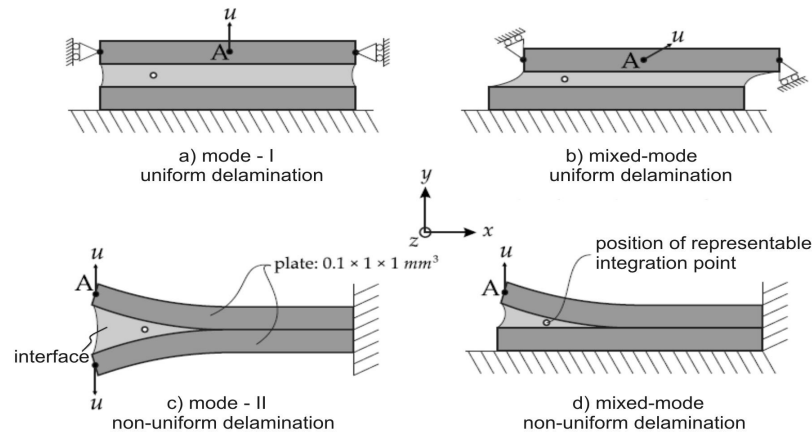


Fig. 2- 10: Delamination modes of OCSM, *Schreurs et al. (2009)*

In order to take into account the delamination effect, the interface area between the coating layer and the steel substrate must be investigated. By using experimentation, it can be observed how the delamination occurs. It is found that fibrillation is the main mechanism that leads to the delamination of the coating layer from the steel substrate under the imposed loading conditions as shown in Fig. 2- 11, *Schreurs et al. (2009)*.

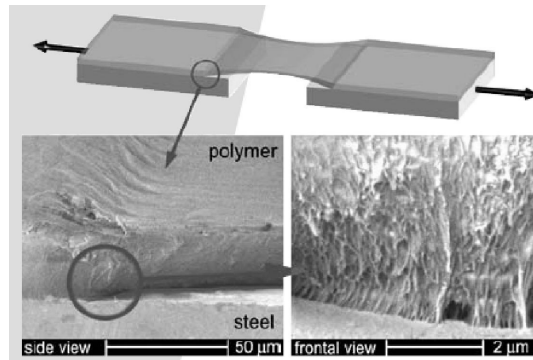


Fig. 2- 11: Experimental observation of fibrillation, *Schreurs et al. (2009)*

For this reason, a numerical tool that can successfully describe the interface area is required. With regard to the interface area between the steel substrate and organic coating, a large variety of cohesive zones have been proposed in recent year, *Williams & Hadavinia (2002)*; *Van den Bosch et al. (2007)*. Fundamentally, the cohesive zone describes the relation between the normal opening displacement, the normal traction and a separate relation for the coupling between the tangential opening displacement and the tangential traction, see *Van den Bosch et al. (2008)*, for an overview. In Fig. 2-12 a cohesive zone element is schematically presented.

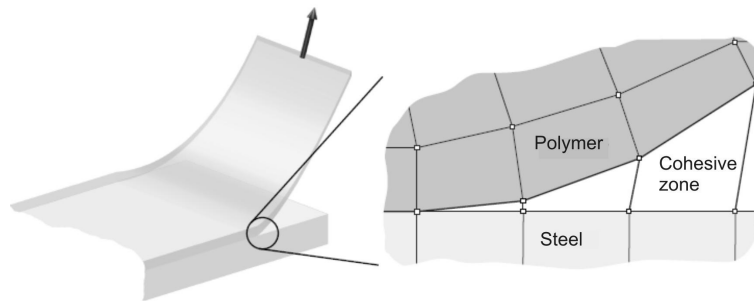
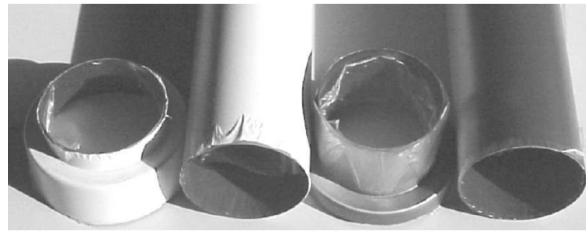
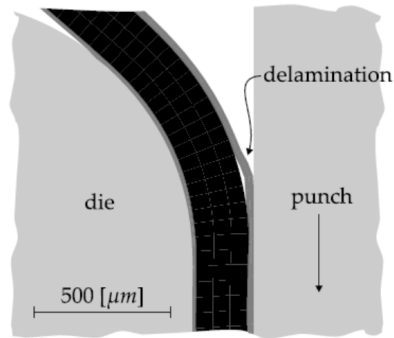


Fig. 2- 12: Cohesive zone element with initial zero thickness, *Van den Bosch et al. (2007)*

By developing a cohesive zone model with large displacement formulation accounting for interfacial fibrillation, the delamination phenomenon of the polymer coating is taken into account, *Van den Bosch et al. (2007)*.



Example of products that show delamination



Delamination predicted by FEM simulation

Fig. 2- 13: Experimentally determined and numerically predicted delamination, *Schreurs et al. (2009)*

For this purpose, a mixed numerical-experimental approach in order to quantitatively investigate and characterize delamination in polymer coated metal sheet was presented by *Van den Bosch et al. (2008)*. In this investigation, the integral bi-material system was analyzed. It was shown that the peel test is a suitable technique to study the debonding of the

polymer coating from its substrate. The coating thickness varies considerably across the polymer coated sheet. Furthermore, it is important to establish an accurate constitutive model of the coating layer on account of large inelastic deformation of the coating during the peel test.

Consequently, another contribution that develops a numerical model allowing to predict the delamination of the polymer coating from the steel substrate during deep drawing process was done by *Schreurs et al. (2009)*. The experimentally characterized cohesive zones were used to describe the interface between the polymer and the steel and were capable of modeling delamination of a prior partial loss of adhesion during an axis symmetric deep drawing simulation. According to this investigation, the delamination was observed on account of squeezing of the coating layer between the substrate and the punch as shown in Fig. 2- 13. The experiment has shown that the delamination occurred at the top of the cup while the numerically predicted one occurred at another position on account of an external condition i.e. squeezing. The developed tool has provided a quite good delamination prediction in this case. However, it is necessary to improve the accuracy of the predicted model that can take into account a combination of all key factors leading to the loss of adhesion.

Further key technical requirement of the forming of OCSM is that the coating layer should not be damaged during various operations in sheet metal forming such as cutting, bending, embossing, roll forming or deep drawing. In addition to delamination, the organic coating has to be free from defect such as cracking, chipping and scratch. Therefore, the durability of coating during plastic deformation has become a crucial concern. The strain states in sheet metal forming can be either biaxial ($\varphi > 0$, $\varphi_2 > 0$), plane strain ($\varphi > 0$, $\varphi_2 = 0$) or deep drawing ($\varphi > 0$, $\varphi_2 < 0$). These strain states can result in the change of the interface area between the coating and steel substrate in case of OCSM. According to *Wang & Vayeda (2007)* the coating adhesion can be affected by plastic deformation. However, there was no significant debonding when the material was subjected to biaxial stretching, whereas the adhesive bond deteriorated and coating pickup was observed in the tape test for the deep drawing deformation mode.

With respect to the coating durability, *Wang & Vayeda (2007)* developed a new technique to evaluate adhesion of coating to sheet metal under plastic deformation. The PVDF coated sheet metal with two types of primer i.e. PES and PUR primer was investigated. Based on the concept of the Forming Limit Diagram (FLD), the coating performance was evaluated by using the standard test according to ASTM D3359 such as the notch-coating adhesion test, the cross-hatch tape test, accelerated conditioning, the uniaxial tensile test and the rectangular stretch bend test. The effect of external conditioning such as time, humidity and corrosion environment on the coating performance was presented. The durability diagram has shown that the higher substrate strain caused the adhesive bond to deteriorate and further led the coating failure. The durability limit diagram was constructed and could be used in conjunction with the FLD to determine the feasibility of a complex forming operation.

In another research, *Hatanaka et al. (1989)* investigated the coating adhesion after deep drawing in relation to the pre-treatment of aluminum. It was concluded that the deterioration of adhesion by drawing was due to the cohesive failure of films resulting from pre-treatment

and the change in the underlying surface topography. The performance of polyurethane- and polyester-coated stainless steel after Erichsen cup drawing was evaluated by *Deflorian et al. (2000)*. The adhesion was evaluated by means of electrochemical impedance spectroscopy. Other contributions concerning the coating adhesion and coating durability were presented by other researchers. For example, *Gay (2000)* investigated the adhesion between a solid and a stretched elastic material. For this kind of material, it was found that the adhesion is not affected by stretching at a molecular scale. The adhesion, however, is changed on a macroscopic scale on account of the elastic response of the material. *Chang et al. (1997)* developed the notched coating adhesion test to evaluate the adhesive performance and durability. The accelerated humidity condition is considered in this test. The coated specimens were subjected to uniaxial tensile strain and the strain at which the delamination occurred was used to calculate the critical strain energy release rate. This test can successfully be used to evaluate the interfacial fracture toughness of the coating layer.

2.2.2.2 Formability of OCSM

In sheet metal forming, failures normally occur due to the development of localized necking in the material, *Marciniak & Duncan (1991)*. The strain states and strain values at which localized necking are first observed can be experimentally measured. By conducting the Nakajima tests and plotting the maximally allowable value of the principal strains, the FLD of the material can be established as shown in Fig. 2- 14, *Hasek & Lange (1980)*.

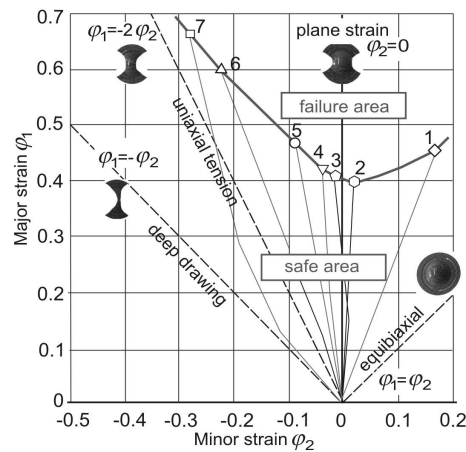


Fig. 2- 14: Forming limit diagram

The FLD is a strain-based analysis technique. This diagram offers the chance to determine process limitations in sheet metal forming and it is widely used to evaluate the formability of sheet materials. Concerning the FLD prediction of the sheet metal, numerous attempts have been contributed, *Hora (2006)*. For example, *Keeler (1965)* has presented the determination of forming limits in automotive stampings as a pioneer investigation. In another research, *Xu et al. (1998)* evaluated the effect of various material parameters on the positive minor strain

side of the FLD. It was found that the limit strains were strongly dependent on the yield locus shape. An advanced method to describe the forming of sheet metal was presented by *Klocke et al. (2003)*. By taking the whole stress and strain behavior during the forming process into account, ductile fracture could be predicted.

For organically coated sheet metal, the plastic deformation imposed on the steel substrate may result in an increase or decrease of surface area at the coating-primer-substrate interface, *Hohlfelder (1999)* and *Hult et al. (1999)*. The changing of interface effects may also lead to the change of coating performance i.e. coating failures, and it requires a thorough understanding. Thus, the formability of OCSM must consist of not only the formability of the steel substrate but also the coating failures such as cracking, scratching.

A pioneer investigation concerning the formability of OCSM was done by *Fischer & Klein (1971)*. By conducting cupping, cylindrical and square cup tests, the influence of the main parameters such as metal surface, sheet thickness, coating thickness and strain rate on the forming behavior of OCSM was experimentally evaluated. Furthermore, the effect of the coating layer on the deep drawing properties was investigated. It was shown that the microstructure of the substrate surface has a significant influence on the adhesive property. The thicker coating layer results in a better forming behavior than the thinner one. In the cylindrical deep drawing process, the thinning value in case of the forming with coated sheet was larger compared to the one of the uncoated cylindrical cup. The reason for this is that the organically coated layer acted as lubricant and this could reduce the friction coefficient between the punch and the sheet metal.

Bräunlich et al. (1998) evaluated the forming behavior of OCSM under production conditions. In this contribution, the formability of organic coated sheet is experimentally investigated. Bending, folding, embossing, deep drawing and some other tests were conducted. The coating performances after forming such as gloss loss, coating tear-off were inspected. The minimum bending radii, the maximum deep-drawing depth, the allowable folding radii were determined. Additionally, the decrease of the gloss property depending on the roughness value after forming was evaluated. This investigation provided a means to evaluate the forming behavior and the coating performance after forming.

By using an electrochemical approach, *Bastos et al. (2004)* presented a correlation between the coating resistance and the equivalent plastic strain in case of uniaxial, biaxial and plane strain of the PES and PUR coatings. Accordingly, the mechanical deformation of organic coated steel causes a reduction of anti-corrosive protection properties, which is due to a loss of adhesion at the polymer/substrate interface. It was shown that the protective properties of the coated system decrease with increasing strain. At low plastic strain, the coating resistance decreased logarithmically with the equivalent plastic strain. Meanwhile the changes in the coating resistance were much smaller, ultimately leading to the loss of adhesion to the pigment particles at higher strains.

Schikorra et al. (2002) submitted the contribution related to the prediction of the surface quality based on the strain state of the steel substrate. A system consultation was developed in order to obtain a prognosis of the formed product's surface qualities. Three organic coated sheet metals namely PUR, PES and EP were investigated by using the notch tensile test and

Erichsen cupping test. Coating performances such as loss of gloss, brightness increase, cracking, adhesion failure and corrosion resistance were evaluated. The FLD of the correspondent steel substrate was established. The coating performances depending on the plastic deformation were determined by correlation of the coating failures and the steel substrate's strain. However, this investigation has only focused on uniaxial tension and a pure deep drawing strain state.

2.2.2.3 Application of FEM for forming of OCSM

Since the beginning of the 1970s, the finite element (FE) simulation has been applied in sheet metal forming in order to optimize and design the forming process in the forefront of tool construction.

A first investigation concerning the application of FEM in sheet metal forming in two dimensional cases has been contributed by *Wifi (1976)*. Since the beginning of the 1980s, the first three-dimensional models have been successfully obtained, *Tang et al. (1982)* and *Toh & Kobayashi (1983)*. Until now, the application of FEM in sheet metal forming has been characterized by a rapid development. Depending on the time integration, the FE algorithms can be divided into the following approaches:

- one-step
- explicit and
- implicit method.

The quality of an FE simulation depends on the algorithms and modeling of the FE mesh. A sustainable improvement of the whole model requires an improvement of all sub-aspects. The simulation results allow the designer to predict the product properties such as strain and thickness distributions; failure indicators for wrinkling, fracture; spring-back phenomenon etc. Hence, the time and cost of the manufacturing loop "Trial – and – Error" are considerably reduced, *Lange (1990)*.

Before 1995, the use of the FEM to determine the coating failure of pre-painted steel sheets during forming, especially in deep drawing processes was not referred to in the literature. The reason is the high computational cost to be expected for a complete modeling of the substrate and the coating system, *Keßler (1996)*.

As a pioneer contribution, *Keßler (1996)* investigated the working area and predicted the coating failures of OCSM by using a numerical method. The cylindrical and square cup deep drawing process using PUR coated sheet metal was experimentally conducted in order to determine the coating failures such as cracking. The correspondent deep drawing processes were also simulated by using the FE code INDEED. The multi-layer shell element was proposed for the modeling of both steel substrate and coating layer. These simulations were performed by using a simplified model that only consists of a steel substrate. The reason is the limitation of the simulation software and the modeling of the organic coated material on account of the relatively large thickness ratio between the steel substrate and the coating layer at that time. As a result, the large thickness ratio will lead to a large aspect ratio in the FE mesh. That is the cause of inaccurate computation and time consuming. Thus, the prediction

of the coating failures after forming was based on the strain states and the FLD of the steel substrate.

Van der Aa et al. (2000) and Van der Aa et al. (2001) investigated the wall ironing process of polymer coated aluminum and polymer coated sheet metal. Simulations of the ironing process were performed by using a two-dimensional plane strain model in the FE code MARC. The constitutive behavior of the metal substrate polymer was modeled with a generalized compressible *Leonov* model. In the case of PET coated material, the model is represented by a *Maxwell* element with an *Eyring* viscosity describing a small strain elastic response, followed by yield and intrinsic softening. Subsequent hardening behavior due to molecular orientation is modeled as a neo-Hookean spring. A similar *Maxwell* model with a modified *Bodner-Partom* viscosity function was used to describe the elasto-viscoplastic behavior of metal. For the coated specimens, perfect adhesion is assumed on the interface between metal and coating. Three elements were used through the thickness of both substrate and coating. The thickness of the steel substrate and the coating layer is 0.26 mm and 0.03 mm, respectively. The influence of the die angle, the ironing velocity and the ironing reduction on the process forces and friction were evaluated. This investigation has proved the fact that it is possible to consist of both the steel substrate and the coating layer in only one FE model, despite of large differences in their thicknesses. Additionally, it provided a good means for future investigations, particularly with regard to the simulation of the forming process with OCSM.

The computation strategies for the simulation of the deep drawing process using PET coated steel sheet on both sides were developed by *Owen et al. (2007)*. Similar to the investigation of *Van der Aa et al. (2001)*, the single-mode compressible *Leonov* model was used for the description of the constitutive behavior of polymer. For the steel substrate, the Hill's orthotropic criterion was employed for the description of the metal substrate, which is coupled with a ductile damage evolution law. Low order elements were used for the modeling of both the substrate and coating layer. This investigation has shown a good suitability of the developed strategies. However, no consideration is given to the interface area between the steel substrate and coating layer i.e. adhesion properties. Furthermore, there is no comparison between the numerical and experimental results to validate the developed strategy.

Clearly, all the observations have shown that numerous attempts with regard to the coating performances depending on the deformation were conducted. Nevertheless, most research activities focused on corrosion protection or the delamination phenomenon. Some investigations have dealt with loss of adhesion, recovery of coated steel, coating durability under external conditions or forming behavior. Less attention is given to the industrial forming process of coated sheet metal, especially in the field of the change of optical properties after forming processes.

2.2.3 Hydroforming technique and OCSM

The working-media based forming technique or the so called hydroforming technique is a well-known process which was employed first to form sheets by the use of a liquid as a soft punch before World War II. Nowadays, the hydroforming technology is widely used for forming lightweight or complicated components in the automotive and aerospace industry etc. Due to many advantages compared to the conventional method, this forming technique has

gained increased interest in the industry. Furthermore, the fields of application have become broader, *Lang (2004c)*.

Depending on the process features and the usage of original blanks, the hydroforming process is basically classified into two groups, namely tube and sheet hydroforming. Depending on whether a punch or a die will be used to form the sheet, the sheet hydroforming is further divided into two sub-groups, namely hydroforming with a punch (SHF-P) and with a die (SHF-D). Depending on the number of blanks being used, the SHF-D is further divided into hydroforming of single blanks and double blanks, *Nakagawa et al. (1997)*, *Homberg (2000)*.

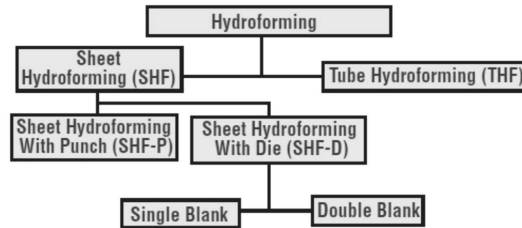


Fig. 2- 15: Classification of the hydro-forming technique, *Yadav (2006)*

The hydro-mechanical forming technique, also known as sheet hydro forming with punch (SHF-P), is nowadays gaining more and more interest in industry, *Lang (2004c)*. The working principle of this method is shown in Fig. 2- 15. Due to its characterization, this forming technique is extremely suitable for forming of OCSM.

In HDD, the female die which is used in conventional stamping is replaced by a pressure tank. The sheet metal is formed over the punch surface under the acting of the hydraulic counter pressure in the pressure chamber, generated by a pressurizing fluid. During the forming process, the fluid pressure is gradually increased and it depends on the punch travel and the control valve settings. To avoid the leakage of the fluid, a sealing ring is set up near the radius on the draw die. Based on the working of the fluid in the pressure tank, this process can be divided into two groups: active and passive hydro-mechanical forming, *Homberg (2000)*.

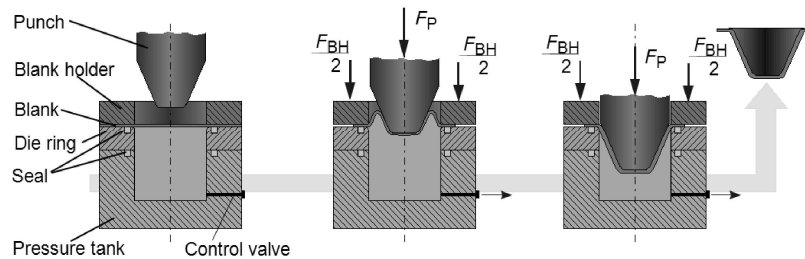


Fig. 2- 16: Schematic present action of hydro-mechanical forming process, *Homberg (2000)*

For the active forming, the fluid pressure is created by an external pump in order to form sheet metal and thus increase strain hardening. In hydro-mechanical forming, the fluid pressure is generated during the forward travel of punch and controlled by a relief valve.

During the forming process, the value of the fluid pressure is in a range of 5 to 100 MPa, depending on the geometry and material used. For aluminum, this value is controlled from 5 MPa to 20 MPa; from 20 MPa to 60 MPa for steel and from 30 MPa to 100 MPa for stainless steel, *Lange et al. (1990)*.

The range of components, which can be manufactured with this forming technique, is very wide, e.g. from structure parts made of high-strength steel up to large-scale outer surface parts made of aluminum and its alloys. In comparison with the conventional forming techniques, the hydro-mechanical forming method possesses many advantages, as follows, *Homberg (2000)* and *Khandeparkar (2007)*:

- *Higher achievable drawing ratio (β , max) compared to conventional deep drawing process (can be reached at the value of 3)*, because the friction between blank and outer surface of punch is gradually increased and it depends on the punch travel and the punch speed. The greater the counter pressure, the greater the friction between the deep drawing part wall and the punch, which is the main reason for the increase of the drawing ratio as per Coulomb's friction law. An increasing counter pressure results in a corresponding increase of the maximum draw ratio.
- *Better surface quality*, because the outer surface of the blank is in contact only with the hydrostatic medium. Hence, no friction occurs between the sheet metal and a lower die.
- Moreover, it is possible to manufacture sheet metal parts with tapered-shaped walls without wall wrinkles. This can be done by optimizing the counter pressure in dependence on the punch travel. Products with a tapered shape can only be produced by conventional deep drawing if a multi-stage process is used. Using the HDD process, complicated shapes such as conical, parabolic geometries can be produced with a minimum number of forming stages and local thinning is minimized, Fig. 2- 17 and Fig. 2- 18.
- *Decreasing of the spring-back phenomenon* due to higher strains and a nearly even strain distribution over the part surface.

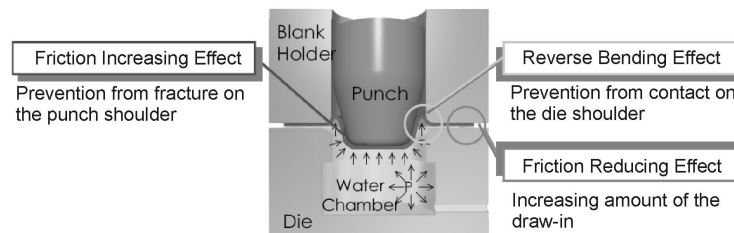


Fig. 2- 17: Characterization of HDD process, Hama et al. (2007)

- *Dimensional accuracy* is higher than if using the conventional deep-drawing technique.
- *Tooling cost reduction* since pressure chamber does not need to satisfy the precision and tolerance requirements of deep drawing tools.

- *Better flow of sheet* due to the action of the fluid pressure reduces the friction at the interface between the work piece and drawing die.
- *More uniform thickness* of the forming part at the end of the forming process due to the increased friction between the punch and the sheet.

On the other hand, disadvantages of this technology require some additional investment such as the high ram force press with an external hydraulic system in order to generate and regulate the counter pressure. Hence, the cycle time for the production is higher than with conventional forming. The reason is the limit of the maximum valve flow rate and the time for filling up the pressure tank. Furthermore, the product surface must be cleaned after the forming process.

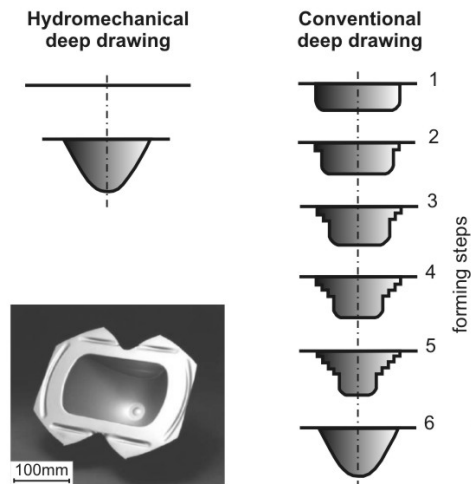


Fig. 2- 18: Advantage of HDD compared to conventional deep drawing, Bürk (1963)

In the HDD process, the final quality of the product can be influenced by many different parameters such as counter pressure, BHF, pre-bulging phenomenon, friction and material properties, *Ceretti et al. (2005)*. During the forming process, these parameters should be controlled together and can be varied together with the punch travel to produce defect free parts. Furthermore, the relations between the BHF and the counter pressure in the water chamber with respect to the punch travel are also the key parameter in order to optimize the process. In other words, the BHF can be defined by using the pressure path and that is a simple way for understanding the correct force, *Khandeparkar (2007)*. The limits of both parameters in which the HDD process operates successfully and without failure are known as “Process Limit” and the region within the limit is called the “Forming Window”, see Fig. 2-19.

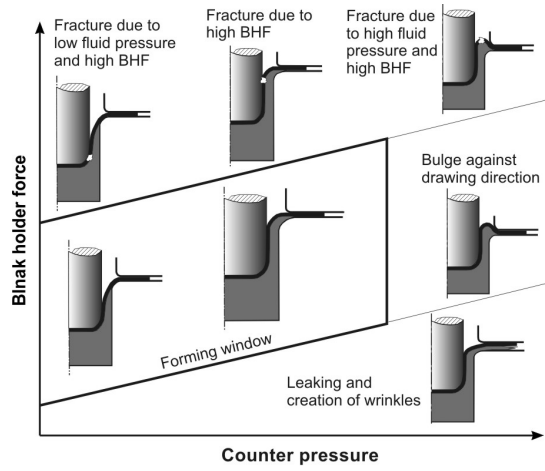


Fig. 2- 19: Forming window of HDD process, Palaniswamy (2006)

The counter pressure and the BHF play an important role and significantly influence the strain distribution of the part. These are the key parameters for a successful HDD process. The sheet metal is in direct contact with the oil or water in the pressure chamber instead of the female die so that the counter pressure acts as an essential factor to adjust the deformation of the deformed parts, Fig. 2- 20.

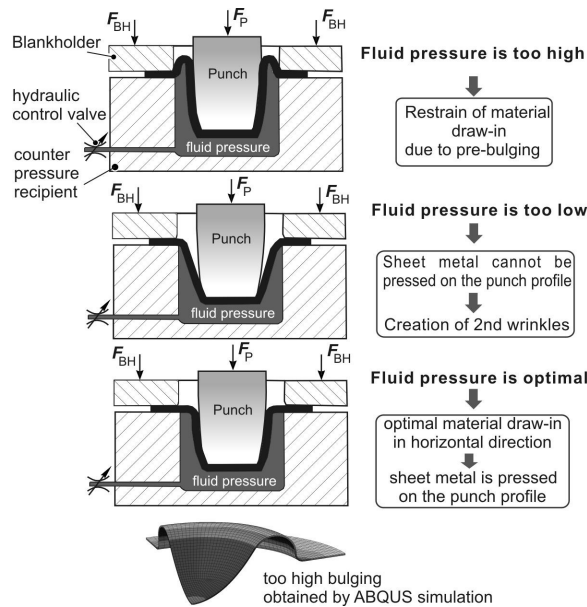


Fig. 2- 20: Influence of counter pressure on the quality of product, Doege & Behrens (2007)

As can be seen, if the counter pressure is too high, it will restrain the material flow during the forming process and lead to either pre-bulging against the drawing direction or fracture of the sheet metal. If the counter pressure is not sufficient, the sheet metal will not fit tightly on the punch profile and it will lead to sidewall wrinkling of the final product.

The form of the pressure curve and the BHF, which depend on the punch travel, are the key factors in the HDD process. A high counter pressure is not advisable at the beginning of the punch travel on account of the small available area of force transfer. Higher pressure at the beginning of the process, however, leads to excessive material thinning. It is indicated that an increase of the counter pressure at higher drawing depths results in a higher part accuracy and lower spring-back, *Khandeparkar (2007)*.

In Fig. 2- 21, three exemplary pressure curves depending on the punch travel used in the HDD process are recommended.

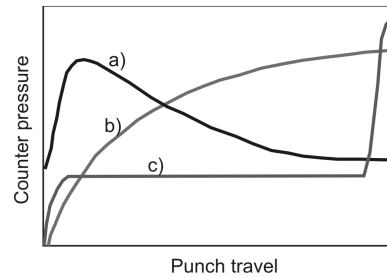


Fig. 2- 21: Exemplary pressure curves in HDD process, *Lange (1990)*

Among these, the curve (a) shows a rapid increase at the beginning of the process and a gradual decreasing. This curve results in a high tensile stress at the beginning, low process stability, possibility of blank rupture, lower part accuracy and lower limited drawing ratio (LDR). The advantage of the curve (a) is to optimize the formability of the sheet metal and minimize blank thinning. The pressure curve (b) shows the low value of the counter pressure at the beginning of the process and the gradual increasing afterward. This results in an increase of the tensile stress with increasing drawing depth. Using this curve will provide higher strain in the sidewall area of the forming part, lower thinning of the sheet and higher LDR and optimal formability. The pressure curve (c) shows a relatively low pressure rise at the beginning and a sharp rise at the end of the forming process. As a result, the tensile stress is relatively low at the beginning of the process and increased at the end. The pressure curve (c) is utilized in order to get lower blank thinning, high process stability, higher shape accuracy and higher strain in the side wall area of the forming part.

It is recognized that sheet metal bulges in the unsupported region between the punch and the blank holder in the direction opposite to the drawing direction. The sheet metal is thus lifted from the drawing die radius and flows over a fluid cushion. The bulge is an important advantage since it can result in a reduction of the friction and bending force at the drawing die radius. On the other hand, the bulge can also lead to double bending of the sheet. Under extreme conditions i.e. at high counter pressures, the bulge is clamped between the punch,

blank holder, which results in rupture, *Khandeparkar (2007)*. Some researchers have also investigated several methods of controlling the bulge height by employing modifications in the die system, *Bürk (1963)* and fluid pressure instead of a rigid mechanical device, *Siegert & Ziegler (1998)*. By using this system, the bulge height can be actively controlled along the punch travel.

Numerous research works related to HDD processes have been experimentally and numerically investigated so far, *Kleiner (2006)*; *Lang et al. (2004c)*. Most research activities have focused on the increase of shape and dimension accuracy of the parts, *Herold (1984)*; the increase of the formability of high strength materials such as magnesium and magnesium alloys, *Bach et al. (2006)* or very thin sheet metals, *Wellendorf (2003)*; the simulation of the HDD process, *Zhang et al. (2000)*; *Jensen et al. (2001)*; the modeling of oil pressure distribution, *Jensen et al. (2000)*; sealing technique in order to prevent the liquid from escaping during the HDD process, *Celeghini (2001)*; or counter pressure control technique, *Aust (2003)*. Many investigations have dealt with the modification of the HDD process such as the application of the elastic blank holder system in order to form the very complicated parts in the automobile industry, *Siegert & Aust (2001)*; combination of the HDD and conventional forming technique, *Wagner (2001)*; using a heated die and cooled punch in combination to form aluminum alloys, *Groche et al. (2002)*; *Groche et al. (2005)*; using the HDD process for forming magnesium alloys at elevated temperature to increase the deep drawing ratios, *Jäger (2005)*; using tailor welded blanks in the HDD process, *He 'tu (2006)*; using multi-layer sheet hydroforming, *Lang et al. (2005)*. Some contributions have focused on the influence of process parameters such as the effect of anisotropy and pre-bulging during the HDD process, *Zhang (2003)*.

Further contributions have focused on the development of analytical models for the HDD process in order to determine the rupture and wrinkling instability and also the working zone based on plane strain criteria and the energy method, *Yossifon et al. (1985)*; *Lo et al. (1993)*. *Dariani et al. (2006)* and *Azodi et al. (2008)* investigated theoretically and experimentally the influence of geometrical and material parameters on the critical fluid pressure. In this contribution, the lower bound of the fluid pressure was also presented. *Reddy et al. (2006)* developed a mathematical model for the prediction of the bounds of the BHF and fluid pressure to avoid tensile and compressive instabilities in the HDD process. *Bakhshi-Jouybari et al. (2009)* investigated the tearing phenomenon in the cylindrical HDD process by developing an axisymmetric analysis combined with the FE method. The critical fluid pressure which results in tearing was investigated. In another research, *Choi et al. (2007)* developed analytical models for warm HDD of lightweight materials. The effect of temperature, fluid pressure, BHF and forming speed were investigated.

2.3 Conclusion

The processing of OCSM by forming processes induces large deformations in both the steel substrate and the coating layer. This consequently results in topographical changes on the surface of both materials. As a result, this may lead to coating failures such as cracking, scratch, gloss decrease and delamination of the coating layer off the steel substrate. The occurrence of the coating failures leads to a loss of optical and protective properties.

The literature survey concerning the forming of OCSM indicates that the prediction of the coating performances i.e. optical properties and coating failure such as cracking depending on the deformation level and strain state is a so far unsolved problem. In addition to this, the knowledge of the relationship between the surface roughening, gloss reduction and deformation afterwards is a crucial need in industry.

Processing of OCSM requires forming processes which maintain the functional properties of the organic coating. HDD is a hydro-forming process that allows higher drawing ratios, lower springback, a better geometrical accuracy, homogeneous deformation and excellent surface properties due to the presence of working media. Despite of the fact that HDD offers promising properties for forming OCSM and numerous investigations concerning the HDD process have been contributed. However, less attention is paid to the use of the counter pressure and the BHF for the adjustment of the strain distributions in order to obtain the desired optical property of the OCSM products. Furthermore, fundamental knowledge about a material-specific process design for OCSM is not available. As a result, it remains and opens further research subjects.

3 Research aims and objectives

The goal of this thesis is fundamental research for a material-specific process design for processing organically coated sheet metal (OCSM). Therefore, the determination of the influences of strain states and strain levels on the functional properties of OCSM parts is essential. This knowledge can be used in the frame of a numerical process design in order to optimize the forming process for OCSM. For this, an approved FE-based modeling strategy for the simulation of the forming process of the OCSM is required which allows the prediction of surface properties of OCSM. The achieved knowledge will be applied for the process design of Hydro-mechanical deep drawing (HDD), supplying fundamentals about the influence of process parameters of the HDD process on the product properties as well as process control strategies.

In order to achieve these research goals, the following objectives are identified. Fundamental investigations of the forming behavior of the OCSM during the forming process are presented in chapter four. The forming limit diagram (FLD) of OCSM is established by combining the FLD of the steel substrate and the forming limit diagram of coating (FLDC) of the coating layer. The changes of the surface properties as a function of plastic strain i.e. strain states and deformation levels are also reported. The relation between the optical properties and the plastic deformation is established by using the Nakajima test. The surface roughness of both the steel substrate and coating layer depending on the strain state as well as strain level is determined for the interpretation of the change of optical properties. These relations act as the reference data and will be used to evaluate the change of surface properties after forming processes. The influence of the thermal treatment on the coating performances such as gloss property and cracking effect is also evaluated.

The simulation strategy for the computation of the industrial forming process of the OCSM is considered in chapter five. Here particularly, the mismatch of the deformation states between the coating layer and the steel substrate is of interest. The material modeling of the coating layer as an elastomeric material and the procedure for the determination of the material parameters are briefly presented. The developed simulation strategy is first applied to axisymmetrical cases such as hydraulic bulge test and deep-drawing test. The potential and the feasibility of the proposed strategy are later verified by three-dimensional (3D) analyses. In this section, the prediction of changing optical properties and the coating defect i.e. cracking based on the experimentally and numerically results are presented.

In chapter six, the influences of the processing parameters of the HDD forming technique such as the counter pressure, the BHF on the surface quality i.e. gloss reduction of OCSM products are investigated. The obtained results of the Nakajima test are utilized as evaluation criteria. An analytical model of the HDD forming process established by *Lo et al. (1993)* is adapted to parabolic geometries and utilized in the frame of a developed *MATLAB* tool which allows the computation of the strain distribution depending on process parameters. Using this tool, a fundamental understanding of the influencing process parameter setting on the strain distribution could be provided. This knowledge is validated by the HDD forming process of

the OCSM parabolic reflector part. The influence of process parameters on the surface quality is investigated numerically and experimentally.

In the last chapter, the principal results of this study are summarized. Based on these research outcomes, the process scope is reported. Finally, overall conclusions are drawn and recommendations for further researches are given.

4 Influence of strain states and strain level on surface properties of OCSM

In this chapter, the influence of occurring strain states and strain levels on the functional surface properties of OCSM are investigated. Firstly, the experimental set-up and the feasible studies for the determination of the FLD of OCSM are described. Furthermore, the changes of optical surface properties depending on the strain states and strain level are discussed. Then, the corresponding relationship between gloss reduction and plastic strain is established. Additionally, the influences of the process parameters such as thermal treatment on the change of the surface properties are also discussed.

4.1 Materials used

The materials used in this research are mild steel sheet with black polyurethane (PUR) and white polyester (PES). The PUR coated sheets consist of a two-side coating layer i.e. a PUR coating on the decorative side and a protective layer on the other side. The PES coated sheets consist of only one decorative coating layer. The steel substrate for the PUR and the PES coated sheet are DC04 and DX51, respectively.

The PUR coated materials feature high gloss properties. The PES coated feature medium gloss. These coated materials offer the elasticity of rubber combined with the toughness and durability of metal. Furthermore, there are many advantages to use PUR and PES. Both of them offer a wide range of hardness values, an excellent resistance to oils, excellent electrical insulating properties etc. In addition, they have a better abrasion and tear resistance than rubbers and especially offer a high load bearing capacity. Most PUR and PES products offer an extremely high flex-life and can be expected to outlast other elastomer materials where this feature is an important requirement, *Schulze (1994)*. Both PUR and PES coatings offer a good formability in bending and deep drawing. The characteristics of the investigated coated materials are briefly summarized in Table 4- 1.

Table 4- 1: Properties of the PUR and PES coating layer

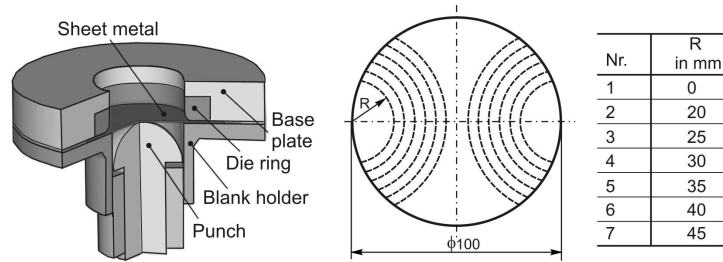
Properties	Unit	PUR	PES
Tensile strength	DIN, N/mm ²	< 40	18.2 - 60
Elongation at break	DIN/ %	< 500	< 300
Tensile Young's modulus	DIN, N/mm ²	< 650	
Rockwell-Hardness	Shore-Hard.	68-99A	
Surface hardness		good	very good
Formability/bending		good	good
Formability/drawing		excellent	good
Colour		black	white

4.2 Forming limit diagram (FLD) and forming limit diagram of coating (FLDC)

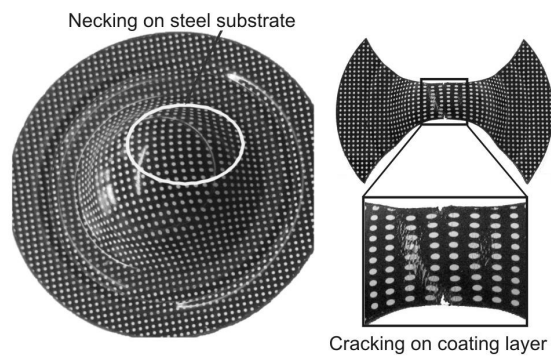
As a failure criterion for sheet metal forming, FLDs are often used. The FLD is a strain-based criterion which is performed on the material under different straining conditions until the

specimens develop necking, which finally leads to fracture or defects on the specimens. Hence, the FLD delineates the boundary of strain and onset of local necking, *Van Tyne et al. (2005)*.

In this section, the FLD and the forming limit diagram of coating (FLDC) are first established in order to evaluate the formability of both the steel substrate and the coating layer.



a) Experimental set-up and specimens of Nakajima test



b) Necking on substrate and cracking effect on coating layer

Fig. 4- 1: Experimental set-up and specimens for Nakajima test

According to the *Nakajima test*, a hemispherical punch with a diameter of 50 mm will deform circle OCSM specimens with a diameter of 100 mm. These specimens are grooved at different radii ($R = 0, 20, 25, 30, 35, 40, 45$ mm, see Fig. 4- 1a) in order to create different states of stress and strain. Five series of the *Nakajima test* were performed on an *Erichsen* universal testing machine to provide data for both FLD and FLDC diagrams. Each series includes 7 specimens with different grooved radii as mentioned above. Speed of the punch is 5 mm/s.

Naturally, the differences in the mechanical behavior between the coating and the substrate material will lead to the differences in their fracture mechanisms. During the forming process, the organic coating exhibits a large elastic deformation while the steel substrate shows an elasto-plastic deformation. Therefore, the fracture mechanisms of the steel substrate and the coating layer have to be investigated separately. Hence, the procedure for establishing the FLD and the FLDC is not the same. For the determination of the FLD, specimens were

stretched until breaking occurred on the steel substrate. Meanwhile, for the FLDC, all the specimens were only stretched until cracking occurred on the coating layer, Fig. 4-1b.

The specimens which were deformed by the Nakajima tests are shown in Fig. 4-2. The strain distribution over the specimens is analyzed with the optical measuring system *Argus* by GOM that allows a strain measurement on deformed parts.

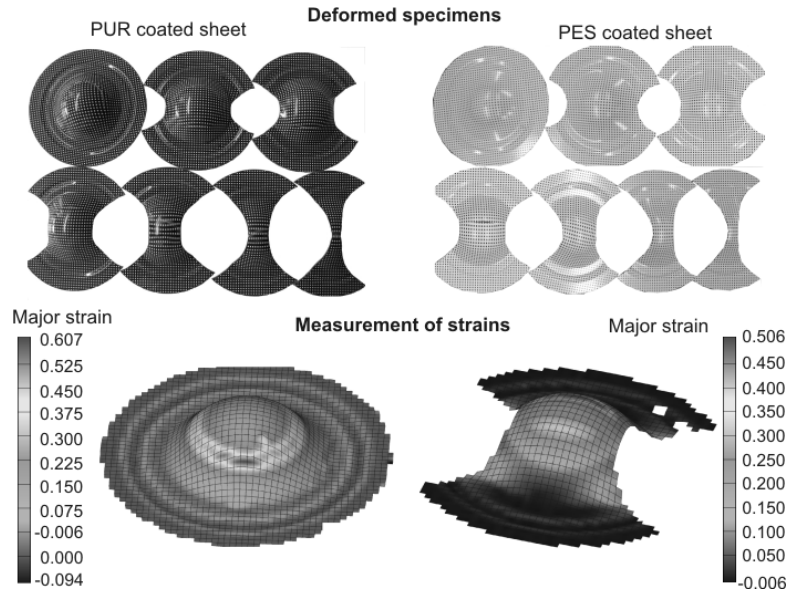
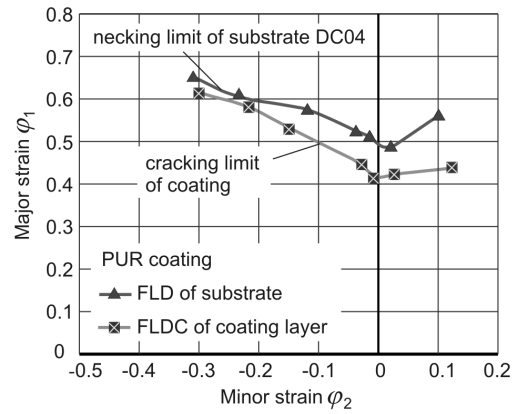


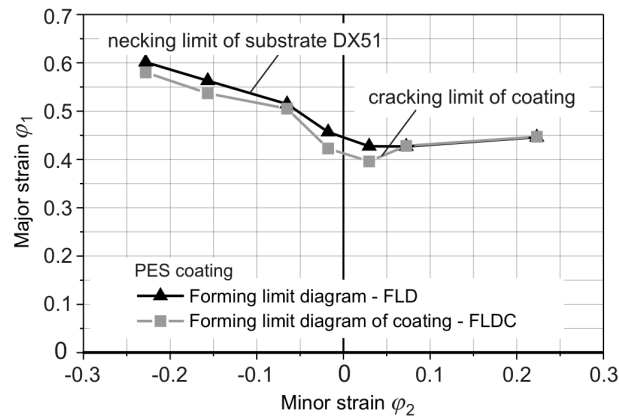
Fig. 4-2: Strain measurement on Nakajima specimens

By using the maximum of the measured first and second principal logarithmic strain φ_1 and φ_2 around fractured areas, the limiting curves, namely FLD and FLDC, are plotted for each specimen. The final result is the average of the data from specimens of five series of the Nakajima tests. The limiting curves represent the border between safe and failure region of forming process. The strain states and strain levels below the determined curves act as *process window* for the whole forming process.

The determined FLD and FLDC for the investigated materials are presented in Fig. 4-3. In the case of PUR coating, the maximal strain value of the FLDC in the case of PUR coating is significantly lower than the one of the FLD. In the case of PES coating, the correspondent strain value of the FLDC is partially coincident with the FLD. The rest part of the FLDC is lower than the strain magnitude of the FLD. It can be observed on the specimens that the cracking effect occurs on the coating layer before the fracture appears on the steel substrate. Therefore, the FLDC should be employed instead of the FLD in order to evaluate the formability of OCSM concerning the surface quality of the coating layer.



a) Forming limit diagram of PUR coated sheet metal



b) Forming limit diagram of PES coated sheet metal

Fig. 4-3: Forming limit diagram (FLD) and forming limit diagram of coating (FLDC) of OCSM

By using these diagrams above, the limitation of any forming state, such as the equibiaxial stretch-forming ($\varphi_1 = \varphi_2$), plane strain ($\varphi_2 = 0$), uniaxial tension ($\varphi_1 = -2\varphi_2$) and deep-drawing zone ($\varphi_1 = -\varphi_2$), is determined.

In order to prove the finding that the coating fails before the substrate, a deep-drawing test was performed. Before testing, the protective coating layer on the PUR coated specimen was removed, but the decorative layer was kept intact. Hence, it is possible to evaluate the behavior of the deformed steel substrate after forming. The obtained results clearly show that the decorative coating layer is fractured while the steel substrate is still intact, without failure, Fig. 4-4.

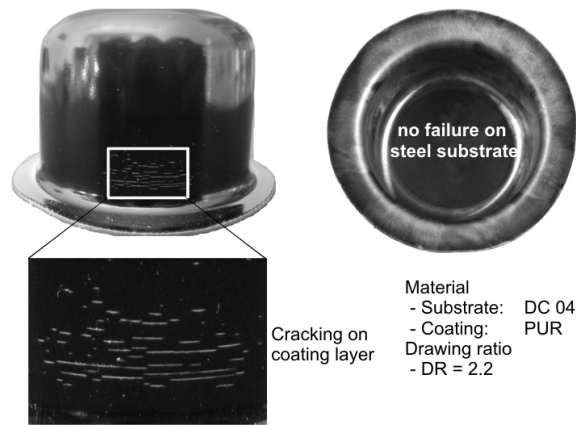


Fig. 4-4: Cracking effect on PUR coating layer

In detail, the coating layer exhibits roughening at first, then cracking. Cracking is caused by rupture of molecular chains of the organic material. After cracking, delamination may happen if the deformation continues. This phenomenon can be explained by the failure mechanism of the organic coating layer on the steel substrate. According to this, mechanical stresses imposed on the coating material and the metal substrate (being in large plastic strains) will lead to coating failures. Among these induced failures, in-plane stresses are the cause of the defect of the coated material, i.e. cracking or roughening. Out-plane stresses are the reason for the loss of adhesion and they may lead to a debonding effect between two layers. On the other hand, large plastic strains in the steel substrate cause the loss of adhesion at the interface and may also lead to delamination in further processing, *Wang & Vayeda (2007)*; *Boelen et al. (2004)*. In addition, residual stresses in the coating resulting from plastic strains in the metal substrate may lead to an additional shear stress at the interface and this is the cause of the aggravated defect of the coating layer, *Polyakova et al. (2000)*. Applying this failure mechanism to the deep-drawing test carried out, the defects of the coating layer were obviously caused by the mechanical in-plane stress and the large plastic strains in the steel substrate.

4.3 Gloss reduction depending on plastic deformation

4.3.1 Principle of gloss measurement

Gloss is one of the most important criteria to evaluate the surface qualities of OCSM parts. The term “gloss” is based on the interaction of light with physical characteristics of a surface. It is actually the reflection of the light into the specular direction when a certain light is radiated on the surface. The standard gloss unit is (*GU*). The gloss reduction can be analyzed by the method which is described by *DIN ISO 2813 (1999)*. The gloss reduction is measured by means of a gloss meter, namely *reflector meter*. The general principle of the gloss measurement is illustrated in Fig. 4-5.

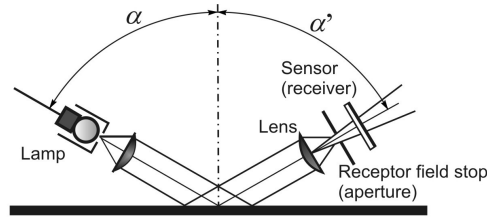


Fig. 4-5: Principle of gloss measurement

The common irradiation angles of incidence for the gloss measurement are 20° (for high gloss surfaces), 60° (for medium gloss surfaces) and 85° (for low gloss surfaces). Two types of gloss measurement apparatuses were used, one for measuring the gloss of flat surfaces and the other one for measuring the gloss of curved surfaces.

To characterize the change of the gloss property, the gloss values of the OCSM before being formed are measured and denoted by G_o . The updated gloss values after forming are measured afterwards and denoted by G_i ($i = 1, 2, 3, \dots$). The deviation of these values is denoted by ΔG and computed as follows:

$$\Delta G_i = G_o - G_i \quad (4.1)$$

The relative loss of gloss, which is denoted by LG , is defined by the following equation:

$$LG_i = 100 \frac{\Delta G_i}{G_o} = 100 \frac{G_o - G_i}{G_o} \text{ (in \%)} \quad (4.2)$$

According to equation (4.2), the maximum and minimum loss of gloss can be determined as follows:

$$LG_{i_min} = 100 \frac{G_o - G_{i_max}}{G_o} \text{ (in \%)} \quad (4.3)$$

$$LG_{i_max} = 100 \frac{G_o - G_{i_min}}{G_o} \text{ (in \%)} \quad (4.4)$$

4.3.2 Relationship of gloss reduction to strain magnitude and strain states

To evaluate the gloss reduction of the coating layer depending on the deformation process, the Nakajima tests are performed at predefined depths i.e. different strain levels. Subsequently, the respective strain states over specimens are measured and denoted by H_i ($i = 1 : n$). The corresponding gloss reductions are recorded by the NOVO-Curve equipment and denoted by LG_i ($i = 1 : n$) afterward. This equipment allows the gloss measurement on concave or convex surfaces at an irradiation angle of 60° . Depending on the grooved radius, specimens are numbered from one to seven, see Fig. 4-6.

In order to assess the change of the gloss property of OCSM specimens, the two following cases of the Nakajima test were performed.

- specimens without printed grid on the surface to analyze the gloss reduction;
- specimens with printed grid to analyze the strain states and strain level.

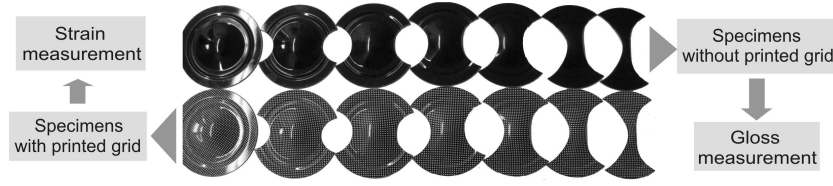
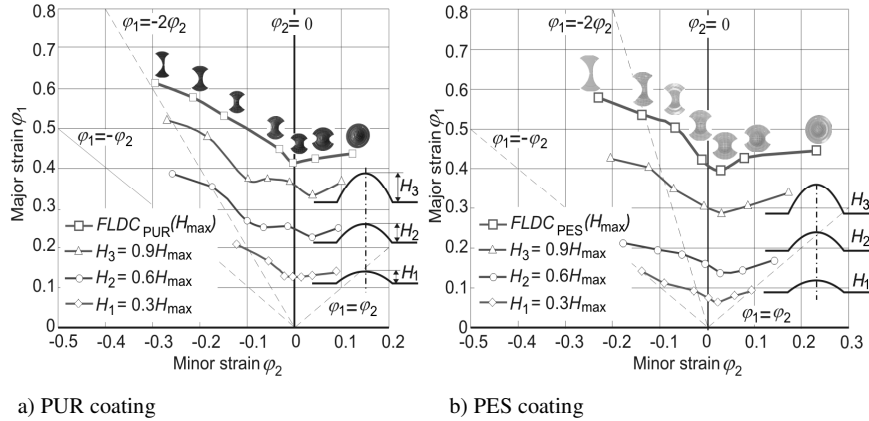


Fig. 4-6: Nakajima specimens for the determination of the strain states and the gloss reduction

The measurement of strain values by the Nakajima tests in the cases of PUR and PES coatings in conjunction with the obtained FLDC are presented in Fig. 4-7.



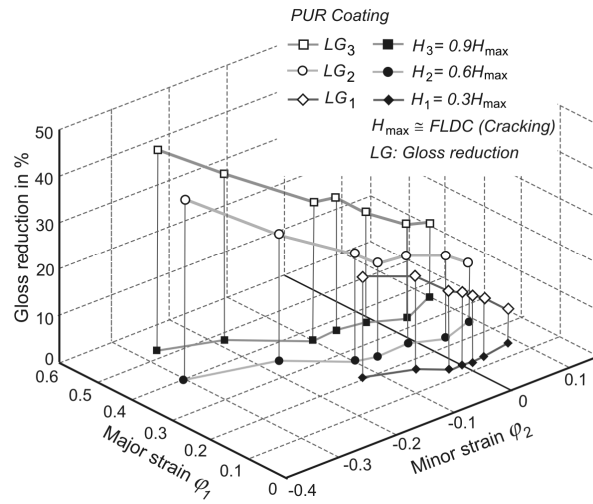
a) PUR coating

b) PES coating

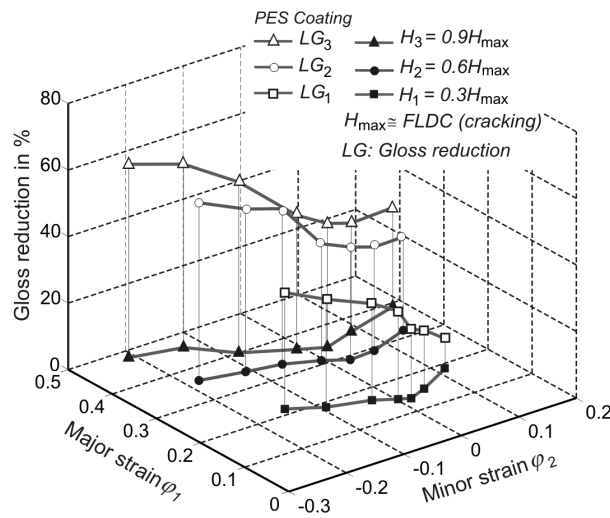
Fig. 4-7: Strain values of PUR and PES coated sheet metal obtained by Nakajima test

In order to ease comparisons, it is conventionally assumed that the strain value at the limited fracture of the coating layers corresponds to 100 % deformation. In other words, all values on the FLDC have the deformation of 100 %, depending on the strain states. Basically, it is necessary to carry out the Nakajima test at the pre-defined strain levels, i.e. 5 %, 10 %, 20 % and so on. For a better illustration, only the strain values corresponding to 30 %, 60 % and 90% are presented. These strain values are denoted by H_1 , H_2 , and H_3 respectively.

The dependency of the gloss reduction on the strain values, i.e. major and minor logarithmical strains of the deformed parts, is shown in Fig. 4-8. In the case of the PUR coating, it can be observed that the loss of gloss of the first case H_1 is not large. The highest gloss value is obtained with the circular specimen (grooved radius $R = 0$). The deformation of those specimens exhibits the balanced stretching state i.e. $\phi_1 \cong \phi_2$. The measured gloss value is $G_{1_max} = 83$ GU (GU means gloss unit). The maximal gloss value results in a minimal gloss reduction. According to equation (4.3), the minimum gloss reduction is $LG_{1_min} = 7.7$ %, only.



a) Gloss reduction depending on major and minor strains of the PUR coated sheet



b) Gloss reduction depending on major and minor strains of the PES coated sheet

Fig. 4-8: Gloss reduction vs. strain states and strain levels

For the first case H_1 , the lowest gloss value $G_{1_{min}} = 70.8$ GU is obtained with the seventh specimen (grooved radius $R=45$), which represents the deep drawing strain state i.e. $\phi_1 = -\phi_2$.

As a result, the lowest gloss reduction leads to the maximal gloss reduction. According to the equation (4.4), this value can be computed as $LG_{1_max} = 21.3 \%$.

Considering the second and the third case which correspond to the higher strains H_2 and H_3 , the gloss reduction trends are seen to be similar to the one of the first case H_1 . In the balanced stretch-forming zone, where the major strain φ_1 equals the minor strain φ_2 , the gloss reduction reaches the minimum value. The losses of gloss in case of H_2 and H_3 are respectively computed as:

$$LG_{2_min} = 13.1 \%, LG_{3_min} = 35.1 \%$$

Similarly, the maximum gloss reduction of the second (H_2) and the third (H_3) case is obtained with the specimens under the uniaxial strain state. The maximum losses of gloss value are:

$$LG_{2_max} = 16.7 \%, LG_{3_max} = 43.0 \%$$

In the case of the PES coating, a similar dependence of the gloss reduction on the different strain levels was obtained. Accordingly, the lowest gloss reduction occurs at the lowest strain level H_1 . The gloss reduction is then increased with increasing deformation. For ease of reference, the extreme gloss reductions in the case of PES and PUR coatings are summarized in Table 4-2.

Table 4-2: Summarization of measured gloss reduction in case of PUR and PES coating

Deformation level	Measured gloss reduction in %			
	PUR Coating		PES Coating	
	LG_{i_min}	LG_{i_max}	LG_{i_min}	LG_{i_max}
$H_1 = 0.3H_{max}$	7.70	21.30	9.02	34.98
$H_2 = 0.6H_{max}$	13.10	35.10	28.07	53.43
$H_3 = 0.9H_{max}$	16.70	43.00	29.78	58.12

According to Table 4-2, the data of both coatings show that the lowest gloss reduction is obtained at the lowest strain level H_1 . When the deformation is continuously increased, the gloss reduction is increased too and the highest value is obtained at the highest strain level H_3 . Obviously, it can be concluded that the loss of gloss depends on the occurring strain level over the formed parts.

In order to separate the influence of strain level and strain state, Fig. 4-9 and Fig. 4-10 show the dependencies of the gloss changes on the strain states and the equivalent plastic strain $\bar{\varphi}$. For reference reasons, the different strain states are taken into consideration by using strain ratio, which can be calculated by $\beta = \varphi_2 / \varphi_1$.

By comparing the gloss reduction at a similar equivalent strain, it is seen that the equibiaxial strain state always provides the lowest gloss reduction. In contrary, the uniaxial and deep drawing strains result in a higher loss of gloss. The gloss reduction is seen to be gradually increasing from the equibiaxial state to the other strain states, i.e. plane strain, simple tension and deep drawing. Obviously, compressive strains lead to a significant decrease of the gloss values. This effect can be seen on both investigated materials.

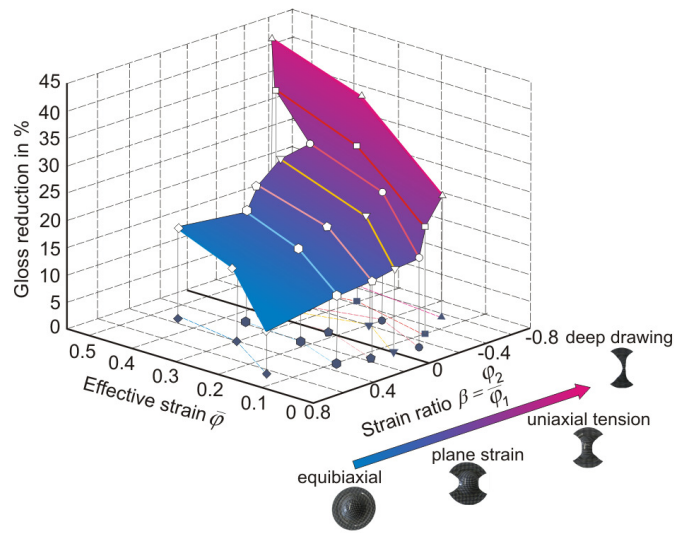


Fig. 4-9: Gloss reduction versus strain ratios and equivalent strain of the PUR coating

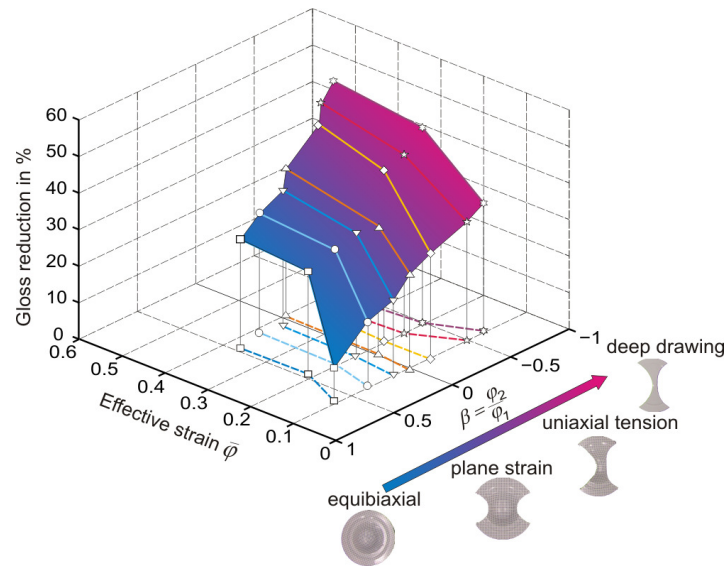


Fig. 4-10: Gloss reduction versus strain ratios and equivalent strain of the PES coating

A comparison between the results in Fig. 4-9 and Fig. 4-10 also indicates that the gloss reduction of the PES coating is higher than that of the PUR coating on account of the thinner

steel substrate and coating layer. This is because the roughness of the thinner steel substrate is larger than that of the thicker substrate. The detailed explanation of the presented results will be given in the following subchapter.

4.4 Deformation induced changes in substrate and coating

The formability of OCSM depends on a number of different parameters such as steel substrate surface, thickness of the coating layer and the substrate, strength and texture of the metallic substrate, strain rate, cohesion between steel substrate and coating layer, *Fischer & Klein (1971)*. Among these, the steel substrate surface and the cohesion are the critical factors that reveal significantly the influences on the gloss degree and the delamination. In this section, the fundamental understanding of the relation between the deformation, the appearance of the steel substrate and the coating layer are investigated.

The investigated Nakajima specimens are continuously utilized to tackle this task. In order to evaluate the topography changes in the steel substrate, the PUR and PES coating layers are removed by using a special paint removing composition, namely Dichlormethan – CH_2Cl_2 . The PUR coating layer is much more difficult to be removed than the PES coating layer. Therefore, this work was carried out by the project partner *Voestalpine GmbH*. After removing the coating layer of all specimens, the steel substrate surfaces are analyzed by means of a confocal 3D microscope, namely *NanoFocus* and *Zeiss* microscope.

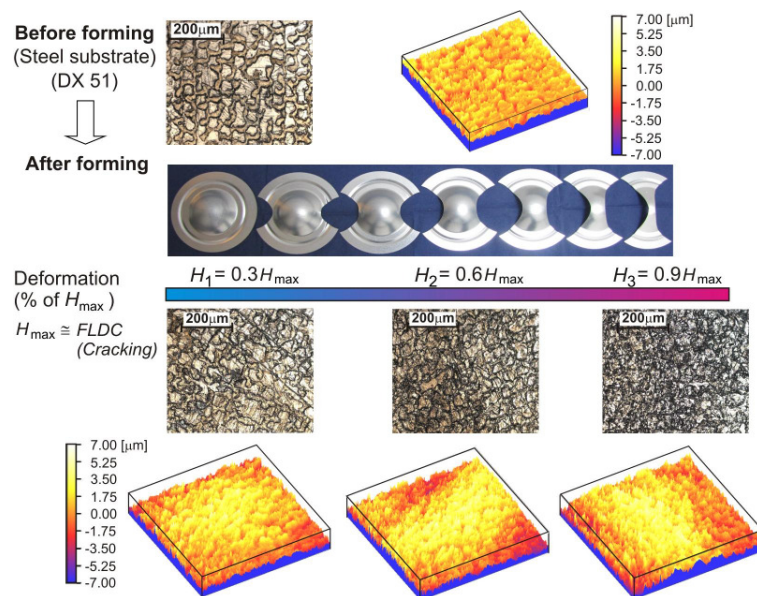


Fig. 4-11: Topographic change of the steel substrate (DX51) in case of PES coating

In Fig. 4-11 and Fig. 4-12, the topography changes of the DX51 and the DC04 steel substrates, that correspond to the PES and PUR coated materials, are displayed, respectively.

For ease of reference, the microstructures before and after forming are depicted with 2D and 3D pictures.

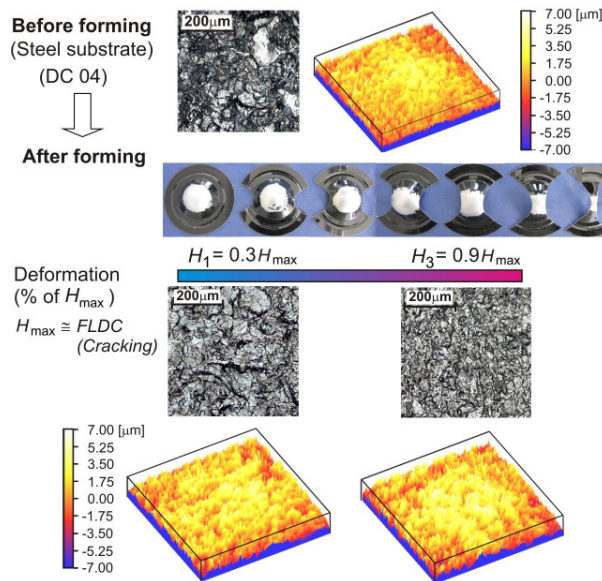


Fig. 4-12: Topographic change of the steel substrate (DC04) in case of PUR coating

During forming operations, the sheet metal undergoes different deformation modes. The resulting surface topography of the steel substrate is dependent on the type of deformation imparted, *Van Tyne et al. (2005)*. Here, it is seen in Fig. 4-11 that the surface structure of the steel substrate is affected by plastic deformation. The initial micro structure of the DX51 steel substrate significantly shows a texture structure which is inserted during skin pass rolling. At a low strain level i.e. $H_1 = 30\%$ of the maximum pole height in the *Nakajima* test, no considerable changes occurred. That means the texture structure is still observed on the surface of all specimens. With increasing strain levels, the micro texture structure is visibly affected. When the strain level reaches a value of 60% of the maximum pole height in the *Nakajima* test, the texture nearly disappears and the surface of the steel substrate is slightly flattened. At a higher strain level i.e. 90% of the maximum pole height in the *Nakajima* test, the micro texture structure of the DX51 substrate has definitely disappeared.

The similar tendency of the topography changes was observed on the DC04 substrate of the PUR coated sheet. Compared to the hot dip galvanized DX 51, where skin pass rolling was done in a final production step at the end of the hot dip galvanized line, the micro structure of the electro galvanized DC04 is different. Here the carbon steel was skin passed prior to the coating process and fine microstructure of the EG coating makes it difficult to detect the subjacent skin pass structure. The topography changes on the steel substrate surface result in surface roughness that leads to a change of adhesive strength at the interface between the

substrate and the coating layer. In order to evaluate the roughness of the steel surface in dependence on the strain levels and the strain path, the roughening on the Nakajima specimen's surfaces without coating layer was measured by means of the roughness measurement apparatus using the *MarSurf XR 20 V1.40-3* software packet.

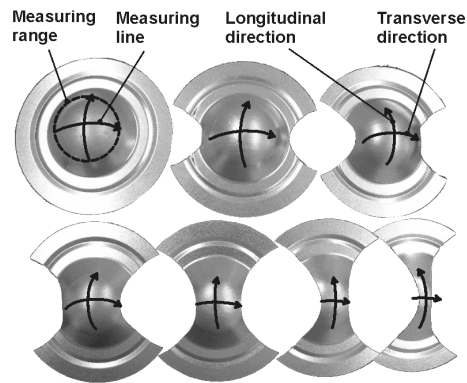


Fig. 4-13: Measurement of the roughness on steel substrate surface

The measurements were carried out in both longitudinal and transverse direction as shown in Fig. 4-13. The experimentally measured results of both steel substrates DX51 and DC04 are displayed in Fig. 4-14 and Fig. 4-15, respectively.

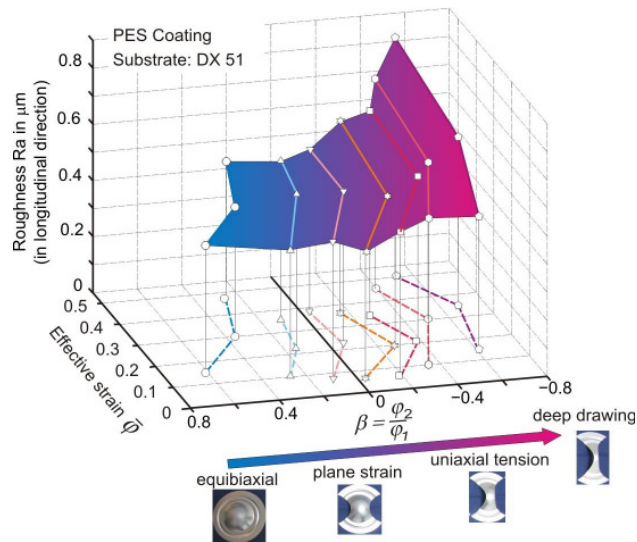


Fig. 4-14: Roughness of DX51 steel substrate in case of PES Coating

Like for the loss of gloss, the obtained results have shown that the surface roughening depends not only on the strain level but also on the strain state imposed on the specimens. Concretely, the increased strain caused an increase in the surface roughness. Both investigated materials indicated that the equibiaxial and plane strains result in a lower surface roughness compared to the one in case of simple tension and deep drawing mode.

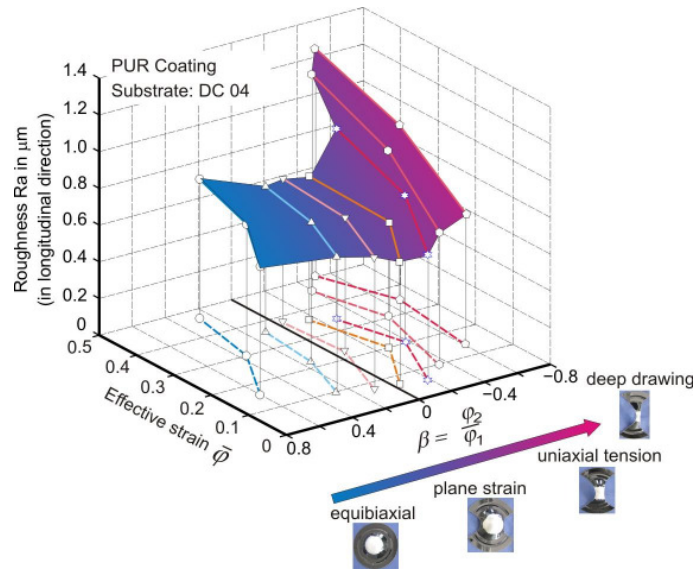


Fig. 4- 15: Roughness of DC04 steel substrate in case of PUR Coating

A comparison of the obtained roughnesses depicted in Fig. 4- 14 and Fig. 4- 15 clearly indicated that the substrate thickness certainly affects the roughness behaviors. As can be seen, the initial roughness of DX51 and DC04 is, in turn, 0.39 μm and 0.55 μm . At 30 % of the maximum pole height in the *Nakajima* test, the correspondent values in case of equibiaxial deformation, for instance, are 0.45 μm and 0.7 μm , respectively. The resulting deviations are 0.06 μm and 0.25 μm . At a higher strain level i.e. 90 % of the maximum pole height in the *Nakajima* test, the obtained deviations are 0.46 μm and 0.69 μm . Similar tendencies are observed in other deformation modes.

Above, the topography changes on the steel surface have been investigated. In order to evaluate the influence of that changes on the surface property of the coating layer, the roughness on the PES and PUR coating layers before and after forming are also measured and plotted as shown in Fig. 4- 16 and Fig. 4- 17.

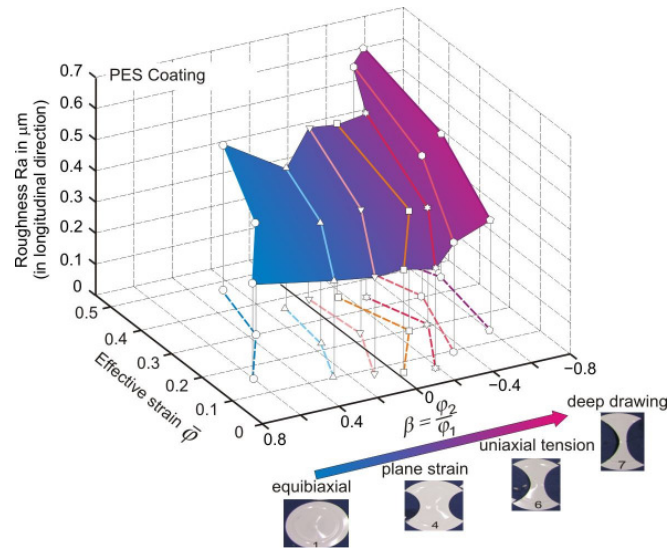


Fig. 4- 16: Roughness changes of PES coating after forming

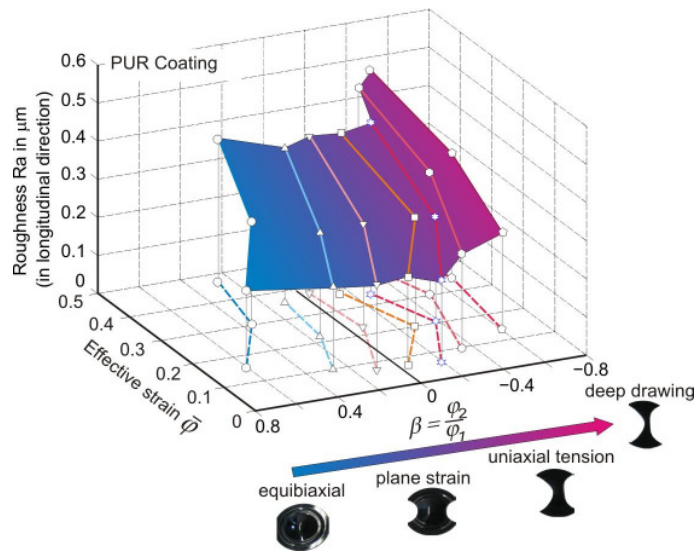


Fig. 4- 17: Roughness changes of PUR coating after forming

The obtained results show that the coating thickness causes the development of the roughness on the surface. In this investigation, the PES coating thickness is only 0.025 mm while the correspondent one of the PUR coating is 0.05 mm. The resulting roughness of the PES

coating is seen to be larger than the one of the PUR coating. At 30% of the maximum pole height in the *Nakajima* test, for instance, the roughness value of the PES reaches the value of 0.3 μm while the roughness of the PUR coating is only 0.2 μm . The similar tendencies are observed at higher strain levels and also in other deformation modes. Obviously, the roughnesses of the coating layer also depend on both the strain state and the imposed strains.

4.5 Correlation between gloss reduction, plastic strain and roughness

As investigated in the above section, the imposed plastic deformations induce topography changes in the steel substrate and the coating layer. The increase of the strain level leads to the surface roughness of both substrate and coating layer. The surface roughness results in a partial loss of adhesion of the coating layer, which may lead to coating failures such as delamination in further processing, *Schreurs et al. (2009)*. In addition to this, the surface roughness also contributes to the loss of gloss on the coating layer. Hence, the determination of the relationship between the gloss reduction, the surface roughness and the imposed deformations occurring on the deformed specimen is important.

In Fig. 4-18 and Fig. 4-19, the correlation between these parameters of both investigated materials is presented. The gloss reductions of four representative deformation modes i.e. the equibiaxial stretch, plane strain, uniaxial tension and deep drawing are taken into consideration.

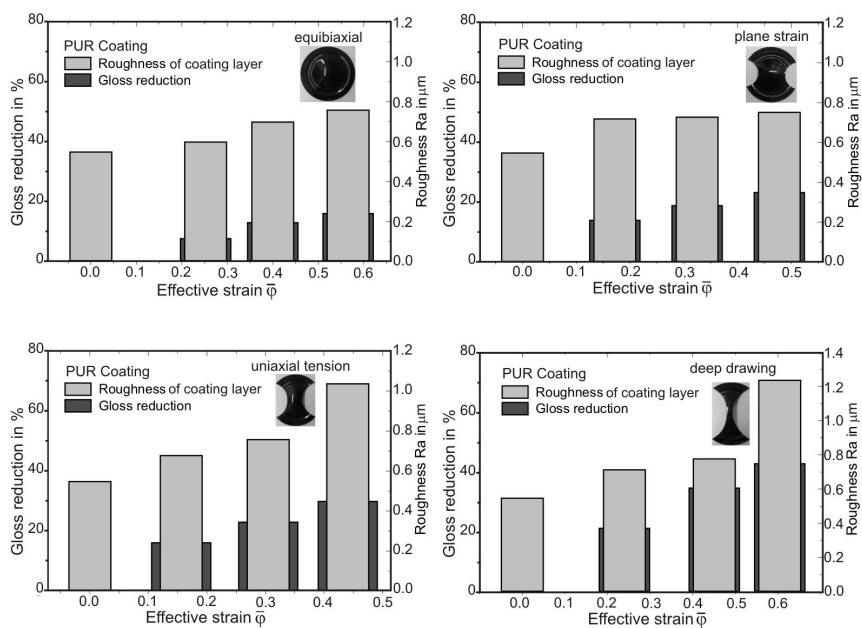


Fig. 4- 18: Correlation between gloss reduction, surface roughness and effective strain in case of PUR coating

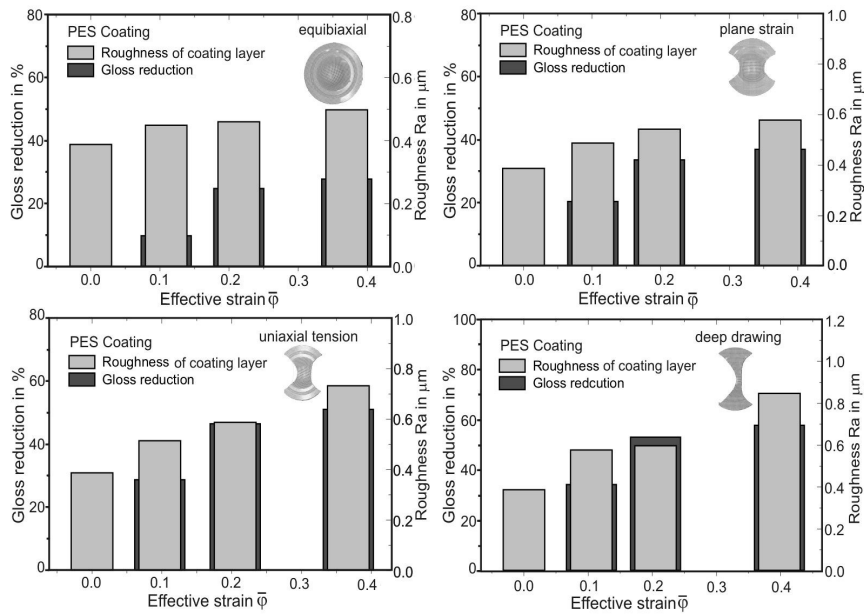


Fig. 4-19: Correlation between gloss reduction, surface roughness and effective strain in case of PES coating

For both investigated coated materials, the equibiaxial deformation modes result in a low value of the surface roughness and gloss reduction. In contrast to that, the deep drawing modes lead to a considerably higher roughness effect and also loss of gloss at a similar effective strain. The obtained results have also shown that the roughness and the resulting gloss reduction at a similar strain are significantly increased with increasing effective strain.

4.6 Evaluation of the obtained results by means of practice-oriented test

As investigated in the previous section, it has to be noted that the coating performance of the OCSM products does not only depend on the strain state and the strain magnitude but also on the thickness of the steel substrate and the coating layer. The *Nakajima test* used provides results on both sides of the FLD, and further induces all deformation modes in sheet metal forming. Therefore, the relations between optical property and plastic deformation obtained by the *Nakajima test* can be used as reference data in order to assess the change of the surface quality after the forming process. In this section, the change of the coating performance of the OCSM products is investigated by means of a practice-oriented test in order to evaluate and to prove the obtained relationships.

In order to tackle this idea, the deep drawing processes using PUR and PES coated materials are experimentally conducted. The strain distribution over the forming part was measured by means of the optical measurement system *Argus* by *GOM*. The gloss reduction was defined by the *NOVO – CURVE* gloss meter. The evaluated procedure is illustrated in Fig. 4-20.

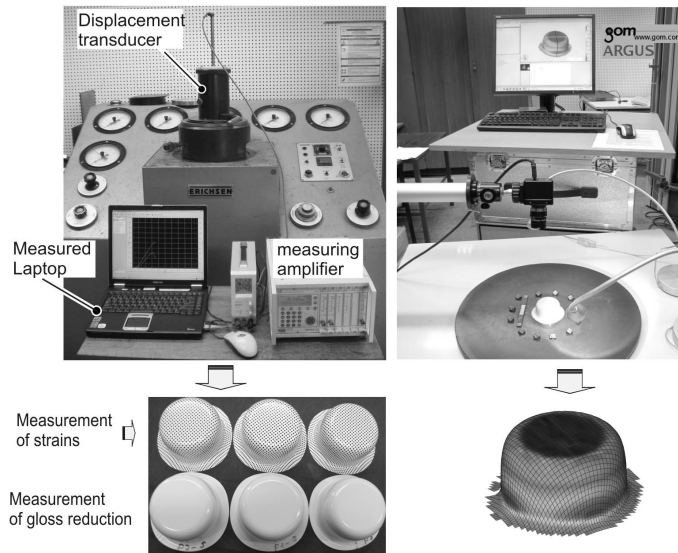


Fig. 4-20: Procedure to evaluate the gloss reduction in deep drawing process

In Fig. 4-21, the topographical performance of the PUR coated cup depending on the strain distribution in the deep drawing process is illustrated.

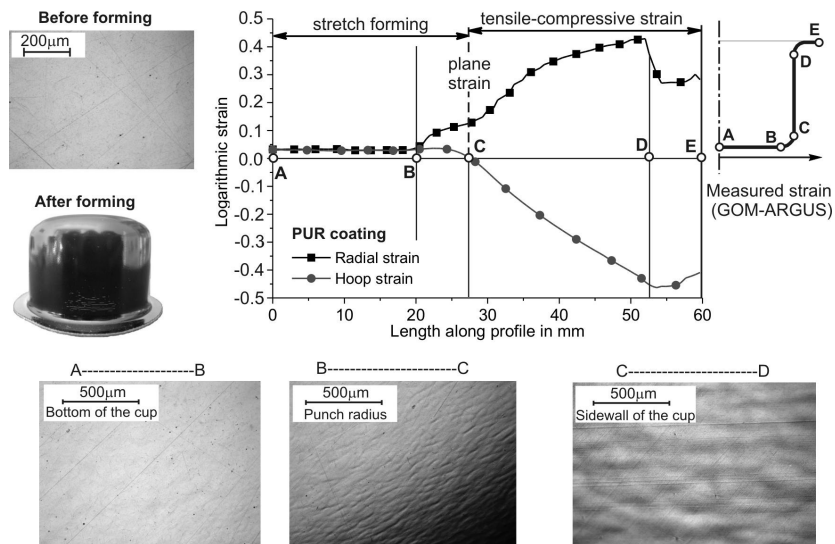


Fig. 4-21: Topographical performance of the PUR coated cup

It is seen that the deformation of the cup deep drawing induces topographical changes in both the substrate and, especially, the coating layer. This phenomenon leads to the gloss reduction of the coating. At the bottom area of the part, where the stretch forming occurred, the coating surface becomes rougher than the initial one. The coating performance change in this area is not large on account of a small imposed strain. Around the punch radius, where the higher deformation is observed, the coating performance was considerably changed. A small waviness on the coating is observed. At the cup wall, where the tensile – compressive strain occurred, the waviness effect became larger compared to the one at the punch radius.

Similar observations were made with the PES coated steel as shown in Fig. 4-22. The PES coating appearance is different from the one in the case of the PUR coating. It is observed that the bottom of the PES cup showed the flow-line effect on account of the strain aging effect of the DX51 substrate, which leads to this effect in case of stretch forming.

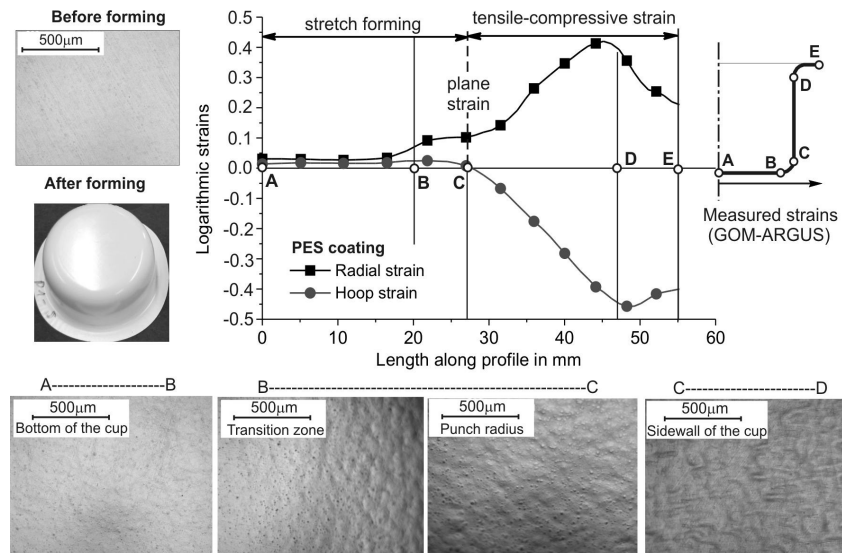


Fig. 4-22: Topographical performance of the PES coated cup

The flow-line effect does not continuously exist when the deformation is increased. Around the punch radius, the coating appearance is significantly changed compared to the correspondent area in the case of the PUR coating. At the sidewall area, where the highest deformation occurs, the type of the wave is also different compared to the PUR coating layer. No damage such as cracking or debonding is observed on the PES coating. Clearly, all the observations show that the topological performance of the coating is considerably affected by the coated material and the level of deformation.

As investigated above, the topographical changes induce the change of the optical property i.e. gloss reduction. Now, the glosses on correspondent areas are measured to show the

dependence of the gloss value on the strain state and the strain level. In Fig. 4-23, the gloss value as well as gloss reduction as a function of the strain of the PUR coated cup are shown. Before forming, the initial gloss value of the PUR coated sheet metal was 91.5 GU. After forming, the bottom area of the cup exhibited the highest gloss with 87.5 GU, as compared to other areas. From the corner around the punch radius to the corner around the die radius, the gloss value decreases gradually. The minimum gloss occurred at the sidewall of the cup and was only 37.7 GU. At the flange area, where shown the tensile-compressive strain state, the gloss value was lower than the one at the bottom of the cup and reached a value of 80.5 GU.

Apart from the gloss values, the gloss reduction along the profile of the deep drawing cup is also presented in Fig. 4-23. It can be seen that the lowest gloss reduction occurred at the bottom of the cup, where the stretch forming state was observed. As can be seen, this value was only 4.8% compared to the initial gloss value. From this position, the gloss reduction trend is continuously increased and reaches the maximum value at the sidewall area of the cup. The highest value of the gloss reduction was approximately 60%. In the flange area, the gloss reduction was not large and reached a value of 2.8%.

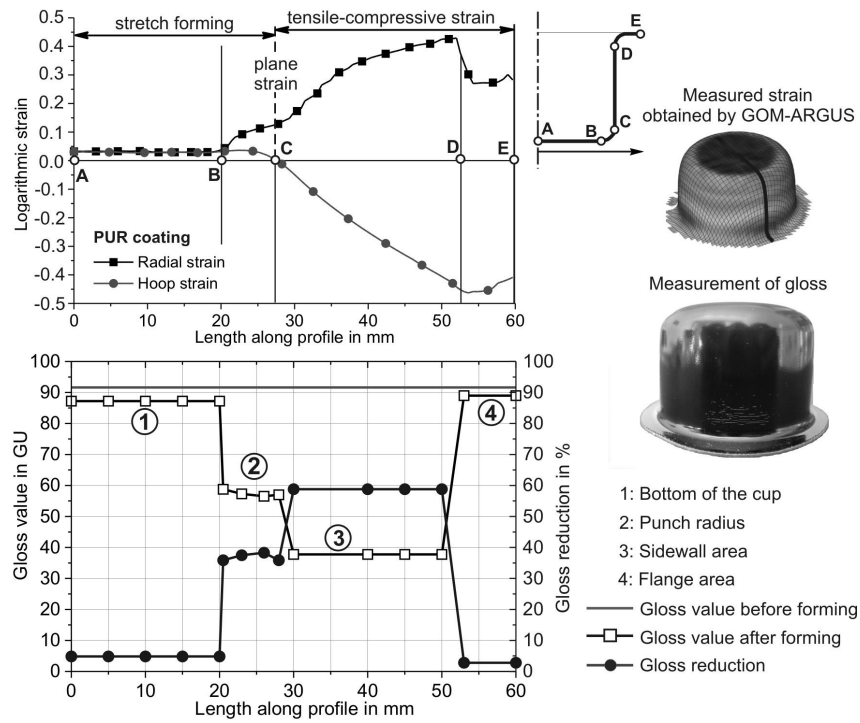


Fig. 4-23: Relationship of gloss reduction to deformation of the PUR coated cup

For the PES coated cup, a similar tendency of the gloss value and the gloss reduction was obtained as shown in Fig. 4-24. But the gloss reduction at the bottom and at the flange of the PES cup is above 10 %, while this value is around 2.8 % on the PUR cup. The gloss reduction of the PES cup is higher than that of the PUR cup on account of the thinner coating layer and steel substrate.

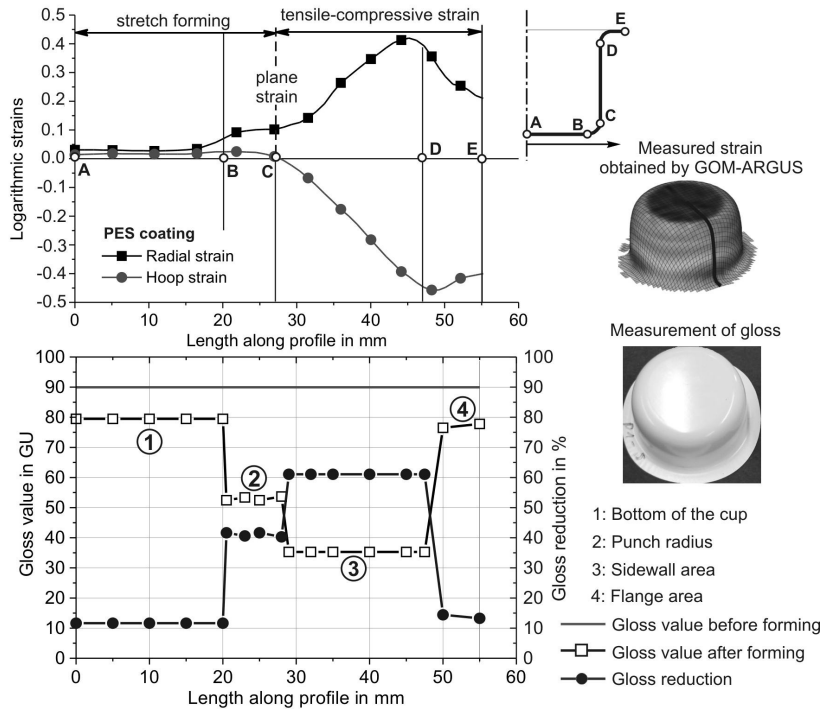


Fig. 4-24: Relationship of gloss reduction to deformation of the PES coated cup

Clearly, the experimentally determined results are in good agreement with the reference results obtained by the *Nakajima test*. It is confirmed that the gloss value and the correspondent gloss reduction are considerably dependent on the strain states and the strain level. The gloss degree decreases with increasing deformation. The gloss reduction is also affected by the strain states. The biaxial stretch deformation mode provides a lower gloss reduction compared to the deep drawing mode. The type and the thickness of the coated material and steel substrate have a considerable influence on the change of the coating appearance.

4.7 Gloss recovery effect

As mentioned above, OCSM is an ideal material for large-lot production in the appliance industry, architecture, civil engineering and automobile industry due to the advantages of the

mechanical-technological properties. For the application in the automobile industry, this kind of material is suitable for the manufacturing of car body panels and headlamp systems such as reflector parts. However, it has to be noted that the working temperature of the reflector parts is relatively high. This may consequently influence the gloss property of the OCSM reflector. Hence, the investigation of the influence of the temperature on the optical properties of the organic coated material is necessary.

To this end, *Nakajima tests* with pre-defined deformation levels were conducted. The resulting degree of gloss before thermal treatment was measured. Afterward, all specimens were placed into an oven. The setting temperature was 120°C and the working time approximately 30 minutes. The resulting gloss levels after thermal treatment were recorded. The loss of gloss in dependence on strain levels is computed by the equation (4.2).

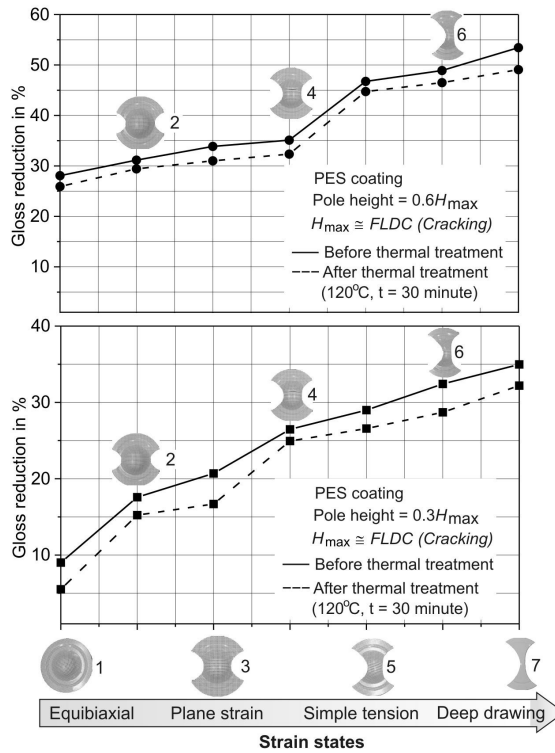


Fig. 4-25: Gloss recovery effect observed for PES coating

In Fig. 4-25 and Fig. 4-26, the resulting gloss reduction in case of PES and PUR coatings are displayed, respectively. It can be seen that the gloss reductions of both investigated materials after an additional thermal treatment were significantly lower than those before thermal treatment. Considering the gloss reduction at 30 % of the maximum pole height in the *Nakajima test* in the case of the PES coating, for example, the minimal and maximal value are

10 % and 35 %, respectively. After thermal treatment, the correspondent values are in turn 6% and 32 %.

For the PUR coated sheet, the similar tendencies of the gloss reduction after low thermal treatment were observed in the first and second series of the Nakajima test that corresponds to 30 % and 60 % of the maximum pole height in the *Nakajima* test. At a higher deformation level i.e. 90% of the maximum pole height in the *Nakajima* test, the additional thermal treatment leads to the cracking phenomenon on the coating layer of the forming part. The reason is the low thermal resistance of the PUR coated metal.

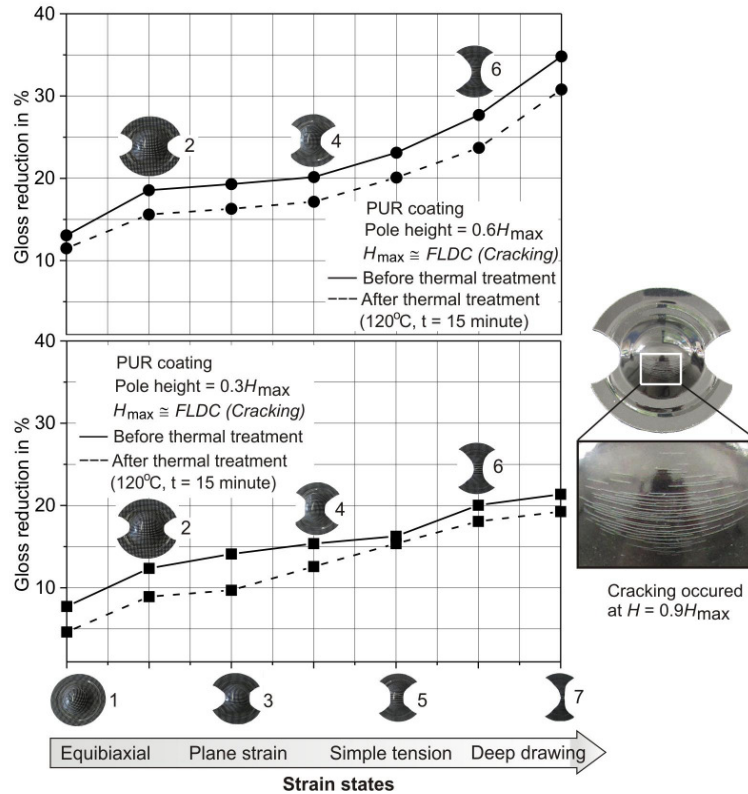


Fig. 4-26: Gloss recovery effect observed for PUR coating

This reversible gloss reduction is called “gloss recovery effect” and can be explained on the basis of the “Teil-Reflow effect” of plastically deformed polymer coatings. Accordingly, the coating defect can be repaired by providing a tighter molecular network that is flexible between the points of intersection, *Zwaag (2007)*. If the temperature exceeds the coating’s glass transition temperature (approximately 60°C for PUR and PES), the coating defect will

be recovered leading to a gloss recovery as observed. In Fig. 4- 27, the mechanism of this effect is schematically shown.

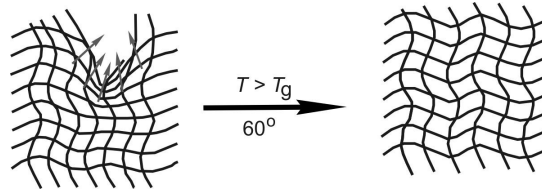


Fig. 4- 27: Reflow effect of polymer coating (T_g : glass transition temperature), Zwaag (2007)

Obviously, it can be concluded that the gloss reductions are affected by low additional thermal treatment. However, the reversible level is not high. Both obtained results for PUR and PES coatings give an indication of no considerable dependence of the gloss recovery on the effective strain and the strain state contributed in the specimens of the Nakajima test.

4.8 Conclusion

The above investigations indicated that the gloss reduction of the coated surface depends on the strain states and the deformation imposed on both the steel substrate and the coating layer. The relations between the gloss reduction and the plastic deformation obtained by the *Nakajima* test can be used as the reference data to predict the change of the optical property of OCSM products after industrial forming processes. According to the proposed method, it is necessary to establish gloss reduction curves versus different strain values. Then, based on these template curves, we can evaluate the gloss reduction which corresponds to a specific strain level and strain state. The following conclusions are drawn:

- The FLDC should be used instead of the FLD in order to evaluate the formability concerning the quality of the coating layer.
- An increase of the strain value leads to an increase of the loss of gloss.
- The strain state has a major influence on the gloss reduction and the roughness evolution. Among different strain states, the biaxial stretch deformation modes lead to a lower gloss reduction and roughness than the uniaxial and deep drawing modes. The uniaxial tension mode results in a higher gloss reduction and roughness than the tensile-compression mode.
- The gloss reduction is affected by topographical changes of both the substrate and the coating layer surface.
- The change of the optical performance depends on the thickness of both substrate and coating layer. A lower gloss reduction is attained if substrate and/or coating layer is thicker.

5 Simulation of the forming process with OCSM

In this chapter, the application of the simulation strategy to compute the forming process of OCSM is presented. The FE modeling such as material model, meshing of OCSM is first considered. The effectiveness and the feasibilities of the overall strategy are then verified by an axisymmetrical and a three-dimensional analysis. The simulation results are validated by experimental investigation afterward. The predicted procedure of the gloss reduction and the coating failures i.e. cracking based on FE and experimental results are also presented in this chapter.

5.1 Modeling

5.1.1 FE model

As per reviewed literature and the experimental investigation in the chapter above, the organic coated materials and steel substrates greatly differ in their mechanical behavior, especially when these materials are in the large deformation state. The organic coated materials such as PUR or PES show a nonlinear elastic behavior while the steel substrate exhibits an elasto-plastic behavior, Fig. 5- 1. Additionally, the elasticity modulus of the metal substrate is much higher than the one of the organic material, whereas the Poisson's ratio is smaller than that of the organic coated material. The difference of the Poisson's ratio leads to the difference of the thickness strain of both materials. Therefore, the prediction of the coating performances based on the deformation of the steel substrate only provides in-situ accuracy.

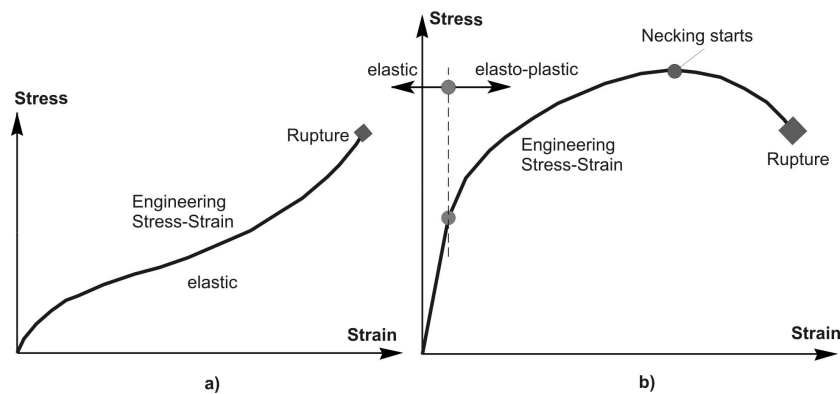


Fig. 5- 1: Strain-stress curve of the organic coated material (a) and the steel substrate (b)

From a structural point of view, it has to be noted that there is a cohesive zone at the interface between the steel substrate and the coating layer. Thus, the problem in consideration is whether the FE model has to consist of the cohesive zone or not. In order to answer this critical question, the failure modes and the failure mechanism of the coating layer on the steel substrate are analyzed. During forming process, mechanical stresses imposed on the coating layer and large plastic strains in the metal substrate lead to coating failures, Fig. 5-2. Among the induced failures, in-plane stresses are the causes of roughening or cracking. Meanwhile, out-plane stresses and plastic strains imposed on the steel substrate are the reasons for the loss

of adhesion between two layers. As a result, this may lead to delamination or surface roughness of the coating, *Hult et al. (1999)*. Obviously, the delamination is the macro fracture level of the layer material regarding the interface defect. The cohesive zone must only be considered for the computation of the delamination phenomenon between the layers.

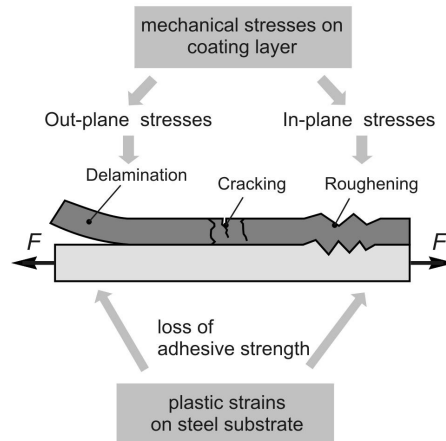


Fig. 5-2: Failure mechanism of the coating layer on the steel substrate

During the deep drawing process, for example, the loading condition i.e. occurring stresses according to by *Doege & Behrens (2007)* are shown in Fig. 5-3.

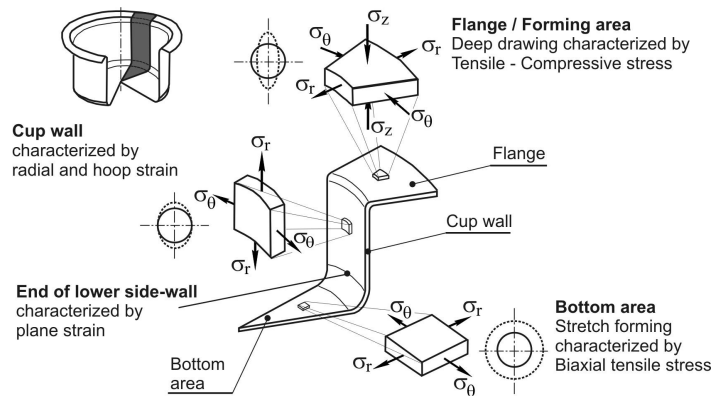


Fig. 5-3: Loading in deep drawing process, *Doege & Behrens (2007)*

According to this, the deep drawing process is characterized by the following zones:

- **Flange area:** metal at the flange area is bent and straightened as well as subjected to a **tensile - compressive stress**

- *Cup wall*: metal in the cup wall is subjected to a *circumference* or *hoop* and a *radial tensile strain*
- *End of lower cup wall*: *plane strain* (restrain uniaxial tensile stress)
- *Bottom area/Force transmission zone*: metal in this area is thinned down and is subjected to a *stretch forming* characterized by *biaxial tensile stresses*.

The imposed stresses on both the coating layer and the steel substrate are in-plane stress, except the flange area. The out-plane stress σ_z in this area characterized as compressive stress is caused by the BHF. The σ_z is equal to zero in case of an absence of the BHF. Clearly, this term cannot lead to the delamination effect during the forming process.

The obtained FLDC in chapter four and the conducted experimentations have shown that the roughening and cracking occurs on the coating layer before necking and delamination are observed on the steel substrate. The change of the optical property, i.e. gloss reduction is affected by surface roughening of both the steel substrate and the coating layer. This is not related to the interface defect. Therefore, the cohesive zone can be neglected in the case of the evaluation of the optical property of the coating layer.

Based on above analysis, it can be concluded that the coating layer should be considered in the FE model in order to predict directly the optical property changes of the coating layer. For this purpose, perfect adhesion on the interface between the steel substrate and the coating layer is assumed.

5.1.2 Elements used and meshing

It has to be noted that the element used for the coating layer is not similar to the element of the steel substrate. The reason is that the organic coated material shows a nearly incompressible behavior (the bulk modulus is much larger than the shear modulus or Poisson's ratio, approximately 0.499 or 0.5), and the solution cannot be obtained in terms of the displacement history only, since a purely hydrostatic pressure must be added without changing the displacements.

In this case, the low-order solid elements are proposed to model both materials. These elements are preferred in nonlinear structural mechanics because of their low computational cost and simplicity in dealing with this geometry. But in many cases, especially in case of pure bending problems, the brick element exhibits low-precision results due to the stiffening effects known as shear locking, Poisson thickness locking and volumetric locking. To prevent these locking effects and to obtain the accuracy of computations, at least two layers of element through the thickness of each material and RI technique are accompanied, *Chandra & Prathap (1989); Hauptmann et al. (2001)*. Additionally, for the modeling of the coating layer, either Herrmann formulation elements in *Marc/Mentat* or Hybrid formulation elements in *Abaqus* is used in order to prevent volumetric and shear locking. These elements are designed for incompressible elasticity applications. Apart from four nodes (at corners) as a standard element, the fifth node (at center) only has a pressure degree of freedom that is not to be shared with other elements, Fig. 5-4, *Abaqus (2007); Marc (2005)*. More precisely, they are "mixed formulation" elements, using a mixture of displacement and stress variables with an augmented variation principle to approximate the equilibrium equation and compatibility

conditions. These elements also remedy the problem of the volumetric locking and shear locking by using a fully or selectively reduced integration.

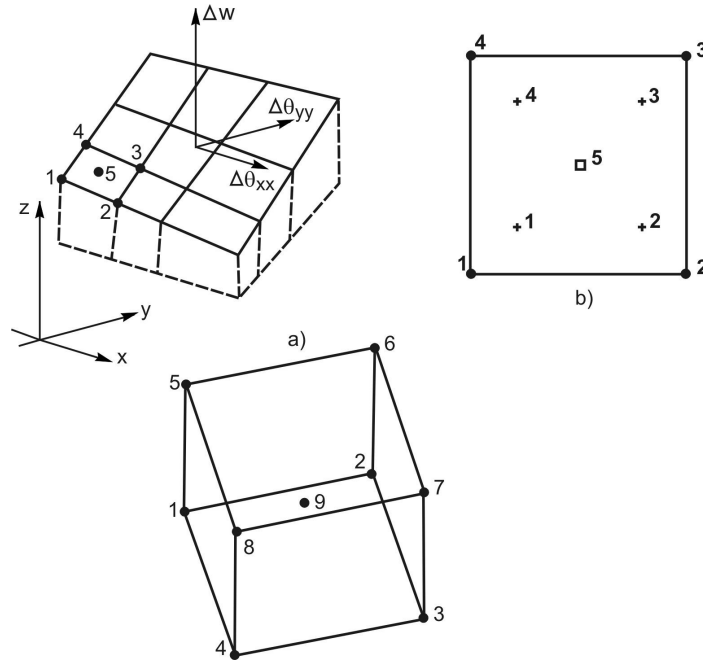


Fig. 5-4: Element with Herrmann formulation (a), Gaussian integration points (b), Marc (2005)

In a 2D model, four-node standard plane strain elements can be applicable because these elements are free from the volumetric locking effect *Chandra & Prathap (1998)*. But in a 3D model, the eight-node standard elements suffer from the volumetric locking effect. Therefore, three-dimensional arbitrarily distorted brick elements used Herrmann formulation (in Marc) or Hybrid-formulation (in Abaqus) is employed for the modeling of the coating layer, Fig. 5-4. This formulation uses an eight-node isoparametric element with an additional ninth node for hydrostatic pressure. This element is suitable for the simulation including materials, which show an incompressible behavior such as plastic or polymer.

The number of FE elements over the thickness of both materials plays an important role in FE simulation and it has a considerable influence the accuracy of the FE result. Therefore, convergent tests need to be carried out in order to determine the suitable number of elements that can provide the precise result. To check the convergence of the FE computation, the circular cup deep drawing process is simulated. In this simulation, the FE mesh is varied from coarse to fine until the results are convergent. The FE model is depicted in Fig. 5- 5.

Fig. 5-6 shows the result of the convergent test. Clearly, the equivalent plastic strain changes with increasing element number. According to this test, at least four sub-layers of elements

should be adopted over the substrate and the coating thickness in order to get convergent results.

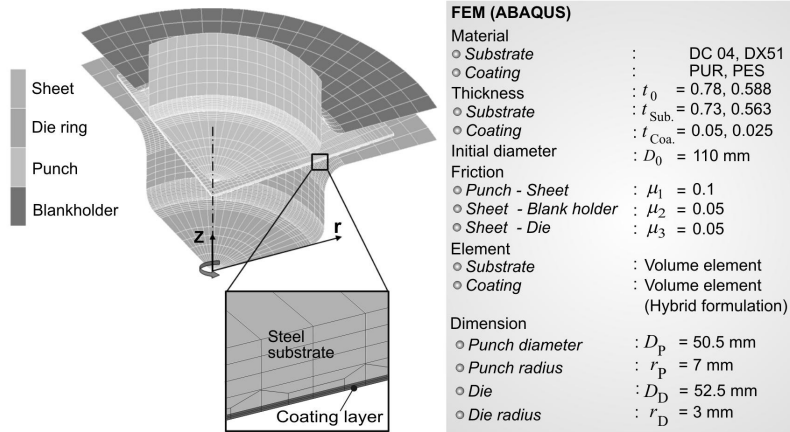


Fig. 5- 5: FE model for convergent test

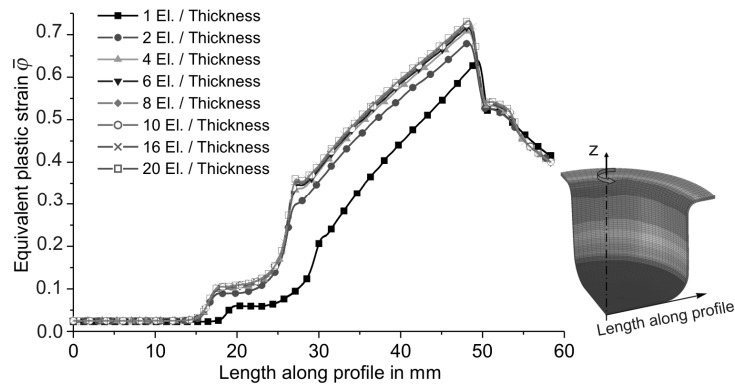


Fig. 5-6: Equivalent plastic strain depending on the number of elements

From the structural point of view, the coating thickness is quite thin as compared to the substrate thickness. The thickness ratio with respect to the substrate often ranges from 1:2.5 and 1:50. Therefore, the mesh size for the coating layer must be very fine in comparison to that of the steel substrate. As a result, both total number of elements and computational time will be significantly increased. To overcome this challenge, it is necessary to find out a suitable mesh strategy. In Fig. 5- 7, the meshed strategy for the modeling of OCSM is proposed. Basically, both types of the mesh can be used. But it has to be noted that the “simple mesh” (SM) leads to a bad aspect ratio when the coating layer is modeled. In order to reduce the aspect ratio, the mesh type b (RAR) is proposed.

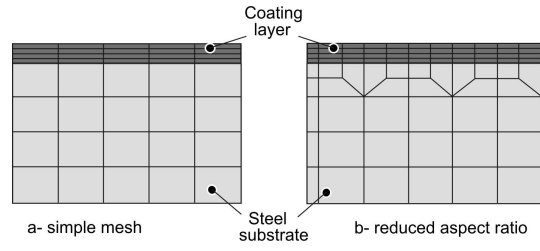


Fig. 5- 7: Meshing of OCSM

5.2 Material modeling for the coating layer

5.2.1 Energy function

Organic coated materials show a nonlinear elastic strain-stress behavior. For the modeling of such materials, two theoretical models, so called hyperelastic and viscoelastic models are commonly employed. The hyperelastic models were first documented by *Treloar (1958)* and applied to polymers that are considered to have isotropic, highly elastic and incompressible properties. The major distinctions of the hyperelastic and the viscoelastic models are summarized as follows, *Dong (2002)*:

1. Due to the non-linear elastic behaviors, hyperelastic models rely solely on the final strain state and not on the history of strain
2. Considerations of both elastic and viscous effects, viscoelastic models nonetheless are time-dependent deformation

Undergoing large deformations, most of the polymer materials show nearly incompressible characteristics. This indicates that the volume of workpieces during deformation remains constant despite thickness, length and width are varied. The incompressible condition is described as follows:

$$V = V_0 \quad (5.1)$$

or

$$\lambda_1 \lambda_2 \lambda_3 = 1 \quad (5.2)$$

where:

- V and V_0 are volumes in the deformed and un-deformed states;
- $\lambda_1, \lambda_2, \lambda_3$ are the principal stretch ratio in 1, 2, 3 directions and can be defined as:

$$\lambda_i = \frac{L_i}{L_{i,0}} = \frac{L_i + \Delta u_i}{L_0} = 1 + \varepsilon_{i,E} \quad i = 1, 2, 3 \quad (5.3)$$

where $\varepsilon_{i,E}$ is the engineering strain in the i direction.

The three strain invariants of the right Cauchy-Green strain tensor \mathbf{C} can be expressed as:

$$\begin{aligned} I_1 &= \lambda_1^2 + \lambda_2^2 + \lambda_3^2 \\ I_2 &= \lambda_1^2 \lambda_2^2 + \lambda_2^2 \lambda_3^2 + \lambda_3^2 \lambda_1^2 \\ I_3 &= \lambda_1^2 \lambda_2^2 \lambda_3^2 \end{aligned} \quad (5.4)$$

If the material shows a perfectly incompressible behavior, $I_3 = 1$.

For the hyperelastic materials, the strain energy function W was employed. The postulation is that the corresponding stress components are obtained by taking the derivative of W with respect to the strain components. The available function of strain energy is represented either in term of the strain invariants that are functions of the stretch ratios, or directly in terms of the stretch ratios themselves. The general form of the strain energy function can be evidently described by the sum of a series of terms involving powers of $(I_1 - 3)$ and $(I_2 - 3)$ in the equation (5.5), *Marc (2005)*:

$$W = \sum_{i,j}^{M,N} C_{ij} (I_1 - 3)^i (I_2 - 3)^j \quad (5.5)$$

where

- W : energy function;
- C_{ij} : material parameters concerning the Shore hardness.

When the body is undeformed, it can be acquired of $W = 0$ and $C_{ij} = 0$. From the general equation (5.5), a variety of hyperelastic models have been developed.

Based on the energy function, the stresses can be computed by taking derivatives of W with respect to strain components and it can be written as follows:

$$\mathbf{S} = \frac{\partial W}{\partial \mathbf{E}} = \sum_i \frac{\partial W}{\partial \lambda_i} \frac{\partial \lambda_i}{\partial \mathbf{E}} \quad (5.6)$$

where \mathbf{E} is the Green-Lagrange strain tensor; \mathbf{S} is the second Piola-Kirchhoff stress tensor. It relates to the Cauchy stress by the following expression:

$$\mathbf{S} = \mathbf{J} \mathbf{F}^{-1} \cdot \boldsymbol{\sigma} \cdot \mathbf{F}^{-T} \quad (5.7)$$

with

- $J = V/V_0$: Jacobien;
- \mathbf{F} : deformation gradient which relates to the right Cauchy-Green strain tensor by the expression $\mathbf{C} = \mathbf{F}^T \mathbf{F}$.

The constitutive tensor is calculated as the second derivative of the energy function W with respect to the Green-Lagrange strain as:

$$\mathbf{C} = \frac{\partial^2 W}{\partial \mathbf{E}^2} = \frac{\partial}{\partial \mathbf{E}} \left(\sum_i \frac{\partial W}{\partial \lambda_i} \frac{\partial \lambda_i}{\partial \mathbf{E}} \right) \quad (5.8)$$

In general, the constitutive tensor of a hyperelastic material is a function of the strain λ_i . Hence, the strain- stress behavior is nonlinear even at small strains.

5.2.2 Categories of hyperelastic model

a. Neo-Hookean model

The earliest and simplest elastomer model is the neo-Hookean model that considered the behavior of rubber-like material, *Dong (2002)*. This model is expressed as:

$$W = C_{01}(I_1 - 3) \quad (5.9)$$

The constitutive relation for uniaxial tension i.e. $\lambda_1 = \lambda$, $\lambda_2 = \lambda_3 = \frac{1}{\lambda}$ can be computed as:

$$\sigma_{ur} = 2C_{10}\left(\lambda^2 - \frac{1}{\lambda}\right) \quad (5.10)$$

The constitutive relation for equibiaxial tension i.e. $\lambda_1 = \lambda_2 = \lambda$, $\lambda_3 = \frac{1}{\lambda^2}$ can be described as:

$$\sigma_{er} = 2C_{10}\left(\lambda^2 - \frac{1}{\lambda^4}\right) \quad (5.11)$$

This model exhibits a constant shear modulus and gives a good correlation with the experimental data of up to 40% of the elongation in the uniaxial tension test and of up to 90% of the elongation in the simple shear test, *Marc (2005)*.

b. Mooney-Rivlin model

The other forms of the energy function were propounded by *Mooney-Rivlin (1940)*, and *Rivlin et al. (1951)*. They are given as follows:

- Two-term Mooney-Rivlin model:

$$W = C_{10}(I_1 - 3) + C_{01}(I_2 - 3) \quad (5.12)$$

- Three-term Mooney-Rivlin model:

$$W = C_{10}(I_1 - 3) + C_{01}(I_2 - 3) + C_{11}(I_1 - 3)(I_2 - 3) \quad (5.13)$$

The constitutive relation for the uniaxial tension in this case becomes:

$$\sigma_{ur} = 2\left[\lambda^2 - \frac{1}{\lambda}\right]\left[\frac{\partial W}{\partial I_1} + \lambda^2 \frac{\partial W}{\partial I_2}\right] = 2C_{10}\left(\lambda^2 - \frac{1}{\lambda}\right) + 2C_{01}\left(\lambda - \frac{1}{\lambda^2}\right) \quad (5.14)$$

Similarly, the constitutive relation for the equibiaxial tension is computed as:

$$\sigma_{er} = 2\left[\lambda^2 - \frac{1}{\lambda}\right]\left[\frac{\partial W}{\partial I_1} + \lambda^2 \frac{\partial W}{\partial I_2}\right] = 2C_{10}\left(\lambda^2 - \frac{1}{\lambda^4}\right) + 2C_{01}\left(\lambda^4 - \frac{1}{\lambda^2}\right) \quad (5.15)$$

Mooney-Rivlin's strain energy function is widely used to solve the large elastic deformation of rubber-like materials. By setting $C_{10} = 0$, this function reduces to the neo-Hookean form. The Mooney-Rivlin model can be used in the range of up to 100% technical strain of elastomer material. Therefore, the Mooney-Rivlin model is often used to characterize the material behavior of elastomers, *Stojek et al. (1998)*.

c. Yeoh model

Yeoh proposed another model that only depends on the first strain invariant, which can be expressed as:

$$W = C_{10}(I_1 - 3) + C_{20}(I_1 - 3)^2 + C_{30}(I_1 - 3)^3 \quad (5.16)$$

This model is more versatile than the others since it has demonstrated to fit various modes of deformation using the data obtained from a uniaxial tension test. This leads to reduced requirements on material testing, *Marc (2005)*.

d. Ogden model

Alternatively, for the sake of mathematical simplicity, *Ogden (1972)* proposed another form of the energy function with respect to principal stretch ratios instead of the principal strain invariants. This form is given as:

$$W = \sum_{i=1}^n \frac{\beta_i}{\alpha_i} (\lambda^{\alpha_i} + \lambda^{\alpha_i} + \lambda^{\alpha_i} - 3) \quad (5.17)$$

where α_i and β_i are experimentally determined material parameters. These parameters can be non-integer and negative. The only restriction is that the value of the strain energy function in equation (5.17) must remain positive after total summation, *Stojek et al. (1998)*. For uniaxial tension, the constitutive relation becomes:

$$\sigma_{ur} = \lambda^2 T_{11} = \sum_{i=1}^r \beta_i \left[\lambda^{\alpha_i} - \lambda^{-\frac{\alpha_i}{2}} \right] \quad (5.18)$$

The constitutive relation for equibiaxial tension is given as follows:

$$\sigma_{er} = \lambda^2 T_{11} = \lambda^2 T_{22} = \sum_{i=1}^r \beta_i \left[\lambda^{\alpha_i} - \lambda^{-2\alpha_i} \right] \quad (5.19)$$

For ease of reference, the strain energy functions of hyperelastic models, their form and application range are summarized in Table 5- 1.

Table 5- 1: Strain energy function for elastomer material, *Dong (2002)*

Model	Energy function	Suitable material	Applied range
Neo-Hookean	$W = C_{01} (I_1 - 3)$	Nature rubber, elastomer	Small strain for uniaxial and equibiaxial tension of sheet
Mooney-Rivlin (2 parameters)	$W = C_{10} (I_1 - 3) + C_{01} (I_2 - 3)$	ABS, PMMA, elastomer	Large elastic strain for uniaxial, biaxial tension and simple shear
Mooney-Rivlin (3 parameters)	$W = C_{10} (I_1 - 3) + C_{01} (I_2 - 3) + C_{11} (I_1 - 3) (I_2 - 3)$	ABS, PMMA, elastomer	Large elastic strain for uniaxial, biaxial tension and simple shear
Yeoh	$W = C_{10} (I_1 - 3) + C_{20} (I_2 - 3)^2 + C_{30} (I_1 - 3)^3$	Carbon-black filled rubber	Large elastic strain
Ogden	$W = \sum_{i=1}^n \frac{\beta_i}{\alpha_i} (\lambda^{\alpha_i} + \lambda^{\alpha_i} + \lambda^{\alpha_i} - 3)$	ABS, PPO and PC-PBT alloy, HDPE	Uniaxial and biaxial tensions over the large strain range

5.2.3 Material data for organic coated material

In order to describe the material behavior of the PUR and PES coatings the Mooney- Rivlin model is employed because this model can meet the requirement of computational accuracy and already available in both FE codes *Abaqus* and *Marc/Mentat*, commercial software which are available at IUL.

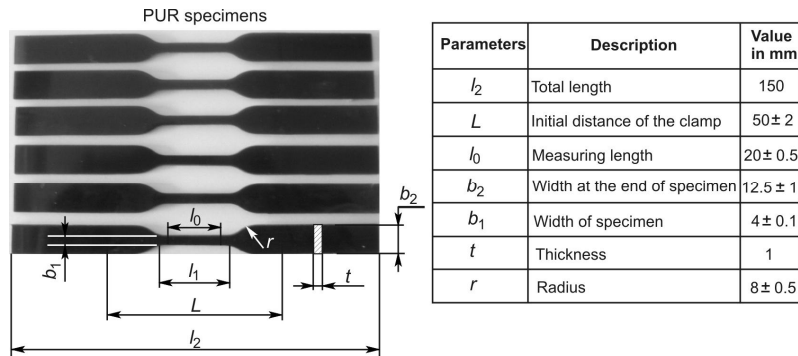


Fig. 5- 8: PUR-specimens for the determination of material properties

The material constants C_{01} and C_{10} in the model can be deduced from experiments such as the tensile or the compression tests by using curve-fitting procedures. To perform the tests with a PUR coating, the specimens were prepared by the company *Hawiflex GmbH* according to the standard *DIN EN ISO 527*, see Fig. 5- 8. The tests were conducted on a *Zwick/Roel* testing machine at *Kunststoff Institut Lüdenscheid*. The material parameters for the PES coated material were supported by *Voestalpine GmbH* in Austria. Fig. 5-9 presents the experimental results i.e. strain–stress curve obtained by the tensile tests of the PUR and the PES coating.

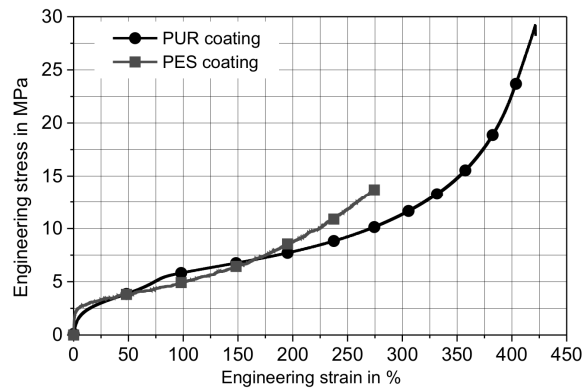


Fig. 5-9: Strain – stress curve of the PUR and the ductile PES coated material

The experiment results show that the form of the PUR and the PES curves are similar. The PES coating is harder than the PUR coating. At the same strain of $\varepsilon = 200\%$, the correspondent stress of the PUR is around 7.5 MPa. Meanwhile this value is 9.5 MPa with the PES coating. The ultimate strain of the PUR coating is also higher than the one of the PES coating. In detail, this value is 400% for the PUR and 250% for the PES, respectively. By using the curve-fitting procedure which is implemented in the commercial software package *Marc/Mentat*, the material constants of the Mooney-Rivlin model, i.e. C_{01} , C_{10} and C_{11} for the PES and the PUR coating are defined and given in Table 5-2 and Table 5-3, respectively.

Table 5-2: Material constants for Mooney-Rivlin model of the PUR coating

Material constants of PUR coating	C_{01} in N/mm ²	C_{10} in N/mm ²	C_{11} in N/mm ²
Mooney – Rivlin model with 2 parameters	0.022	5.033	
Mooney – Rivlin model with 3 parameters	0.021	4.130	-0.071

Table 5-3: Material constants for Mooney-Rivlin model of the PES coating

Material constants of PES coating	C_{01} in N/mm ²	C_{10} in N/mm ²	C_{11} in N/mm ²
Mooney – Rivlin model with 2 parameters	0.014	1.875	
Mooney – Rivlin model with 3 parameters	-0.003	2.112	3.773

5.3 Material model for steel substrate

The steel substrate of the PUR and the PES coated steel are DC04 and DX51 because of their excellent cold-formability. In order to determine the material properties, uniaxial tensile tests according to (*DIN-EN-100002*) were carried out as illustrated in Fig. 5-10.

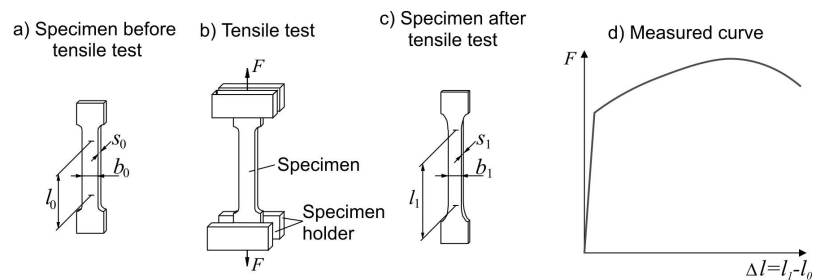


Fig. 5-10: Principle of uniaxial tensile test

The material behavior of the metal substrate can be divided into elastic and elastic-plastic parts. The elastic region is characterized by a nearly linear relation of strain-stress which is

described by Hook's law. The elastic-plastic region is described by the flow curve k_f that expresses the relation between yield stress and equivalent strain φ_e .

For strains that are outside of the identifiable area in the uniaxial tensile test ($\varphi_{max} \approx 0,2$), the flow curve is mathematically extrapolated. For this purpose, the following approaches e.g. either Swift or Voce will be utilized.

$$k_f = k(\varphi_0 + \varphi)^n \quad (5.20)$$

$$k_f = \sigma_0 + G(1 - e^{-C\varphi}) \quad (5.21)$$

where k , φ_0 , n , σ_0 , G and C are the material constants.

In this research, the plasticity criterion with a isotropic hardening effect is invoked due to its simplicity while satisfying the accuracy requirements of metal forming problems. The flow curve is extrapolated from the uniaxial tensile test on the basis of the power-law (Swift) equation. The flow curves and the hardening rule of the steel substrate with PES and PUR coatings are summarized in Fig. 5-11. The material data of both investigated steel substrates are summarized in Table 5- 4.

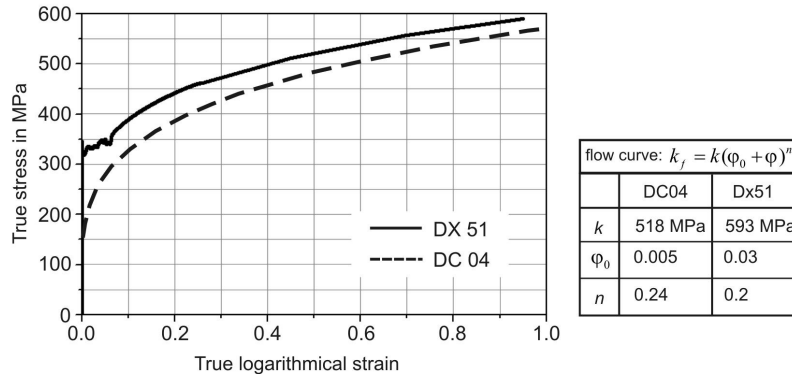


Fig. 5-11: Flow curve of the DC04 and the DX51

Table 5- 4: Material data of the DC04 and the DX51

Steel substrate	Young's mo. KN/mm ²	$R_{p0.2}$ N/mm ²	R_{eH} N/mm ²	R_{eL} N/mm ²	A_e %	R_m N/mm ²	A_g %	A %	r-value
DC04	183.50	174.11	—	—	—	308.13	26.85	41.76	1.6
Dx51	205.67	320	344	342	5	361	21	32	0.84

5.4 Simulation set-up and results

In this section, the potentiality and the feasibility of the proposed simulation strategy are verified by using the hydraulic bulge process, the circular cup and the square cup deep drawing process. All simulation results are validated by the correspondent experimentations.

The prediction of gloss reduction on the deep drawing cup, by using FE results in conjunction with experiments, is also discussed.

5.4.1 Simulation set-ups

In Fig. 5- 12, the FE models of the hydraulic bulge test, the circular cup and square cup deep drawing test are shown.

In the hydraulic bulge test, Fig. 5- 12a, the sheet metal is fixed between the die ring and the blank holder. The chamber underneath the sheet metal is filled with special oil. During the test, the sheet is clamped and then deformed frictionless by means of a drawing piston, which moves upward and presses the oil against the sheet metal. Due to symmetrical condition, a half of the 2D model of the forming tools and blank is modeled in order to reduce the total degrees of freedom and, therefore to speed up the computations. The oil pressure, which is created by the drawing punch, is modeled as a distributed load on the edge of the elements. Contact and friction is neglected because there is no relative motion between the sheet metal and the forming tools. Since the structure is axially symmetric, axisymmetric 2D standard elements are used to discretize the steel substrate because these elements are free from any volumetric locking effect. To model the coating layer, axisymmetric 2D elements using the Herrmann formulation are employed.

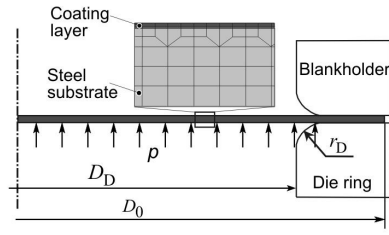
The FE model of the circular cup deep drawing test is depicted in Fig. 5- 12b. Due to the symmetrical characteristics, only a quarter of the structure needs to be modeled in order to reduce the computing time. According to *Meuthen & Jandel (2005)*, the friction coefficient between the organic coating and the steel tools is smaller than 0.05 if a highly volatile oil is used as a lubricant. The last investigations at the IUL, which were carried out by *Kleiner et al. (2002)* also proved that the friction coefficient of organic coated material is lower than 0.05. Therefore, the friction coefficient between the sheet and the die ring, denoted by μ_1 and μ_2 , were assumed to be 0.05. Since the punch is not lubricated in the experiment, so the friction between the punch and the blank, denoted by μ_3 , is much higher than μ_1 and μ_2 and assumed to be 0.1. In this case, the three-dimensional arbitrarily distorted brick elements used Herrmann formulation is employed for the modeling of the coating layer. For the steel substrate, the three-dimensional brick elements are used.

Obviously, a two-dimensional model is only useful to be applied for simple cases or primary design processes. Considering the fact that the three-dimensional complex geometry is indeed often seen in industry, the application of the developed simulation strategy for the three dimensional geometry is required.

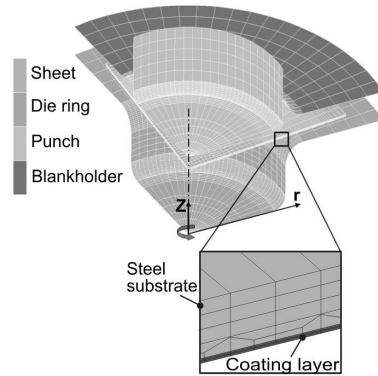
In Fig. 5- 12c, the FE model of the square cup deep drawing as a 3D demonstrated part is shown. Similar to the circular cup deep drawing process, the circular form of the initial blank is chosen. For this computation, all parameters of the axisymmetrical case, i.e. the material, the contact friction between the blank and the forming tools, the element types can be re-used. The punch in both cases, i.e. circular cup and square cup deep drawing simulation is pressed up against the sheet until the given displacement is reached.

a) Hydraulic bulge test

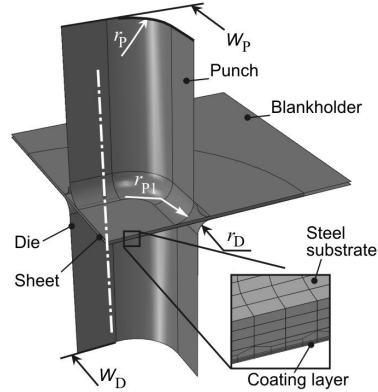
Initial diameter	: $D_0 = 180$ mm (PUR, PES)
Dimension	
◦ Die ring	: $D_D = 100$ mm
◦ Die radius	: $r_D = 3$ mm
Element	
◦ Substrate	: Volume
◦ Coating	: Volume (Hybrid formulation)



b) Circular cup deep drawing



c) Square cup deep drawing



FEM (ABAQUS)

Material		Friction	
◦ Substrate	: DC 04, DX51	◦ Punch - Sheet	: $\mu_1 = 0.1$
◦ Coating	: PUR, PES	◦ Sheet - BH	: $\mu_2 = 0.05$
Thickness		◦ Sheet - Die	: $\mu_3 = 0.05$
◦ Substrate	: $t_{Sub.} = 0.73$ mm, 0.563mm	Element	
◦ Coating	: $t_{Coa.} = 0.05$ mm, 0.025mm	◦ Substrate	: Volume
		◦ Coating	: Volume (Hybrid formulation)
Initial diameter	: $D_0 = 110$ mm (PUR, PES)	Initial diameter	: $D_0 = 100$ (PUR), 95mm (PES)
Dimension		Dimension	
◦ Punch diameter	: $D_P = 50.5$ mm	◦ Punch width	: $W_P = 40$ mm
◦ Punch radius	: $r_P = 7$ mm	◦ Punch radius	: $r_P = 10$ mm, $r_{P1} = 4.5$ mm
◦ Die	: $D_D = 52.5$ mm	◦ Die width	: $W_D = 52.5$ mm
◦ Die radius	: $r_D = 3$ mm	◦ Die radius	: $r_D = 3$ mm

Fig. 5- 12: FE model of hydraulic bulge test (a), deep drawing process (b), (c)

For simplicity and efficiency, in all FE models, forming tools such as the punch, the blank holder and the die ring have all been idealized as rigid bodies, while the organic coated sheet is modeled as a deformable part. The material parameters for the coating layer and the steel substrate are described in Table 5-2, Table 5-3, Table 5-4, and Fig. 5-11. The computations were carried out by using the commercial software package *Abaqus 6.7*.

5.4.2 Simulation results and validations

5.4.2.1. Hydraulic-bulge test

In order to validate the simulation results of the hydraulic-bulge test, the correspondent experiments using the PUR and the PES coated sheet metal were conducted at room temperature by using an *Erichsen* universal testing machine. After performing the tests, the optical measurement system *Argus* offered by the company *GOM* was utilized to measure the deformation of the deformed parts.

The circular specimens with a diameter of 180 mm were cut from the PUR and PES coated sheet metal. Before testing, all specimens were printed with a circle-grid pattern on both sides in order to measure the strain distributions on the coating layer and the steel substrate. The diameter of the circular grid is 1 mm and the distance between them is 2 mm. A professional screen-printing method was used to print the grid pattern on the decorative coating layer in order to avoid mechanical failures like scratches during the printing process. On the black PUR coating layer, the white grid patterns were printed. In contrast to that, the black circle-grid was employed on the white PES coating layer. In order to increase the reliability of the results, five specimens were used over each material. The procedure for the validation of the FE results is depicted in Fig. 5-13.

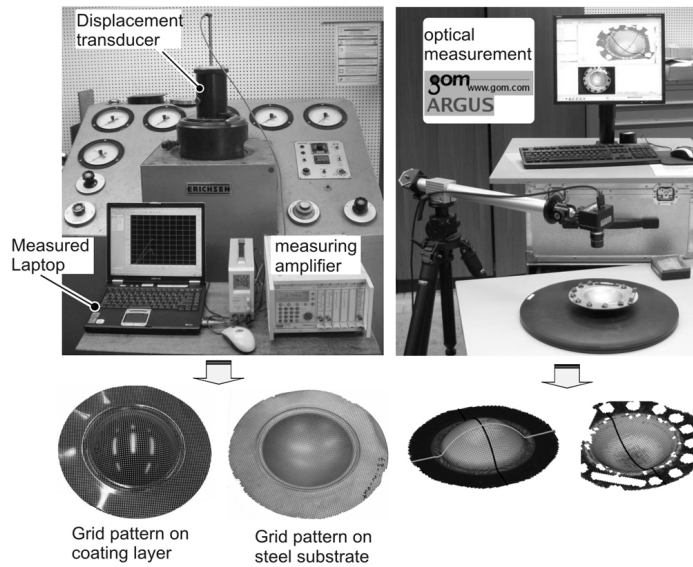


Fig. 5-13: Procedure for validation of FE results

As comparative parameters, the radial strain, the hoop strain and the thickness reduction on the steel substrate and the coating layer are taken into consideration. These parameters are compared to the experiment in order to evaluate the accuracy and the robustness of the

proposed simulation strategy. The comparison of the simulation with experimental results in the case of the PUR coating is depicted in Fig. 5-14.

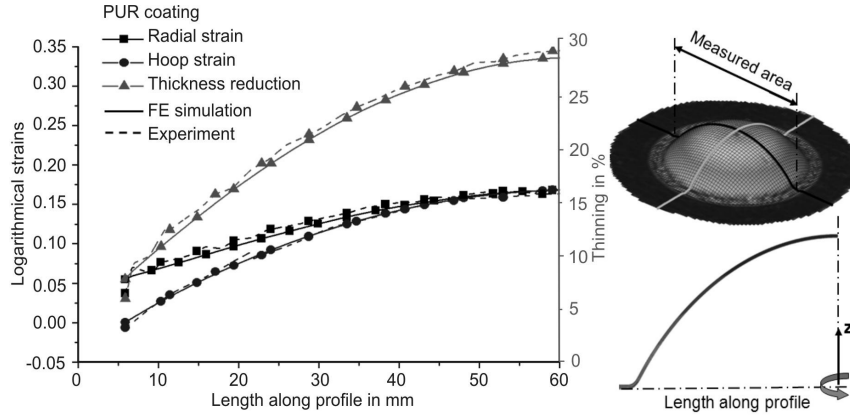


Fig. 5-14: Comparison of strains on the coating layer in hydraulic bulge test - PUR coating

The measured area is located at the draw-bead where the sheet is clamped during the forming process. Only one half of the measured strain is displayed due to the symmetrical property. For the strain components, i.e. the radial and the hoop strains, there is no significant difference between the two results. Concerning thinning, it is observed that the predicted thickness reduction is the same as in the experimental one. The thickness reduction varies along the part wall. The maximal thinning occurs at the top of the part and reaches the value of approximately 30 %. The deviation between the numerical and experimental thickness is lower than 3 %.

For the case of the PES coating, the comparisons between the numerical and experimental results are shown in Fig. 5-15 and Fig. 5-16, respectively.

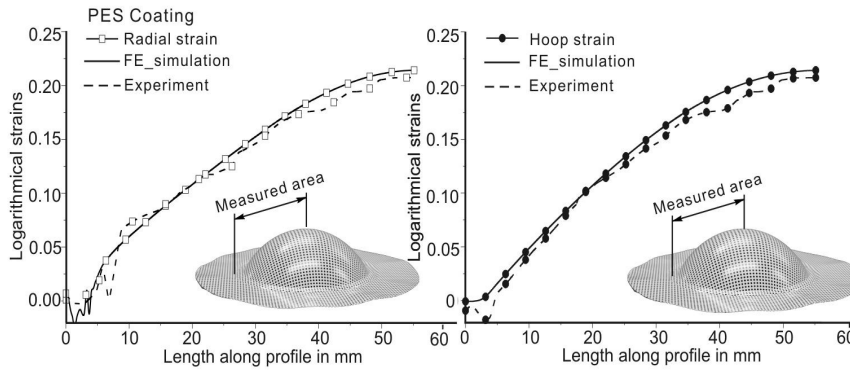


Fig. 5-15: Comparison of strains on the coating layer of the hydraulic bulge test - PES coating

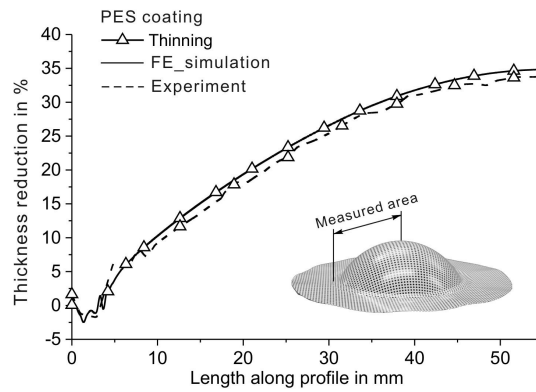


Fig. 5-16: Comparison of thinning distribution - PES coating

Only a slight deviation was observed between the two results. The numerically predicted strains are partially higher than the experimentally determined strains. This deviation occurs at the top of the deformed part, where these strains are regular in all directions, i.e. $\phi_1 = \phi_2$.

5.4.2.2 Circular cup deep drawing process

Similar to the hydraulic bulge test, the validated procedure of the FE results for the circular cup deep drawing is shown in Fig. 5-17.

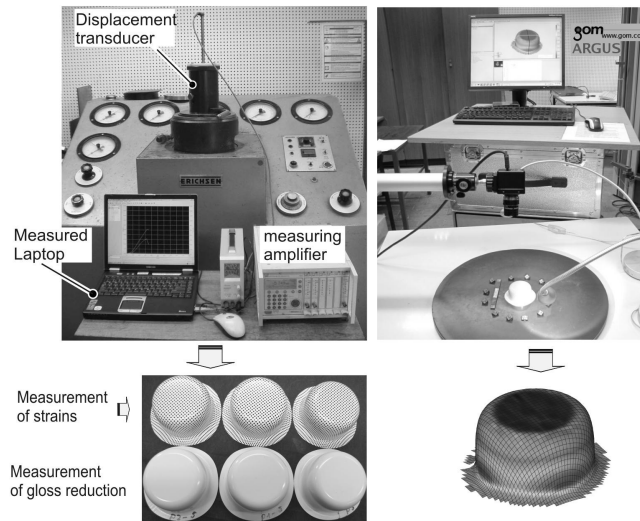


Fig. 5-17: Procedure for validation of the cup deep drawing simulation

For this purpose, the circular cup deep-drawing tests were conducted on the same *Erichsen* universal testing machine at room temperature. The prepared procedure such as printing of the

grid on both sides of the specimens is similar to the hydraulic bulge test. In this case, the circular specimens with a diameter of 100 mm were cut from the PUR and the PES coated sheet metal. The radial strain, the hoop strain and the thinning distribution of the cup are chosen as comparative parameters.

In Fig. 5-18 and Fig. 5-19 the comparisons between the numerical and experimental results of the PUR coated cup are depicted. As can be seen, the numerically predicted strain components and the thinning distribution are in good agreement with the experimentally determined results. The numerical radial and the hoop strains are found to be partially lower than the correspondent parameters for the experimental results. The maximum deviation of the strain values occurs with the cup wall portion and is smaller than 4%. The thinning distribution shows a similar tendency. It is seen that the numerically predicted thickness value is partially lower than the experimentally measured value. This effect occurs with the bottom of the cup and a part of the cup wall. The comparison shows that the maximum deviation between the FE and the measured thickness is smaller than 3%.

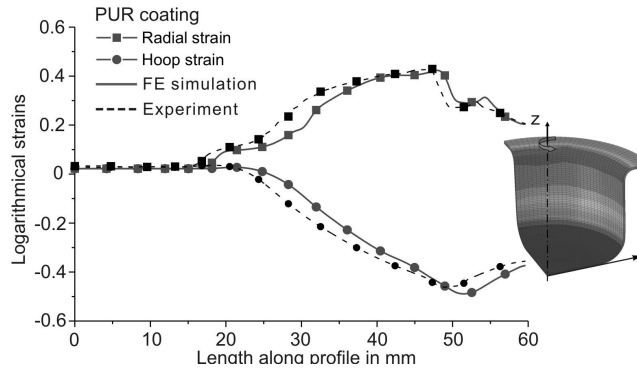


Fig. 5-18: Radial and hoop strain obtained by FE simulation and experiment – PUR coated cup

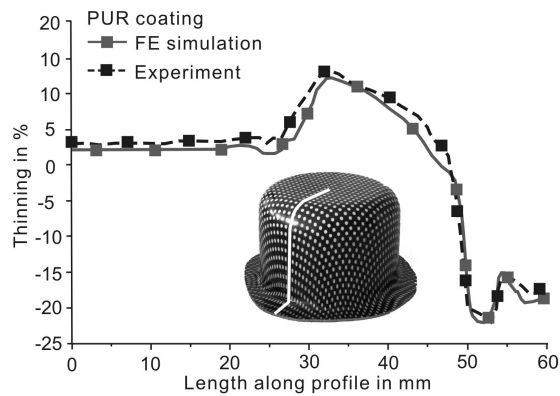


Fig. 5-19: Comparison of thinning distribution - PUR coated cup

In Fig. 5-20 and Fig. 5-21 the comparison between the numerical and the experimental results in case of the PES coated cup are displayed.

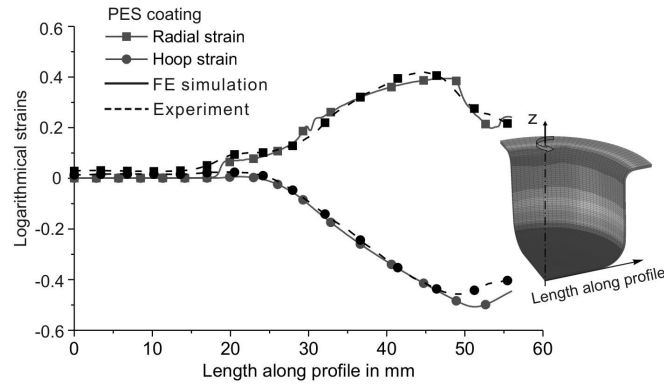


Fig. 5-20: Radial and hoop strain obtained by FE simulation and experiment – PES coated cup

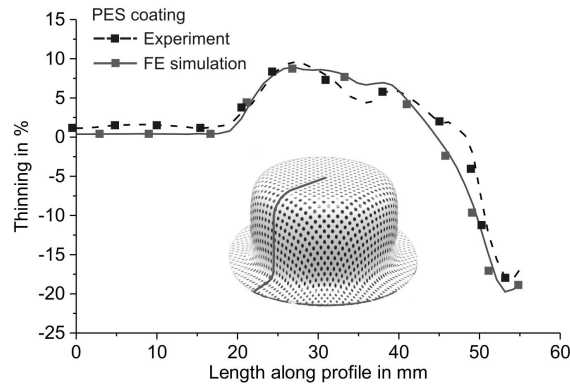


Fig. 5-21: Comparison of thinning distribution of the PES coated cup

Concerning the strain components, the difference between the two results are smaller than those in the case of computation with the PUR coating layer. Considering the thickness reduction, the numerically predicted thinning values are partially lower than the measured results. The maximum difference occurs in the side wall portion of the deep draw cup.

5.4.2.3. Square cup deep drawing process

The validated procedure of the square cup deep drawing simulation is similar to the circular cup deep drawing simulation. The experimental square cup deep drawing processes using PUR and PES coated sheets were also conducted on an *Erichsen* universal testing machine. The diameter of the PUR coated specimens is 100 mm while the correspondent one of the PES coated is only 95 mm due to the limited formability of the steel substrate.

The comparison between the FE and the experimentally measured results in the case of PUR coated sheet are shown in Fig. 5-22 and Fig. 5-23. Due to the geometrical characteristics, the strain distributions are taken along two representative lines: the first one goes from the center point of the bottom to the middle point of the part edge (section A); the other one also starts at the central-bottom point, but goes to the corner of the part (section B).

The square cup results in different strain distributions over the circumference of the part. The radial and hoop strains along the section A are definitely different from those along the section B. In the bottom area of the part, there is a slight stretching of sheet metal. The essential deformation begins at the inlet of the punch radius. Similar to the axisymmetrical case, the larger deformation is observed in the area shortly after the punch radius, i.e. the sidewall area. The radial strain around the die radius is slightly reduced due to the bending effect. In the flange area, both the radial and hoop strain are continuously increased. The thickness of the sheet in the flange area is, thus, thicker than the original one.

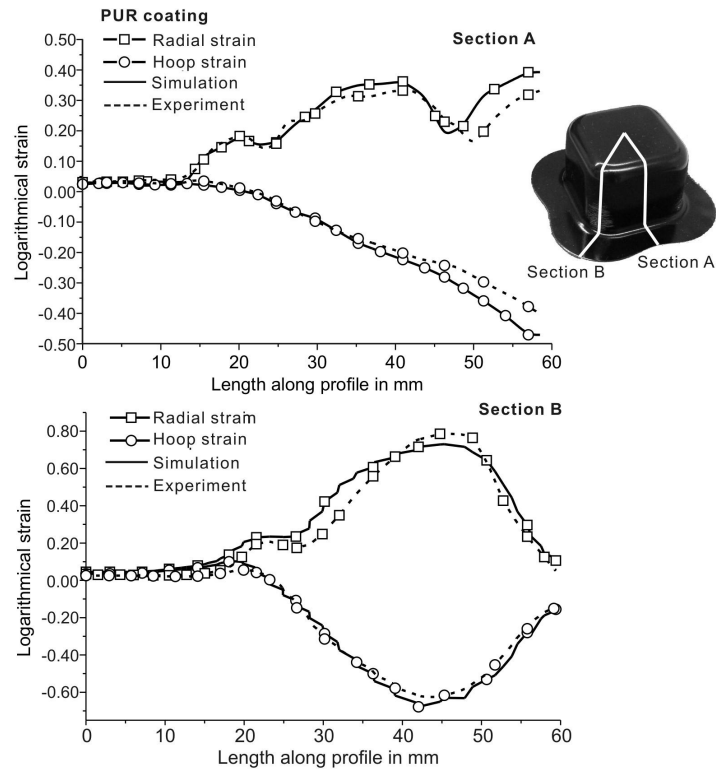


Fig. 5-22: Comparison of strain distributions of the PUR coated square cup

The numerically predicted strains along the section B are similar to the deformation trend of the circle cup. However, the radial tensile strain and the tangential compressive strain are

significantly higher than those of the section A. The largest decrease of thickness is observed at the outlet of the punch radius. As a result, this area of the square cup preferentially tears on account of too much stretching of the sheet metal. At the sidewall area, it is observed that not only the radial strain but also the tangential strain rises and reaches the maximal value. Then, these strains fall off to the rim of the flange area. The sheet thickness in the sidewall area increases due to high the tangential compressive strain, i.e. negative strain φ_2 .

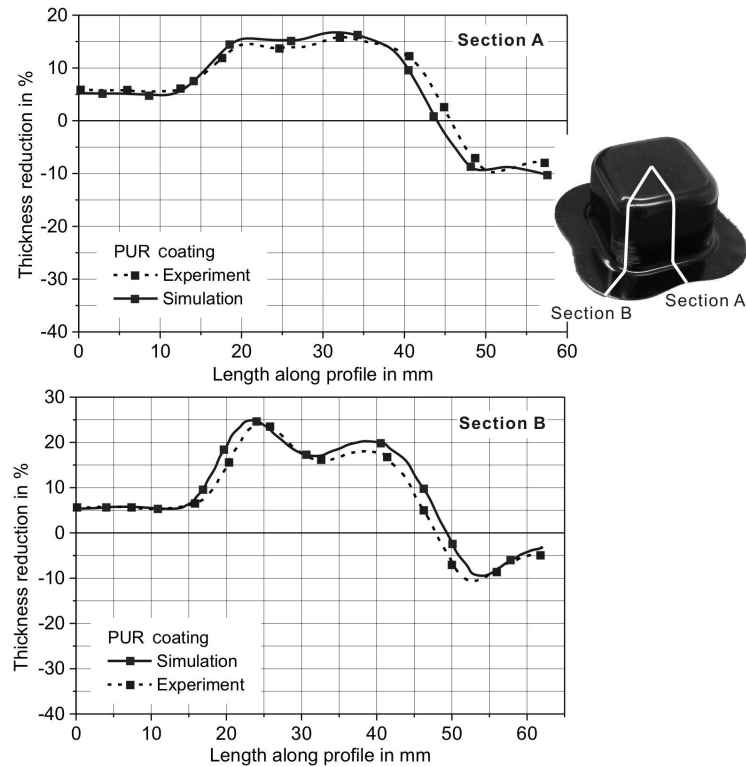


Fig. 5-23: Comparison of thickness reduction of the PUR coated square cup

Taking into consideration the strain distribution along the section A, there is a slight deviation at the flange area of the part. Along the section B, the deviation is partially occurred at the sidewall area of the radial strain. No considerable difference is observed on the tangential strain. Both the thickness reductions along the section A and B show a slight deviation at the sidewall area of the part.

In Fig. 5-24 and Fig. 5-25, the comparisons between the numerically and the experimentally determined results of the PES coated square cup are shown.

Concerning the radial and the hoop strain along the significant section A, only a small deviation at the lower corner around the punch radius and the flange area is observed. Along

the section B, the similar tendency is observed. The slight deviation is located at the punch radius and the flange area. These resulting deviations are within the accuracy range of the measured apparatus and cannot be avoided. The comparisons have indicated that the difference between the numerical and the experimental strain is less than 4 %.

The comparison of the thickness reductions along the section A and B contribute a similar observation as compared to the radial and the tangential deformation. Along the section A, the predicted thickness reductions and the measured one in the bottom area of the square cup are nearly identical as only a small deformation occurs. The maximal deviation occurs at the corner around the punch radius, the area which includes a portion of the sidewall and the corner around the die radius. Along the section B, the predicted thickness reduction of the sheet thickness takes place at the end of the punch radius and reaches a value of 26 % while the correspondent one of the experiment is approximately 23 %.

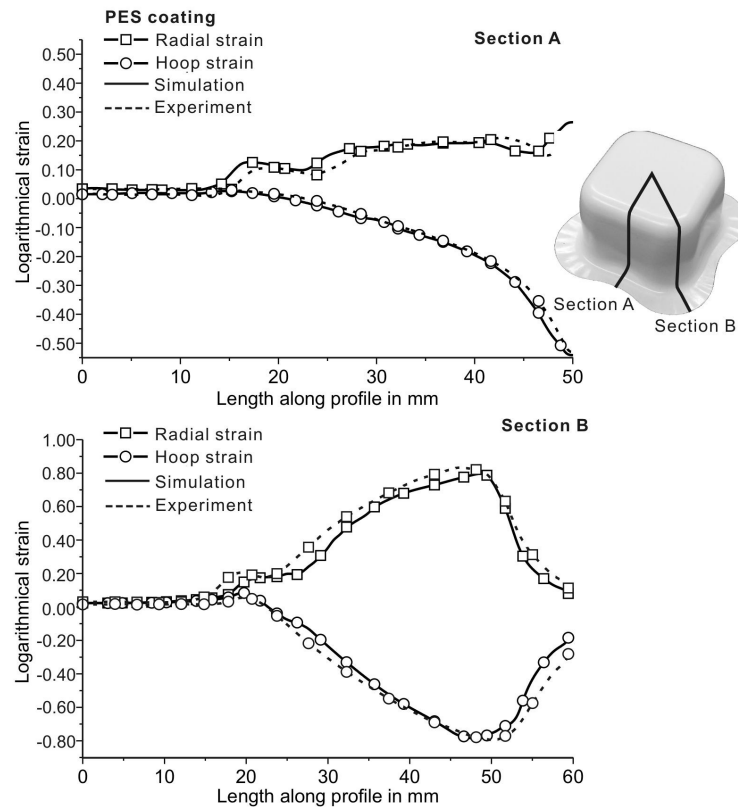


Fig. 5-24: Comparison of thickness reduction of the PES coated square cup

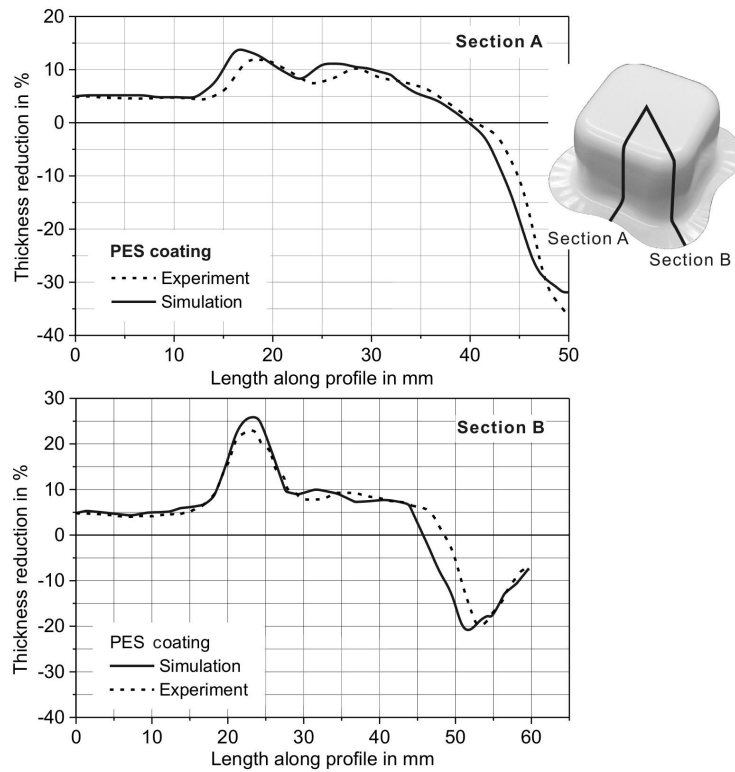


Fig. 5-25: Comparison of thickness reduction of the PUR coated square cup

In summary, it can be concluded that all simulation results are in good agreement with the experimental results. The observed slight deviations between the two results are due to “outdoor” factors not included in FE modeling, and inhomogeneous properties of the material. In addition to that, the strain analysis using *Argus* optical system is strongly dependent on the number of the printed grid points on the radius and the light reflection on the measured surface. This may lead to the deviation between the two results. However, all comparisons indicate that the maximal resulting deviations are lower than 5%. This deviation value can thus be acceptable. As a result, the potential and the feasibility of the proposed simulation strategy are proven. In the next section, the benefit of the proposed strategy will be discussed.

5.4.3 Benefit assessment of modeling with coating layer

Considering the coating layer in an FE model, the proposed strategy has shown two considerable advantages as compared to the case of the modeling without coating layer.

5.4.3.1. Improvement of computational accuracy

A veritable advantage is the improvement of computational accuracy by considering the coating layer in an FE model. In order to observe this effect, the obtained strain distributions of both the steel substrate and the coating layer for the deep drawing process of the PUR and PES coated sheets are plotted together as shown in Fig. 5-26 and Fig. 5-27, respectively.

As can be seen, the bottom of the cup, which is in contact with the punch throughout the process, is deformed only on a small level. As a result, the thickness of the blank in this area is nearly constant. Both computations show that the strain distributions on the coating layer and the steel substrate at the bottom of the cup are identical.

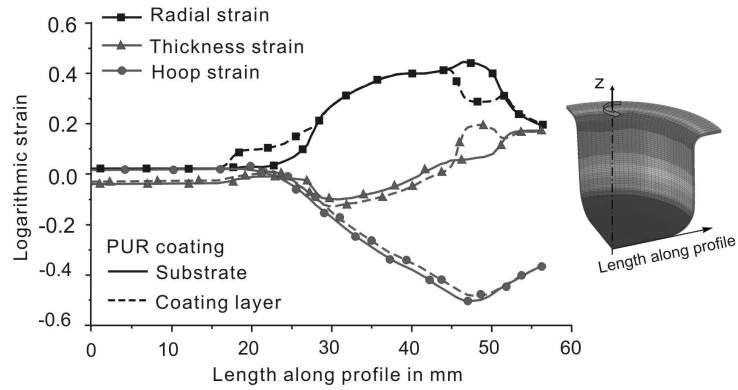


Fig. 5-26: Strain distributions of the PUR coated cup

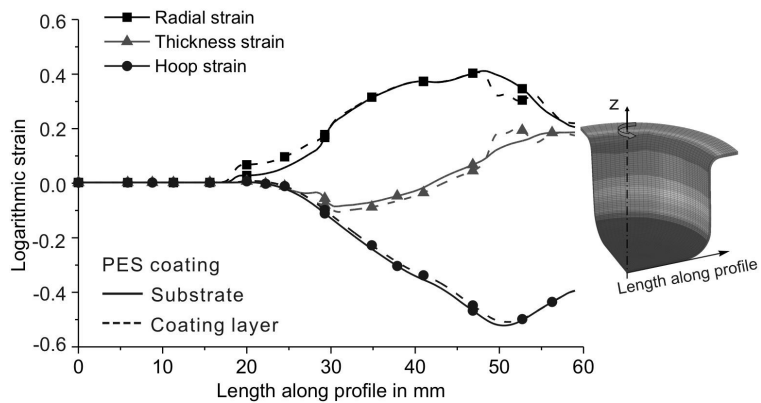


Fig. 5-27: Strain distributions of the PES coated cup

At the side wall area, the radial strain of both steel substrate and coating are also identical. A small difference concerning the hoop and the thickness strain in this area is observed. It is

seen that the hoop strain of the steel substrate is slightly higher than the one of the coating layer, whereas the thickness strain of the steel substrate is lower. However, a significant difference between the substrate and the coating is observed at the bottom corner around the punch and the top corner around the die due to the bending effect. Clearly, these areas are bent under tension during the forming process. As a result, the strain distribution is strongly dependent on the bending radius and the distance from the neutral line. Hence, a neglecting the coating layer would lead to an underestimating of the bending effect, resulting in the calculated strain deviations in the radii areas.

A comparison between Fig. 5-26 and Fig. 5-27 give an indication that the difference concerning the thickness, the hoop and the radial strain of the steel substrate and the coating layer in the case of the PES coated cup is lower than in the case of the PUR coated cup. The reason is that the total thickness and the coating thickness of the PES coated sheet are smaller than those of the PUR coated sheet metal.

5.4.3.1. Computation of stress distributions

Beside the improvement of accuracy, the modeling of the coating layer allows the determination of the stress distribution on the coating layer, see Fig. 5-28.

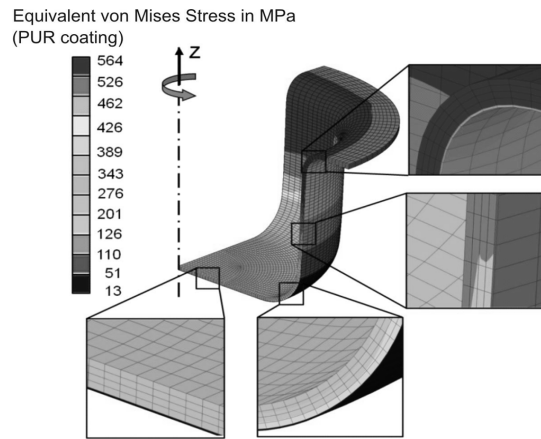


Fig. 5-28: Stress distribution on steel substrate and coating layer of the PUR coated cup

As can be seen, the numerically predicted results indicate that the coating layer undergoes a large elastic deformation while the metal substrate exhibits elastic-plastic deformation during the forming process. This characterization leads to the different stress distribution of both materials. As a result, the level of the equivalent stress of the coating layer is significantly lower than that of the steel substrate. As per reviewed literature, the imposed stresses on the coating layer are also the additional cause of the coating failure, in further processing. Therefore, the determination of the stress distribution on the coating layer plays an important role for the further development of an approach in order to predict the coating

damage based on stress criteria. However, this approach is not further considered in the frame of this research.

5.5 Prediction of surface quality based on FEM and experiment

5.5.1 Gloss reduction

In this section, the prediction of the change of the surface property, i.e. the gloss reduction on the basis of the numerical simulation and the experiment is expressed. Accordingly, the evaluated procedure as shown in Fig. 5-29 is conducted.

Firstly, it is necessary to establish the gloss reduction curves versus the different strain values and the strain states, as shown in Fig. 4-8, Fig. 4-9 and Fig. 4-10. Then, the forming process of OCSM is simulated to determine the strain level and the strain states over the forming parts. The simulation results are validated by the comparisons with the experimental results. Once the numerical results are validated, the measured gloss reduction obtained by experiments, which corresponds to the specific strain states and strain level, can be combined with the strain states obtained by the simulation. Combining the strain states as well as the strain values obtained by the FE simulation, the measured gloss reduction and the gloss reduction diagram (GRD), the change of the surface property, which corresponds to a specific the strain value and the strain state after the forming process, can be predicted.

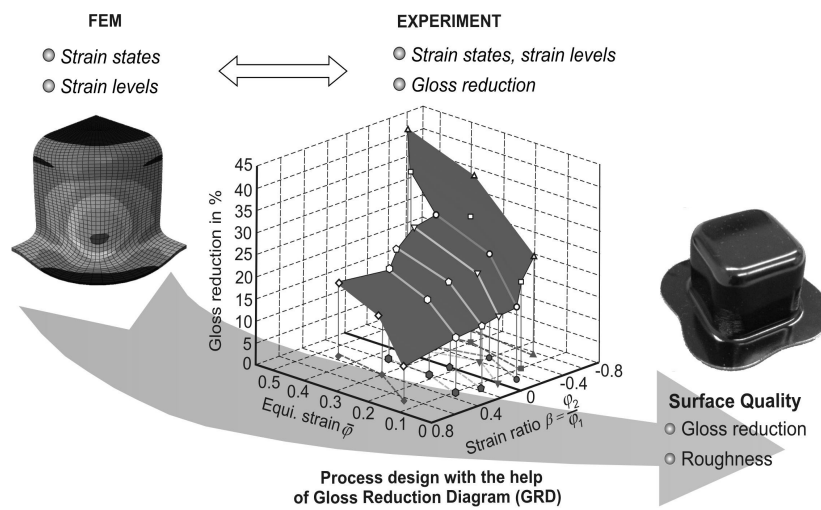


Fig. 5-29: Procedure for the evaluation of the change of surface property

To tackle this idea, the gloss reduction of the deep drawing cups is analyzed. The reason of the choice of the cup is its characteristic that remains the different strain states and the strain levels. According to the proposed method, the cup deep drawing process is first simulated. The FE results given in the section 5.4.2 are used. The numerically predicted strain distributions can be divided into different zones as shown in Fig. 5-30 and Fig. 5-31.

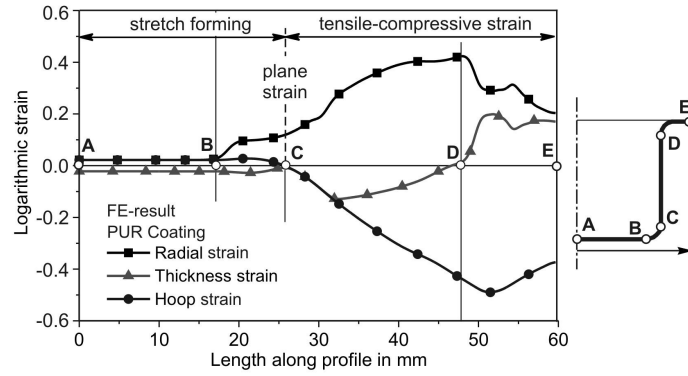


Fig. 5-30: Different strain states of the PUR coated cup

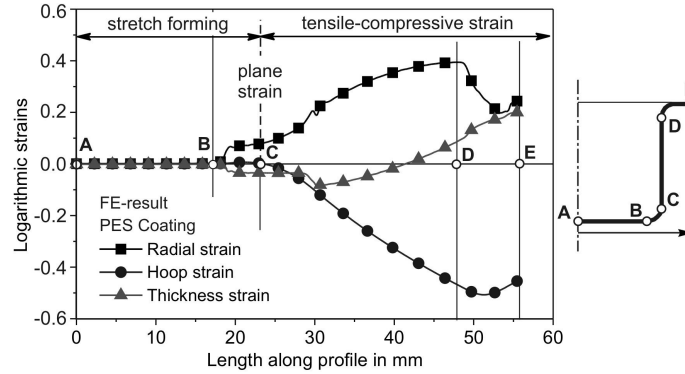


Fig. 5-31: Different strain states of the PES coated cup

The strain values at the three characteristic points which represent the different strain states are considered in detail.

- a point at the bottom area (denoted by *BT*),
- a point at the side wall area (denoted by *SW*),
- a point at the punch radius (denoted by *PR*).

Obviously, the bottom area of the cup in both cases remains the stretch forming and reaches the lowest strain value as compared to other areas. At the bottom corner around the punch radius, the numerically predicted strain value is significantly higher than the one at the bottom area. This area reveals a bending under tension. At the end of this area (point C), the plane strain state occurs. At the sidewall area, the strain level reaches the highest value and shows the deep drawing state. The considered points *BT*, *PR* and *SW* are inserted into the FLDC in order to compare the strain state and the strain level as shown in Fig. 5-32 and Fig. 5-33.

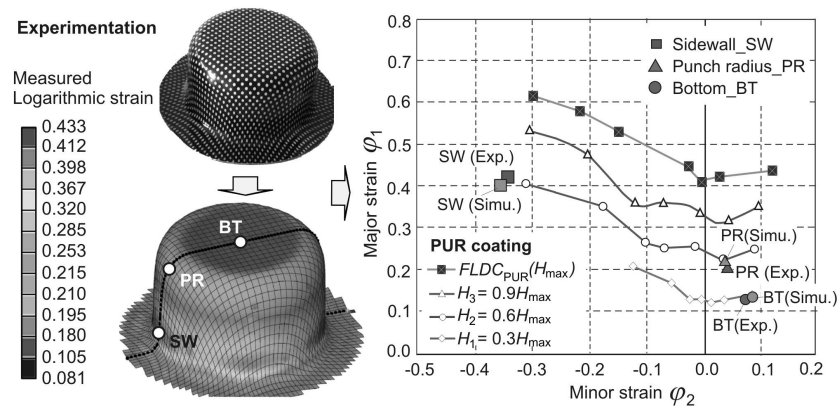


Fig. 5-32: Measured and predicted strains of the experimental cup - PUR coating

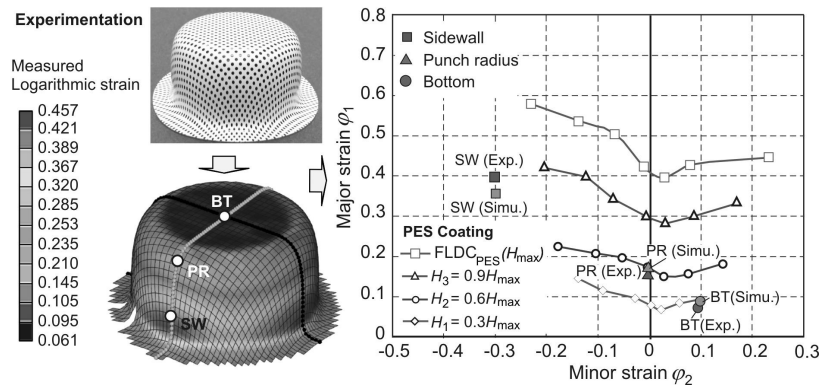


Fig. 5-33: Measured and predicted strains of the experimental cup - PES coating

It can clearly be seen that the strain level at the bottom of both the PUR and the PES coated cup (*BT* point) matches well the first specimen's strain value of the first series H_1 . The punch radius (*PR* point) of the PUR cup can be combined with the second specimen's strain value of the second series H_2 . For the PES coated cup, the strain level in this area can be associated with the strain value of the fourth specimen of the *Nakajima* series H_2 . At the sidewall area of the PUR cup, the strain value of the point *SW* can be combined with the seventh specimen's strain value of the second *Nakajima* series H_2 . At the sidewall area of the PES coated cup, the obtained strain can only be associated with the sixth specimen of the third series H_3 .

Based on the observations above, the gloss reduction at the bottom and the sidewall area can directly be drawn out without any interpolation due to a good match of the strain state and the strain level. Only the strain states at the point *SW* are beyond the one which could be reached by the *Nakajima* specimens. Concretely, the observed deviation between the strains of the

point *SW* and the reference strain of the *Nakajima* specimen is lower than 2 % in the case of the PUR coated cup and is approximately 4 % for the PES coated cup. Hence, the gloss reduction at the point *SW* of both the PUR and PES coated cup can only be evaluated by using an appropriated interpolation.

In Fig. 5-34 and Fig. 5-35, the correlations between the strain states at the points *BT*, *PR* and *SW* and the GRD of the PUR and the PES coated cup are illustrated.

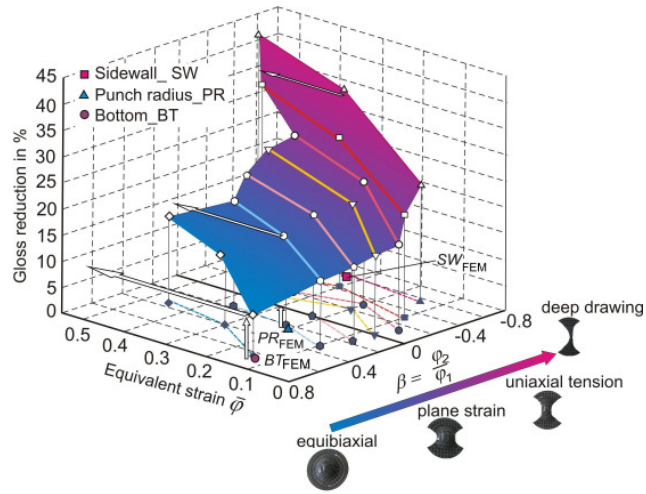


Fig. 5-34: Strain values of the PUR coated cup in association with GRD

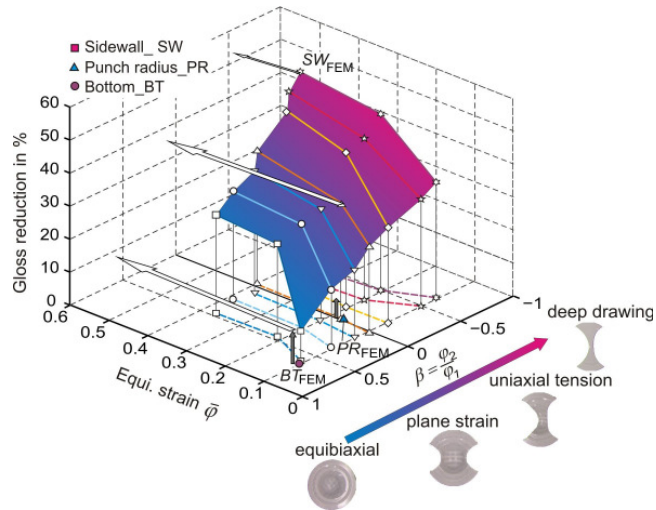


Fig. 5-35: Strain values of the PES coated cup in association with GRD

According to the results obtained by the reference *Nakajima* specimens, the predicted gloss reduction at the bottom area of the PUR cup is only $LG_{BT_FEM_PUR} = 7.7\%$. Around the punch radius, the gloss reduction is considerably higher than the one at the bottom area and reaches a value of $LG_{PR_FEM_PUR} = 14.2\%$. At the sidewall area, the gloss reduction reaches a value of $LG_{SW_FEM_PUR} = 34.5\%$. In the case of the PES coating, the correspondingly predicted gloss reductions are $LG_{BT_FEM_PES} = 9.02\%$, $LG_{PR_FEM_PES} = 37.22\%$ and $LG_{SW_FEM_PES} = 51.3\%$.

In order to validate the predicted results, the deep drawing tests using the PUR and the PES coatings are carried out. Then, the gloss reduction on the correspondent areas of the cup is measured using a special gloss apparatus, namely *NOVO-CURVE*. A comparison between the experimentally measured results obtained by the cup deep-drawing test and the reference gloss reduction is shown in Table 5-5.

Table 5-5: Comparison between the predicted and measured gloss reduction

	Predicted gloss reduction on deep drawing part in %		Measured gloss reduction in %		Deviation in %	
	PUR Coating	PES Coating	PUR Coating	PES Coating	PUR Coating	PES Coating
Bottom	7.70	9.02	5.20	11.63	2.50	2.61
Punch radius	14.20	37.22	16.50	41.67	2.30	4.45
Sidewall	34.50	51.30	37.50	54.80	3.00	3.50

It can be seen that the deviation between the gloss values of the *Nakajima* specimens and the deep drawing part at assimilable states, i.e. points *BT* and *PR*, are between 2-3 %. The maximal deviation is 4.45 % and occurs at the punch radius due to the difficulty of the gloss measurement on the small curvature radius. Only at the point *SW* of both investigated materials, an interpolation of the gloss values is required. The deviation between the interpolated reference data and the experimentally determined gloss values of the PUR and the PES deep drawing parts are 3 % and 3.50 %, respectively. All the observations indicate that the deviation between the measured and the predicted gloss reduction is smaller than 5 %. This is the accuracy range of the measurement apparatus and is therefore acceptable.

5.5.2 Cracking of the coating layer

Cracking is the failure that leads to a loss of attractive and protective properties of the coating layer. The cracking occurs due to high sufficient tensile stress on the coating layer resulting from large deformations on the steel substrate. In order to predict cracking of the coating layer, the established FLDCs are employed. In this section, the prediction of the cracking of the circular and square deep drawing cup using OCSM is presented.

To this end, the deep drawing processes using PUR and PES coated sheets are simulated to determine the strain distribution and to establish the strain diagram. The strain diagram is the result of plotting the strain value at different areas in the principal strain space, *Marciniak & Duncan (1991)*. The strain diagrams of the PUR and the PES coated cups in association with the correspondent FLDC are depicted in Fig. 5-36 and Fig. 5-37, respectively.

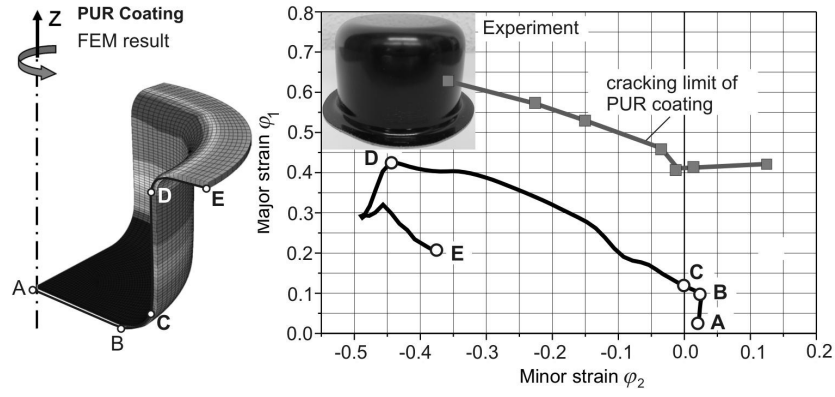


Fig. 5-36: Strain diagram and FLDC of the PUR coated cup

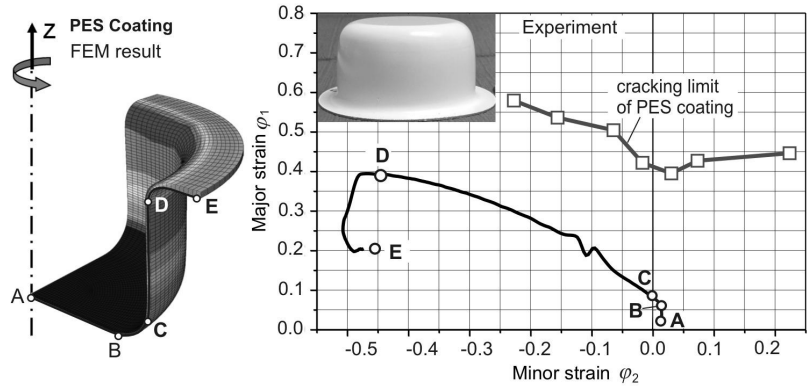


Fig. 5-37: Strain diagram and FLDC of the PES coated cup

In Fig. 5-38, the predicted strain value in conjunction with the FLDC and the experimentally conducted square cup in the case of the PUS coating layer are displayed. It can be seen that the numerically predicted strain at the corner of the square cup is significantly higher than the correspondent one of the FLDC. This results in a very high thinning of the coating layer. In the conducted experimentation, the cracking of the PUR coating is observed at the corner of the square cup. A comparison between the simulation and the experimentation gives an indication that the numerical prediction is in good agreement with the experimentally determined results.

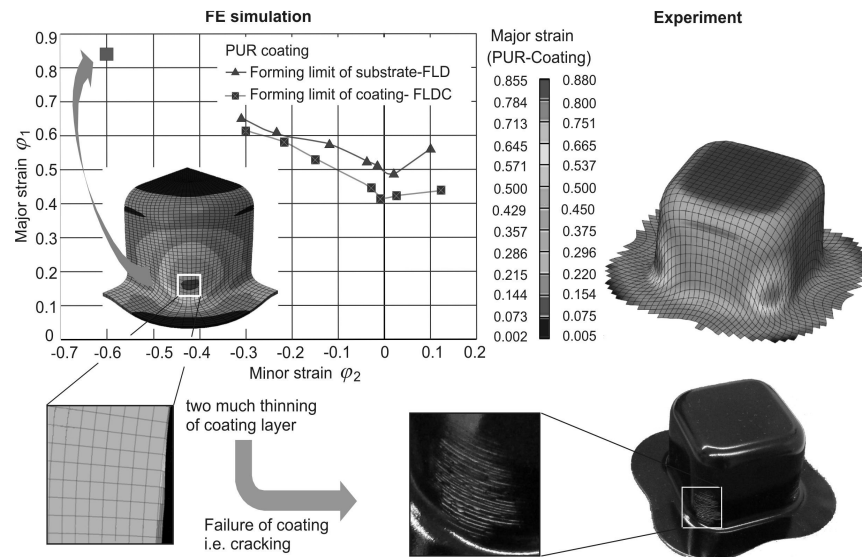


Fig. 5-38: Cracking on the coating layer of the PUR coated square cup

The investigations above demonstrate that the analyzed results of the deep-drawing part consolidate the reference data obtained by the Nakajima test. As a result, the reference data can be applied to predict the optical properties of the OCSM products after an industrial forming process. According to the proposed method, it is necessary to establish the gloss reduction curves versus the different strain values. Then, based on these sample curves, the gloss reduction which corresponds to a specific strain value and strain state can be predicted.

Hence, the design phase of an OCSM product should be conducted as follows. First, the forming process of OCSM is simulated. The obtained numerical strain distributions are then validated. By using the validated simulation results, the strain values and deformation states in different regions of the product are correlated with the obtained GRD. Afterward, the surface quality of the product can be evaluated by combining the FLDC, the GRD and the simulation results.

5.6 Conclusion

The simulation of forming processes with OCSM, such as hydraulic bulge test, circular and square cup deep drawing process, has shown the good applicability of the proposed modeling strategy. It can be seen that the deformation of the coating layer is partially similar to the steel substrate on account of the very thin thickness. In case of stretch forming, the maximal deviation concerning the strain distribution over the forming part occurred with the thickness strain. In case of the deep drawing process, the strain deviation is observed at the corner around the punch radius and the die radius on account of the bending effect. The numerically predicted strains also give an indication that the strain deviation increases with increasing

coating thickness. For industrial problems where the shape of the forming part is usually complex, it is recommended that the coating layer should be considered in the FE model in order to evaluate precisely the change of the coating performances such as the gloss reduction, the cracking and the delamination. Obviously, the modeling with the coating layer improves the computational accuracy.

The proposed strategy for the prediction of the optical property changed by using the FE simulation in conjunction with the reference *Nakajima* test have proven the applicability of the used strategy with an acceptable accuracy. The obtained FLDC can be successfully used to predict the failure of the OCSM products.

In the next chapter, the transferability of the proposed simulation strategy for the forming of a complex geometry in the automobile industry is discussed. The obtained relations in chapter four are utilized to optimize the process parameters of the HDD forming technique.

6 Material-specific process design of hydro-mechanical deep drawing for organically coated sheet metal

As investigated above, the change of the surface properties of the OCSM is significantly dependent on the strain state and the strain level of the formed part. Hence, the surface quality can be adapted or optimized if both strain states and strain level could be regulated. In this chapter, this knowledge gained in Chapter 4 and Chapter 5 is used for the design of hydro-mechanical deep drawing (HDD) to manufacture a parabolic reflector made of OCSM. By combining the main process parameters, i.e. the hydraulic counter pressure and the blank holder force, the strain states over the parabolic reflector part are controlled in order to shift the strain state in direction to positive strain ratios ($\beta > 0$) that provides the minimum of the gloss reduction. The changes of the surface properties, e.g. the gloss value depending on the strain states and the strain ratio of the parabolic reflector part are also presented in this section.

6.1 Manufacturing of parabolic reflector part by means of HDD technique

Lighting reflectors from the coil coated sheet metal are an interesting alternative in the automobile industry as compared to the plastic headlight systems because of the economic efficiency, the high temperature resistance and the high thermal conductivity, *Kleiner & Rogner (2004)*. The common form of the lighting reflector part is a parabolic due to its characterization of the light reflection during the working process, Fig. 6- 1.



Fig. 6- 1: Passenger headlamp system

Paraboloid is one of the typical geometries that cannot be formed in one step by means of the conventional forming techniques due to the occurrence of large unsupported forming zones which can lead to the wall wrinkles. By using the HDD technology, this geometry can be formed with a reduced number of forming steps compared to the conventional forming methods as shown in Fig. 2- 18, while the dimensional accuracy and the surface quality are remarkably improved. Comparably to the conventional deep drawing process, the process window of the HDD is limited by the occurrence of the defects like necking, rupture or extensive thinning on the one hand or wrinkling at the part flange or at the sidewall on the other hand.

6.2 Experimental set-up for HDD process

In this section, the HDD tooling system, which is utilized to conduct the HDD experiment in order to validate the numerical investigation concerning the influence of the BHF and the counter pressure on the surface quality of OCSM, are presented.

The HDD tooling system for all experimentations is first designed and manufactured. Fig. 6-2 depicts the 3D model and the manufactured tool. The die design for the HDD tooling requires a particular attention due to the high fluid pressure acting directly on the sheet metal. The counter pressure recipient is designed as a thick-shell pressure vessel by using a high strength steel. An axial sealing is pressed into a groove in the die ring in order to avoid leakage of the fluid. The BHF is generally generated independent of the press force by using an external hydraulic unit or by employing the blank holder slide in a double-acting press. In this design, the four hydraulic cylinders created the BHF through the blank holder plate. The BHF is controlled by an external hydraulic system that can change the working pressure in each cylinder.

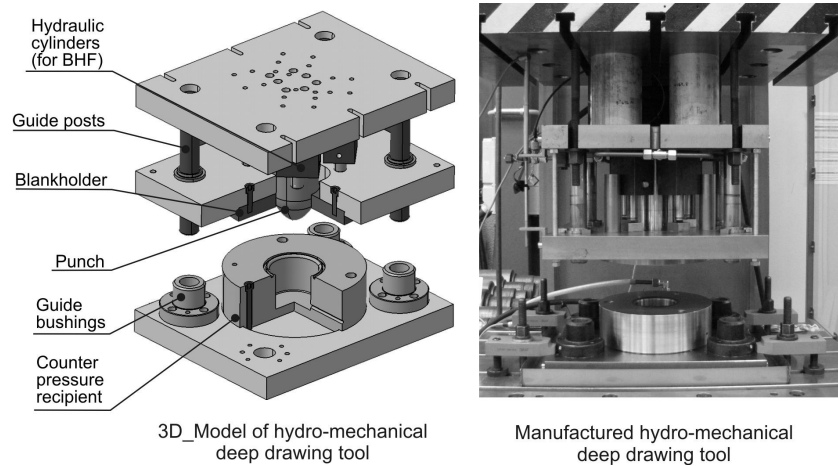


Fig. 6- 2: Tooling system for HDD process

To regulate the counter pressure in the pressure chamber, another external hydraulic system that consists of a controllable hydraulic cylinder and a proportional 4/2 direction valve was utilized. The volume and the oil pressure are regulated by controlling the position of the controllable cylinder through the proportional direction valve. With this system, a pressure value of 35 MPa can be created. An additional relief valve was used as safety valve to avoid bursting of the sealed counter pressure chamber. The controllable cylinder is connected with the relief valve by using a hydraulic pipe. The completed hydraulic circuit that is utilized in order to control and regulate the counter pressure in the HDD process is illustrated in Fig. 6-3.

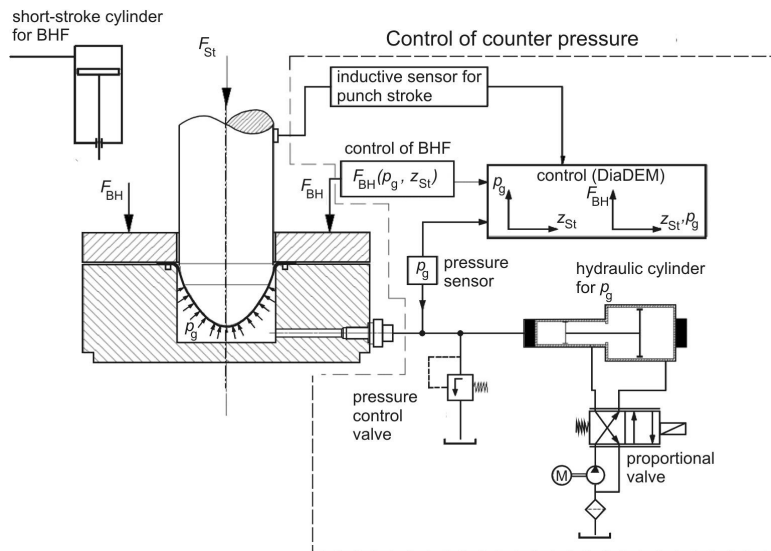


Fig. 6- 3: Hydraulic schema for regulating counter pressure depending on punch travel

During the forming process, the hydraulic oil in the pressure chamber is replaced when the punch descends. The volume flow is controlled via the relief valve and the controllable cylinder that can ensure the required pressure. When the punch reaches the bottom dead point that corresponds to the maximal height of the part, the oil in the pressure chamber cannot be replaced anymore. At that time, the controllable cylinder will provide an additional hydraulic pressure in order to calibrate the forming part.

During the HDD process, the punch travel is the key parameter to be controlled because both the counter pressure and the BHF depend on the punch travel. This parameter is measured by means of a travel sensor which is mounted on the upper plate of the die set. In this context, the counter pressure and the BHF depending on the punch travel act as input data of the process. In order to control the BHF and the counter pressure depending on the punch travel, the control software *DIADeM* of National Instrument software package was employed. This software allows establishing an online close-loop control of any manufacturing process.

For all conducted experimental investigations, a modern CNC-programmable hydraulic press of the *Schuler Hydrap Company* (Model HPSZK 100) was utilized, Fig. 6- 4.

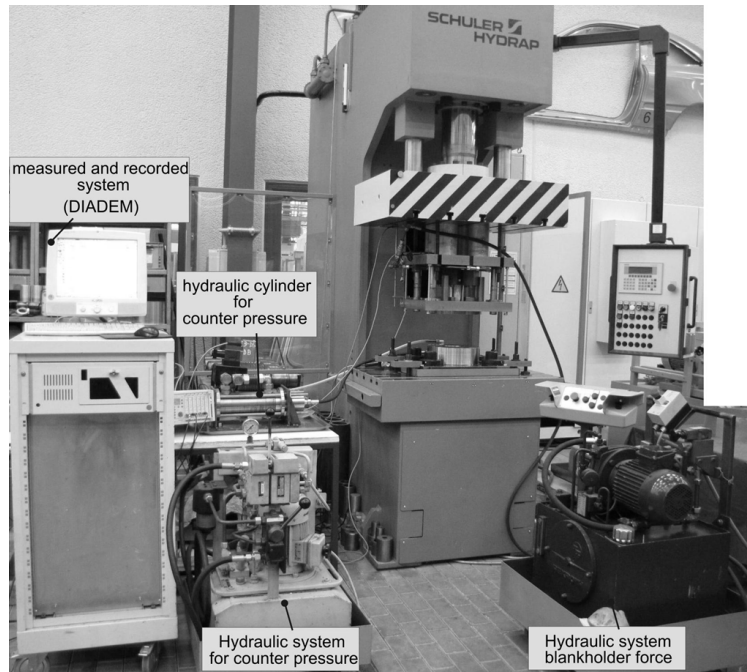


Fig. 6- 4: Experimental equipment for HDD process

6.3 Analytical model for HDD process

In order to investigate the influence of special process parameters like counter pressure and blank holder force on the strain states and strain distribution over the forming part, an analytical model of the HDD process for the parabolic part is first presented. The relations between the strain, the stress and the process parameters as well as the geometrical parameters in different areas are established. These establishments in this work are fundamentally based on the analytical model for the hydroforming of hemispherical cups, which is contributed by *Lo et al. (1993)*. However, *Lo* only established and focused on formulas for the flange and the unsupported region to compute the limit (failure) counter pressure at plastic instabilities (rupture and wrinkling instability). However, the punch-head area was neglected on account of the assumption of rigid movement with punch during the forming process.

The exploitation here is basically in opposite direction as compared to *Lo's* contribution. The new idea is that a computational algorithm and a *MATLAB* program are developed that allow the computation of the strain distribution of the forming part depending on varying counter pressure and the BHF. Using the developed *MATLAB* tool, the influence of the process parameters can be investigated very fast (within several seconds) in order to get the desired

strain distributions that provide the best surface quality, as presented in chapter four. A further contribution of this research work is the adaption of the analytical model to a more complicated geometry, i.e. the parabolic form. Hence, the relations between the process parameters and the geometrical parameters are also different compared to the hemispherical form. The deformation process is completely investigated from the flange to the unsupported region and the punch-head region. It has to be noted that, at the beginning of forming process, the sheet metal in the punch-head region undergoes plastic deformation which is preserved by a friction force. Then, it moves with the punch as a rigid body. In this research, the strain distributions of the sheet in the punch head region have to be considered because they play an important role for evaluations of the surface quality.

The deformation process involved in the HDD process can be divided into three stages. First, the sheet metal undergoes a radial drawing in the flange area. Then, in the unsupported area occurs plastic bending and unbending around the die radius under the presence of hydraulic pressure in the water pot. At the same time, the sheet metal which is in contact with the top area of the punch is formed into the water pot when the punch descends. After that, the sheet metal is pressed onto the punch wall by hydraulic pressure on the opposite side of the sheet metal because the punch moves continuously down into the die cavity, Fig. 6- 5.

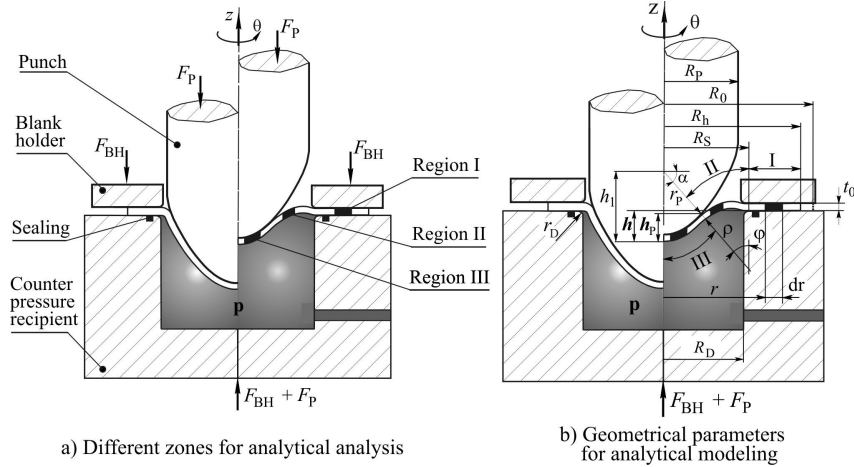


Fig. 6- 5: Deformation process involved in HDD and geometrical parameters

In order to analyze the strain and stress of the HDD process with the parabolic part, the work piece is divided into three parts according to the deformed shape which is named flange (region I), unsupported (region II) and punch-head region (region III). It is noted that the size of these regions depends significantly on the punch travel. The first two regions undergo large plastic deformation during the forming process. The third one first undergoes plastic deformation. Then, it moves with the punch, which can be assumed to be a rigid movement. Fig. 6- 5b illustrates these different computational regions of the HDD process.

For ease of comprehension, the basic knowledge used and the main set of equations derived by *Lo et al. (1993)* are summarized. The differences regarding the geometrical relations in each region compared to the hemispherical form in *Lo's* contribution are also pointed out.

6.3.1 Strain and stress analysis in the flange region (Region I)

The stresses acting on an element at radius r in the flange region (Region I) is shown in Fig. 6- 6. In order to establish the equilibrium equation, an element with the thickness t on the flange region is considered. The friction coefficient between the blank and the blank holder and the die surface are denoted by μ_1 and μ_2 , respectively.

The following basic assumptions are considered:

- The punch and die are assumed to be rigid bodies.
- The geometry of the part is a surface of revolution, thus it is symmetric about a central axis. The thickness, the loads and the stresses are axisymmetrical during forming.
- Bending moments are negligible ($\sigma_3 = 0$).
- Because of axial symmetry, the hoop (σ_θ) and the radial (σ_r) stresses are principal ($\sigma_1 = \sigma_r$, $\sigma_2 = \sigma_\theta$).
- The sheet metal thickness t is constant during the forming process.
- *Tresca* flow condition is assumed to be applicable.

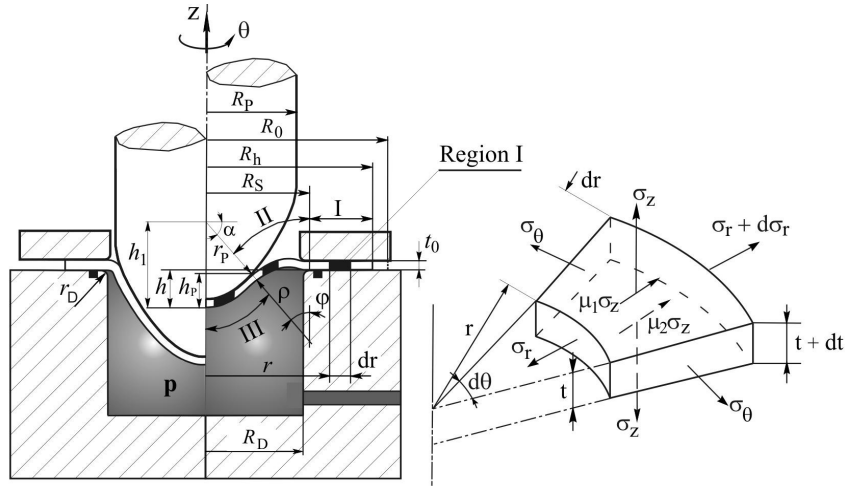


Fig. 6- 6: Stresses on an element at the flange area

As presented in Fig. 6- 6, the force equilibrium in radial drawing direction can be written as:

$$-\sigma_r t r d\theta + (\sigma_r + d\sigma_r)(t + dt)(r + dr)d\theta + (\mu_1 + \mu_2)r\sigma_z d\theta dr - 2\sigma_\theta(t + \frac{dt}{2})dr \sin \frac{d\theta}{2} = 0 \quad (6. 1)$$

The polar equilibrium equation in this case is given as follows, *Lo et al. (1993)*:

$$\frac{d(t\sigma_r)}{dr} + \frac{t}{r}(\sigma_r - \sigma_\theta) + F(p_1) = 0 \quad (6.2)$$

where $F(p_1)$ is the total friction force on both surfaces of the flange region.

$$F(p_1) = (\mu_1 + \mu_2)p_1 \quad (6.3)$$

where p_1 is blank holder pressure.

By substitution of the *Tresca* yield condition, the equation (6.2) is rewritten as:

$$\frac{d\sigma_r}{dr} + \frac{1}{r}\bar{\sigma} + \frac{(\mu_1 + \mu_2)p_1}{t} = 0 \quad (6.4)$$

By taking integration in the range from R_S to R_h , equation (6.4) can be derived as follows:

$$\sigma_r = \int_{R_S}^{R_h} \bar{\sigma} dr + \frac{(\mu_1 + \mu_2)p_1}{t}(R_h - R_S) = 0 \quad (6.5)$$

Assuming the sheet metal follows a generalized *Swift's* power-hardening law:

$$\bar{\sigma} = K(\varepsilon_0 + \bar{\varepsilon})^n \quad (6.6)$$

where K , ε_0 , and n are the material constant characterizing the flow stress and the hardening of the material. Thus, equation (6.5) is rewritten as:

$$\sigma_r^I = \int_{R_S}^{R_h} \frac{K(\varepsilon_0 + \bar{\varepsilon})^n}{r} dr + \frac{(\mu_1 + \mu_2)p_1}{t}(R_h - R_S) = 0 \quad (6.7)$$

Based on Hill's anisotropy yield condition *Hill (1950)*, the equivalent strain rate is denoted as:

$$\dot{\bar{\varepsilon}} = \frac{1+R}{\sqrt{1+2R}} \sqrt{\dot{\varepsilon}_r^2 + \frac{2R}{1+R} \dot{\varepsilon}_r \dot{\varepsilon}_\theta + \dot{\varepsilon}_\theta^2} \quad (6.8)$$

where R is the parameter that represents the orthotropic of the sheet material.

In this area, the change of the sheet thickness is not large and thus, it was assumed that it can be neglected. The volume constancy condition leads to:

$$\dot{\varepsilon}_\theta = -\dot{\varepsilon}_r \quad \text{or} \quad \varepsilon_\theta = -\varepsilon_r \quad (6.9)$$

The equivalent strain can be obtained by integrating the equation (6.8) with respect to the relation in equation (6.9), *Lo et al. (1993)*:

$$\bar{\varepsilon} = \frac{\sqrt{2(1+R)}}{\sqrt{1+2R}} \varepsilon_r = \bar{R} \varepsilon_r \quad (6.10)$$

The radial strain ε_r can be determined as follows:

$$\varepsilon_r = -\int_{r_0}^r \frac{dr}{r} = \ln \frac{r_0^I}{r} \quad (6.11)$$

In equation (6.11) r is the current radius of a computational element which has the initial location on the undeformed blank with the radius r_0^I . The relation between r , punch travel h ,

and current curvature ρ , in case of r between $(r_p + \rho)\cos\alpha$ and R_h is computed on the basis of the volume constancy condition and is expressed as follows.

$$(r_o')^2 = r_p^2 \left(\begin{aligned} & \left(\frac{r}{r_p} \right)^2 - \left(1 + \rho/r_p \right)^2 \cos^2 \alpha + 2(1 - \sin \alpha) \left[1 - \left(\rho/r_p \right)^2 \right] \\ & + 2(\rho/r_p)(1 + \rho/r_p)(\pi/2 - \alpha) \cos \alpha \end{aligned} \right) \quad (6.12)$$

with $\alpha = \arcsin[(r_p + \rho - h_p)/(r_p + \rho)]$

In the equation (6.12), r_p is the normal radius of the end-contact point between the punch and sheet. This radius is varied depending on the punch travel during the forming process. This is also the main feature of the parabolic geometry leading to the difference in geometrical relations.

By the solving equations (6.7) referring to the relations in (6.10), (6.11) and (6.12), the stress and strain distribution in the flange area are determined. Obviously, these distributions in this region depend mainly on the friction coefficients μ_1 , μ_2 , blank holder pressure p_1 and the counter pressure which is represented by the curvature ρ .

6.3.2 Strain and stress analysis in the unsupported region (Region II)

The form of the unsupported region can be considered as a part of shell of revolution (with the axis of revolution Oz), Fig. 6-7.

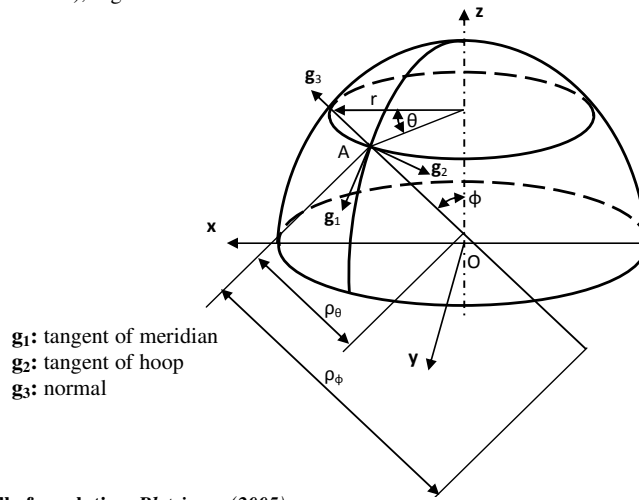


Fig. 6-7: Shell of revolution, Bletzinger (2005)

It is a doubly curved surface with a normal \mathbf{g}_3 at point A. Two tangent vectors in meridian and hoop direction are \mathbf{g}_1 and \mathbf{g}_2 , respectively. This surface has two radii of principle curvature, namely ρ_θ and ρ_ϕ . The following geometrical relations can be drawn:

$$\begin{aligned} r &= \rho_\theta \sin \phi \\ dr &= \rho_\theta \cos \phi d\phi \end{aligned} \quad (6.13)$$

Considering an element at radius r in the unsupported region, Fig. 6- 8, we have:

$$\begin{aligned} ds_1 &= \rho_\phi d\phi \\ ds_2 &= r d\theta = \rho_\theta \sin \phi d\theta \\ dA &= ds_1 ds_2 = \rho_\phi \rho_\theta \sin \phi d\phi d\theta \end{aligned} \quad (6. 14)$$

where dA is the element surface, ds_1 and ds_2 are the lengths of the element edges along the meridian and hoop directions, respectively.

In Fig. 6- 8, the stresses acting on an element at radius r in the unsupported area region, region II, are shown. Clearly, this is a symmetric geometry, hence, there are no in-plane shear stresses $\tau_{\phi\theta}$ and $\tau_{\theta\phi}$.

As shown in Fig. 6- 8, a shell element of sides ds_1 and ds_2 is considered. Due to the counter pressure there is no contact between the sheet metal and the die profile radius. The fluid pressure p acting on this element exerts an inward force F along the surface normal \mathbf{g}_3 :

$$F = p dA = p \rho_\phi \rho_\theta \sin \phi d\phi d\theta \quad (6. 15)$$

Due to the curvature of the shell element, the force in the hoop (circumferential) direction exerts an inward component in the horizontal direction:

$$F_\theta = \sigma_\theta t ds_1 = \sigma_\theta t \rho_\phi d\phi \quad (6. 16)$$

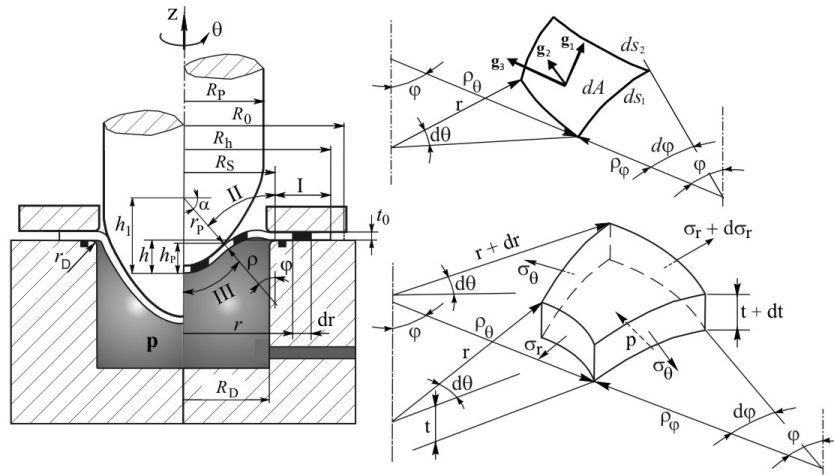


Fig. 6- 8: Stresses on an element at the unsupported region

The components of this force along the normal and the tangent to the surface in the direction of the meridian are:

$$\begin{aligned} F_\theta \sin \phi d\theta &= \sigma_\theta t \rho_\phi d\phi \sin \phi d\theta \\ F_\theta \cos \phi d\theta &= \sigma_\theta t \rho_\phi d\phi \cos \phi d\theta \end{aligned} \quad (6. 17)$$

The stresses along the meridian exert a force F_r :

$$F_r = \sigma_r t ds_2 = \sigma_r t \rho_\theta \sin \varphi d\theta \quad (6.18)$$

Similarly, due to the curvature of the shell element, F_r exerts force components in the surface normal and tangent of meridian, respectively, as:

$$F_r d\varphi$$

$$F_r + \frac{d(F_r)}{d\varphi} d\varphi - F_r = \frac{dF_r}{d\varphi} d\varphi \quad (6.19)$$

Hence, the equilibrium equation in the direction normal to the surface and in the direction of the meridian tangent can be written as:

$$F = F_\theta \sin \varphi d\theta + F_r d\varphi$$

$$\frac{dF_r}{d\varphi} d\varphi - F_\theta \cos \varphi d\theta = 0 \quad (6.20)$$

If we substitute the geometry relations from (6.13) to (6.19) into the equation (6.20), then we get the equilibrium conditions in the normal and in the meridian tangent as:

$$p = \left(\frac{\sigma_\theta}{\rho_\theta} + \frac{\sigma_r}{\rho_\varphi} \right) t \quad (6.21)$$

$$r \frac{d(\sigma_r)}{dr} + \sigma_r - \frac{\rho_\varphi}{\rho_\theta} \sigma_\theta = 0 \quad (6.22)$$

In case of a sphere geometry, we have $\rho_\theta = \rho_\varphi = \rho$, then (6.22) becomes:

$$\frac{d\sigma_r}{dr} + \frac{1}{r} (\sigma_r - \sigma_\theta) = 0 \quad (6.23)$$

For the sake of simplicity, the equation (6.23) is used. Integrating the equation (6.23), we obtain radial stress in region II:

$$\sigma_r^II = \int_{r_p \sin \varphi}^{(r_p + \rho) \sin \varphi} \frac{K(\varepsilon_0 + \bar{\varepsilon})^n}{r} dr + C \quad (6.24)$$

In the equation (6.24), the constant of integration C is the value of σ_r at the transition line between region I and region II. That means, the position r equals to $R_S = (r_p + \rho) \sin \varphi$. To solve the equation (6.24) and to compute the strain component at this region, the procedure is similar to the computation in region I with respect to the continuity condition of σ_r . Hence, the equation (6.24) becomes:

$$\sigma_r^II = \sigma_r^I [r = (r_p + \rho) \sin \varphi] + \int_r^{(r_p + \rho) \sin \varphi} \frac{K(\varepsilon_0 + \bar{\varepsilon})^n}{r} dr \quad (6.25)$$

And the hoop stress in this region is:

$$\sigma_\theta^II = \sigma_r^II - \bar{\sigma} \quad (6.26)$$

where the equivalent stress is determined by the equation (6.6).

The radial strain in this area is determined as follows:

$$\varepsilon_r^{\text{II}} = \ln \frac{r_0^{\text{II}}}{r} \quad (6.27)$$

in case of r between $r_p \sin \varphi < r \leq (r_p + \rho) \cos \alpha$

In equation (6.27), r_0^{II} is deduced from the geometry relation between r and other geometrical parameters that can be determined on the basis of the volume constancy condition and takes the following form in region II.

$$r_0^{\text{II}} = \sqrt{2} r_p \left\{ 1 - \sin \alpha + \frac{\rho}{r_p} \left[\left(1 + \frac{\rho}{r_p} \right) \left(\frac{\pi}{2} - \alpha - \beta \right) \cos \alpha + \left(\frac{\rho}{r_p} \right) (\sin \alpha - \cos \beta) \right] \right\}^{\frac{1}{2}} \quad (6.28)$$

where

$$\beta = \arcsin \left(\frac{(r_p + \rho) \cos \alpha - r}{\rho} \right) \quad (6.29)$$

In the equation (6.12), r_p is the normal radius of the end-contact point between the punch and sheet. This radius is varied depending on the punch travel during the forming process. This is also the main feature of the parabolic geometry.

It is clear that the the distribution of the strains and the stresses in this region depends on the counter pressure during the forming process. If the fluid pressure is too high, the height of the pre-bulging zone is also increased, which could lead to failure of the forming part. On the contrary, if the fluid pressure is not sufficient, it will lead to wrinkles on the sidewall area of the part.

6.3.3 Analysis of strain and stress in the punch head (Region III)

As shown in Fig. 6- 9, a shell element of sides $ds_1 = \rho_\varphi d\varphi$ and $ds_2 = r d\theta$ is also considered in order to establish the equilibrium equation. Due to the counter pressure there is a contact between the sheet metal and the punch head. The friction coefficient in this area is denoted by μ_3 and the correspondent friction force increment is denoted by dN . The fluid pressure p and the friction force on this element exert an inward and outward force along the surface normal, respectively:

$$dN - p dA \quad (6.30)$$

As computed in the previous section, the equilibrium equation in the direction normal to the surface and in the direction of the meridian tangent can be derived as follow:

$$\begin{aligned} p dA &= F_\theta \sin \varphi d\theta + F_r d\varphi + dN \\ \frac{dF_r}{d\varphi} d\varphi - F_\theta \cos \varphi d\theta &= 0 \end{aligned} \quad (6.31)$$

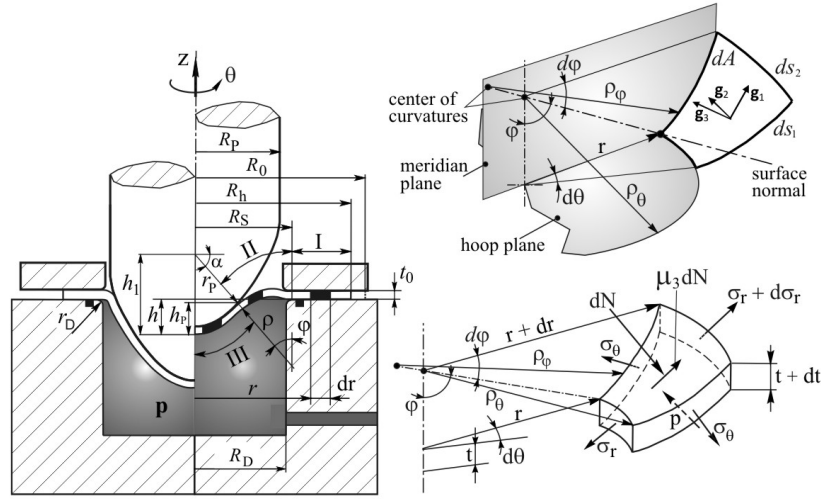


Fig. 6-9: Stresses on an element at the punch head

Substitute the geometry relations from (6.13) to (6.19) into the equation (6.31) we also get:

$$p = \left(\frac{\sigma_\theta}{\rho_\theta} + \frac{\sigma_r}{\rho_\phi} \right) t + \frac{dN}{\rho_\theta \rho_\phi \sin \phi d\phi d\theta} \quad (6.32)$$

$$r \frac{d(\sigma_r)}{dr} + \sigma_r - \frac{\rho_\phi}{\rho_\theta} \sigma_\theta = 0 \quad (6.33)$$

If the punch head is a part of a sphere i.e. $\rho_\phi = \rho_\theta$, then equation (6.33) becomes:

$$\frac{d\sigma_r}{dr} + \frac{1}{r} (\sigma_r - \sigma_\theta) = 0 \quad (6.34)$$

Similar to the solution procedure in region II, the radial stress σ_r in region III can be computed as follows:

$$\sigma_r^{III} = \sigma_r^{II} \left[r = r_p \sin \phi \right] + \int_r^{r_p \sin \phi} \frac{K(\epsilon_0 + \bar{\epsilon})^n}{r} dr \quad (6.35)$$

$$\sigma_\theta^{III} = \sigma_r^{III} - \bar{\sigma} \quad (6.36)$$

where the equivalent strain is determined by the equation (6.6). The radial strain in this area is determined as follows:

$$\epsilon_r^{III} = \ln \frac{r_0^{III}}{r} \quad (6.37)$$

for r is smaller than $r_p \sin \phi$

In equation (6.37), r_0^{III} is determined from the volume constancy condition in region III and is expressed as follows:

$$r_0^{III} = \sqrt{2r_p^2(1 - \cos \gamma)} \quad \text{where } \gamma = \sin^{-1}(r/r_p) \quad (6.38)$$

Equations (6.32), (6.34), (6.35) and (6.37) clearly indicate that both strain and stress states at the punch head area are significantly affected by the friction coefficient which is preserved by counter pressure during the HDD process. By solving these equations, the strain and stress distributions in this area can be obtained.

6.3.4 Algorithm and analytical result

In Fig. 6- 10 the developed algorithm for the computation of the strain distribution using analytical model is shown.

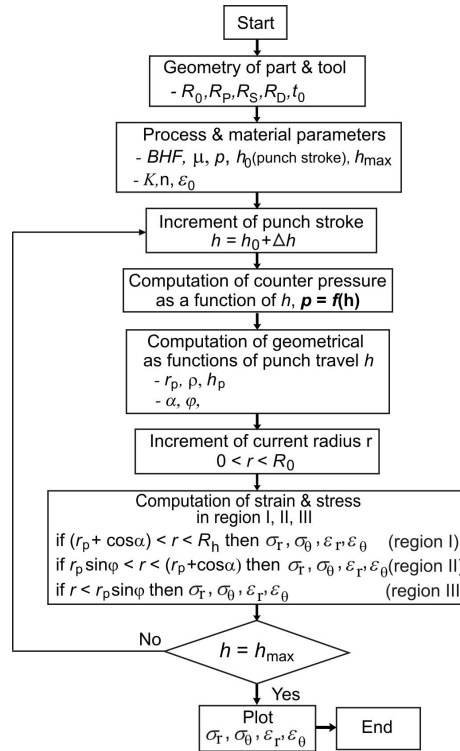


Fig. 6- 10: Algorithm for computation of strain distribution

Due to the complex geometry of the parabolic punch, the radius r_p at the contact point with the sheet metal varies during the forming process, Fig. 6- 11. Therefore, it is impossible to express explicitly the relation between r_p and other parameters. For the sake of simplicity, the

contact radius r_p is kept constant during the forming process. Thus, the form of the punch becomes a spherical geometry.

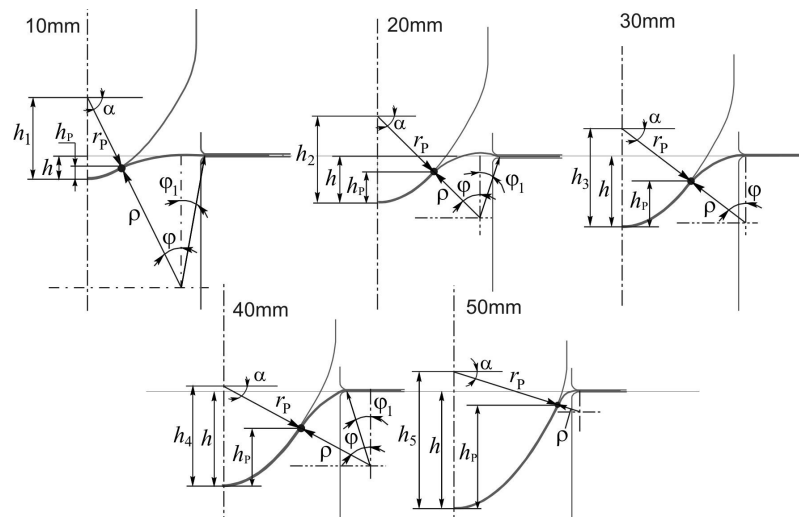


Fig. 6-11: Variation of r_p during HDD process in case of parabolic geometry

According to the algorithm in Fig. 6-10, the geometrical parameters of the forming tools such as radius of die ring R_D , punch geometry R_P , initial thickness of blank t_0 , initial blank radius R_0 must be given as the first step. As the next step, the process parameters F_{BHF} , friction coefficients μ_1, μ_2, μ_3 , maximal punch travel h , material parameters must also be given. The punch travel will be used as dependent parameter of this algorithm. The computation of the counter pressure p and the F_{BHF} as a function of the punch travel is subsequently calculated in the third step. In the fourth step, the necessary relations between the resulting angles α, φ and the geometrical parameters i.e. r_p, h_p are established and computed. By using the equations which have been established in the above sections from 6.2.1 to 6.2.3, the strain and stress distribution of the HDD process can be derived.

In this computation, the three different counter pressures p are proposed as shown in Fig. 6-12. The counter pressure of curve A is divided into three periods. The first one is correspondent to the first 10 mm of the punch travel. In this period, the fluid pressure p is increased from zero to 5 MPa. Afterward, it is kept constant until the punch travel reaches the value of 42 mm depth. In the last period, the counter pressure p sharply rises to a maximum value of 25 MPa and acts as calibration process in case of complex geometries.

For the curve B, the counter pressure p is gradually ascended from 0 MPa to 22 MPa. This curve is utilized to reduce the thinning of the sheet metal due to the increase of the fluid pressure during the whole process that will lead to an increase of the friction coefficient between the punch and the sheet metal.

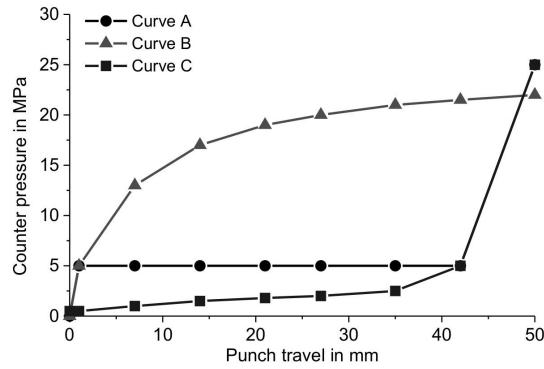


Fig. 6-12: Counter pressure depending on the punch travel

For the curve C, the fluid pressure p is gradually raised from 0 to 5 MPa when the punch descends from 0 till 40 mm. The fluid pressure p is rapidly increased to 20 MPa in the rest part of the punch travel to calibrate the part geometry. By utilizing this curve, the bulging effect is prevented. As a result, the more the fluid pressure p is increased, the better the sheet metal is pressed on the punch profile. The analytical results concerning the radial and the hoop strain compared to the correspondent numerical results are displayed in Fig. 6-13.

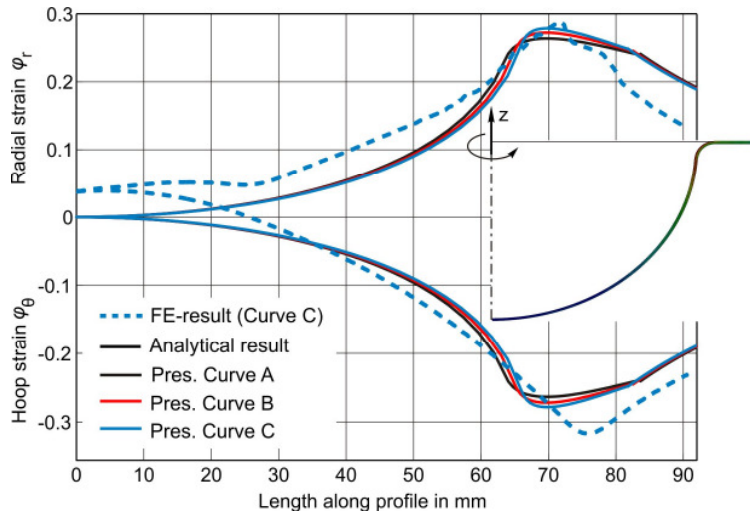


Fig. 6-13: Analytical results compared to the FE simulation

As can be seen, the analytical results are qualitatively in good accordance with the numerical reference results. The maximal deviation occurs at the center of the part due to the assumption that the thickness of the sheet remains constant. The resulting radial strain ϕ_r in both analytical

and FE results is either greater than zero or equal to zero. In contrast to that, the FE predicted hoop strain φ_θ in circumferential direction is greater than zero or smaller than zero or even equal to zero in the case of the plane strain. The analytically computed hoop strain φ_θ is smaller than zero. The analytical results have also qualitatively indicated that the strain level over the forming part is affected by the type of the counter pressure curve. The maximal strain level is obtained with the pressure curve C.

Obviously, the considerable advantage of the *MATLAB* developed tool is that the influences of the key process parameters on the strain states and the strain distribution can be rapidly evaluated. The computation time is less than 5 seconds. Furthermore, this can provide a useful guidance for predefining the process parameters and for optimizing the HDD process.

In order to observe the influences of the BHF on the strain distribution, the counter pressure p is kept constant while the BHF magnitude is changed. Then, the BHF is kept constant for the investigation of the influence of the counter pressure p . In Fig. 6- 14 and Fig. 6- 15, the strain distribution over the forming part affected by the BHF and the counter pressure p are shown.

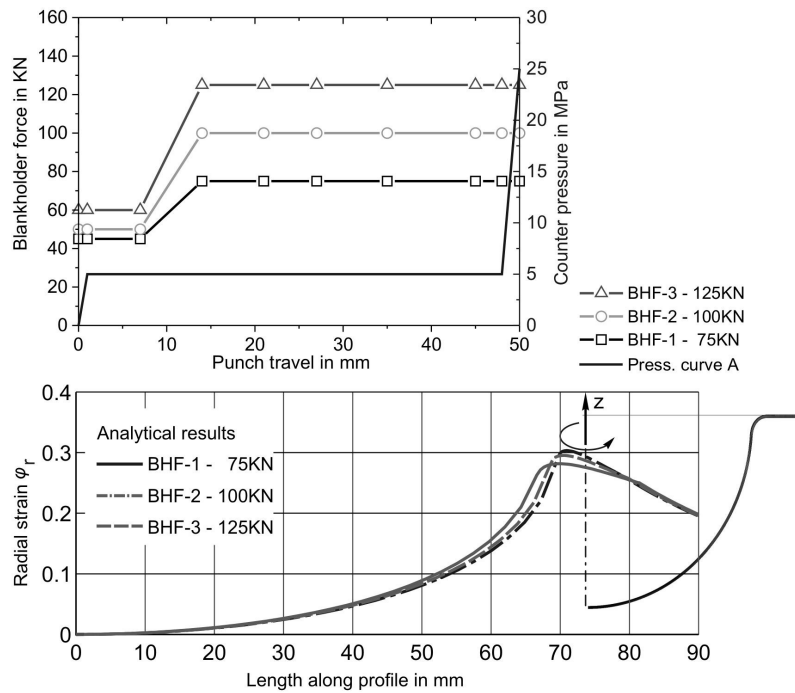


Fig. 6- 14: Strain distribution affected by the BHF obtained by analytical computation

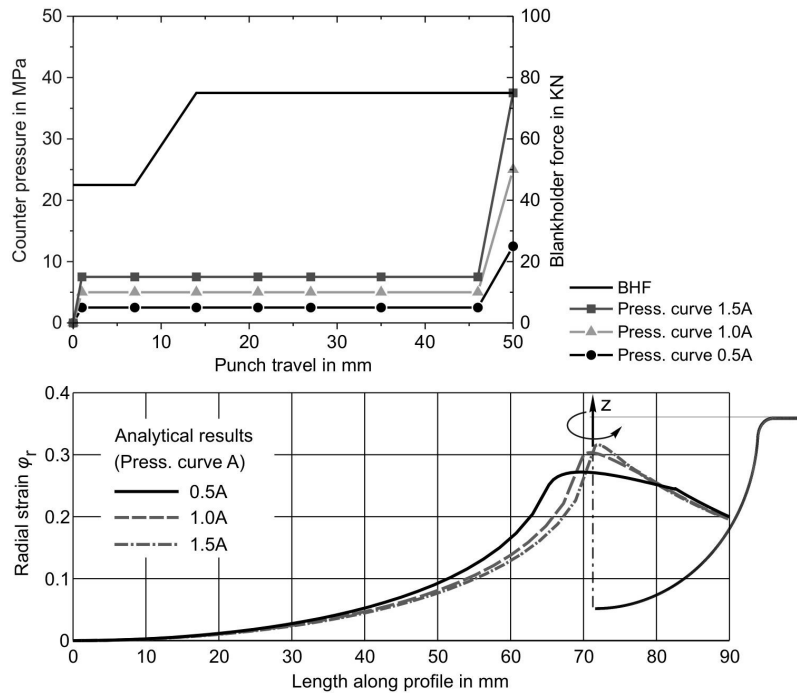


Fig. 6- 15: Strain distribution affected by the counter pressure obtained by analytical model

In Fig. 6- 14 and Fig. 6- 15, the computation using the pressure curve A is chosen for the illustration. The computation with the pressure curves B and C gives an indication of a similar tendency of the strain distributions. For ease of reference, the combination of the dependencies between the maximal radial strain in the unsupported area, the counter pressure p and the BHF during the HDD process is shown in Fig. 6- 16.

Obviously, the strain distributions are affected by both the BHF and the counter pressure p . Under the same counter pressure p , an increase of the BHF results in a slight moving down of the strain path in the unsupported area. As a result, the maximal radial strain in this area is decreased. In contrast to that, the strain path is shifted upward with increasing the counter pressure level, under the same BHF.

This resulting decrease of the radial strain in the unsupported area can be explained on the basis of the strain hardening property of the investigated material. Accordingly, the steel substrate becomes harder with increasing the BHF. This consequently leads to a decrease of the bulge height under the same counter pressure p . The bulge height can also be considered as a function of the material properties and the counter pressure p , *Khandeparkar (2007)*. As a result, the radial strain level is decreased by an increase of the BHF.

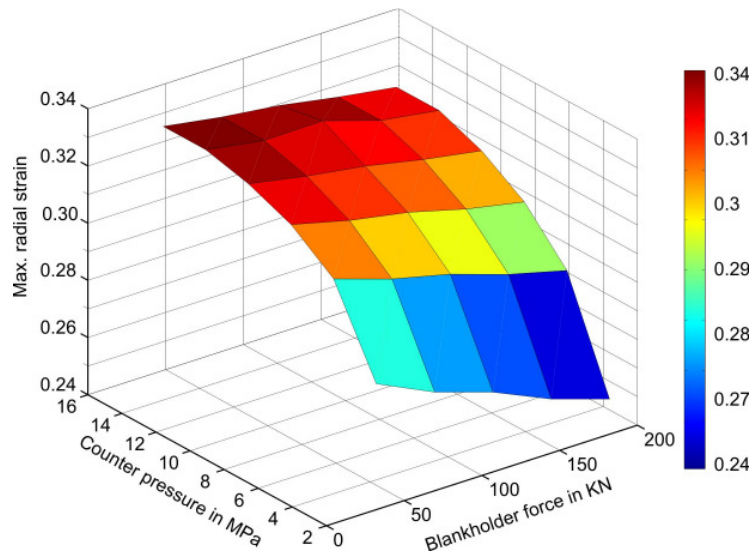


Fig. 6- 16: Relation between maximal radial strain in the unsupported area, counter pressure and BHF

As investigated in Chapter 4, the change of the surface properties significantly depends on the strain states and the strain level of the forming parts. The stretch forming and the plane strain state, which correspond to the strain ratio $\beta \geq 0$, will provide the lowest gloss reduction and roughness. Additionally, the low strain level will result in a low gloss reduction and roughness. The analytical results also give an indication that the radial strain is always greater than zero, whereas the hoop strain is either lower than zero or even equal to zero depending on the position of the part. This qualitative observation is a basic underlying know-how for the determination of the process parameters of the HDD process that can fulfill the desired surface quality.

Accordingly, the selection of the process parameters, such as the counter pressure p and the BHF, has to satisfy the two requirements as follows:

1. Maximal width of the tensile region, $\beta \geq 0$
2. Low strain level

However, both requirements lead to a conflict of goals. The first requirement could only be achieved, if the compressive strain φ_0 is minimized. The compressive strains $\varphi_t = \ln(x/x_0) < 0$ could only be minimized if the radial strain φ_r is increased on the sidewall of the part so that the material point x_0 remains in its radial position, i.e. the point P_1 (see Fig. 6- 17). An increase of the radial strain φ_r results in a higher equivalent strain or a higher strain level, in other words. As a result, this leads to the dissatisfaction of the second requirements.

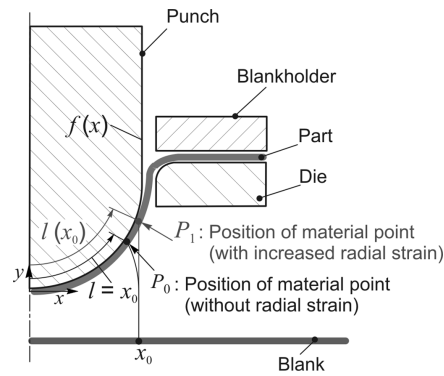


Fig. 6-17: Material point in case of without and with radial strain

According to the previous investigations, the gloss reduction is affected by both the strain ratio and the level of effective strain. Therefore, the applied BHF should be as high as possible to increase radial strain, whereas the counter pressure should be as low as possible.

6.4 Investigation of HDD process by FEA and experiments

In this section, the developed simulation strategy as shown in chapter five is continuously applied to the HDD process. Furthermore, the influences of the counter pressure p and the BHF on the strain distribution of the forming part are numerically investigated by combining with the analytically obtained conclusions. The numerical results are validated by the experiments. The gloss reduction depending on the strain distribution and the strain level is also evaluated. On this basis, the optimal process parameters, such as the suitable type of the pressure curve, the counter pressure level and the BHF, that result in the lowest gloss reduction are drawn out.

6.4.1 Simulation set-up

The HDD process is computed by using *Abaqus* finite element code that allows a combination of both the steel substrate and the coating layer in only one FE model. The numerical model is depicted in Fig. 6-18.

Only a quarter of the construction was modeled due to the axisymmetrical property. The thickness of the steel substrate was discretized in four layers of an hexahedral solid element. For the coating layer, four layers of the Herrmann formulation element were employed. The perfect adhesion force at the interface between the steel substrate and the coating layer was assumed. Contact assuming Coulomb friction between the blank and the punch, the blank - die surface, and the blank - blank holder was modeled. Friction between the blank and the die surface is denoted by μ_1 , between the blank and the surface of the blank holder is denoted by μ_2 . These values are very low since the counter pressure increases with the punch travel and the blank is lifted off the die surface.

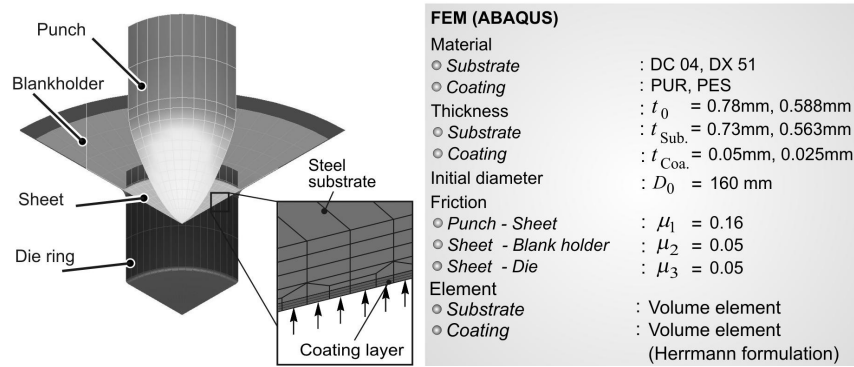


Fig. 6- 18: FE model for the HDD process with OCSM

In the HDD process, the hydro-dynamic lubrication condition is created between blank and die radius due to the influence of the fluid pressure. According to *Meuthen & Jandel (2005)*, the friction coefficient between organic coating and steel tools is smaller than 0.05 if a highly volatile oil is used as lubricating material. The last investigations at the IUL, which were carried out by *Kleiner et al. (2002)*, also proved that the friction coefficient of organic coated material is lower than 0.05. For this reason, the values μ_1 and μ_2 were assumed to be 0.02. Since the punch is not lubricated in the experiment in order to sufficiently attain the friction increasing effect, the friction between the punch and the blank, denoted by μ_3 , is much higher than μ_1 and μ_2 and assumed to be 0.16. Symmetrical boundary conditions are specified on the appropriate edge of the blank. The fluid pressure was modeled as a distributed pressure that depends on the punch travel. Hence, the simulated and experimental conditions are considered to be approximately similar.

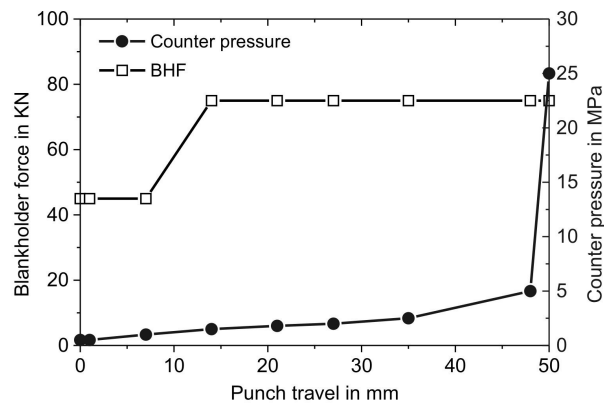


Fig. 6- 19: Fluid counter pressure and blank holder force

The fluid pressure curve and the correspondent BHF depending on the punch travel are illustrated in Fig. 6- 19. In this computation, the pressure curve C and the BHF curve 1 was chosen.

6.4.2 FE results and validations

The hydro-mechanical deep drawing tests were carried out on a modern CNC-programmable hydraulic press of the *Schuler Hydrap Company* in order to validate the obtained FE results. Consequently, the optical measured systems *Argus* and *Atos* were utilized to evaluate not only the strains but also the geometrical accuracy of the forming part.

Concerning the geometrical accuracy, cross sections were cut off from the parabolic reflector parts in order to compare the forming stages obtained by FE simulation and experiment. This comparison is shown in Fig. 6- 20.

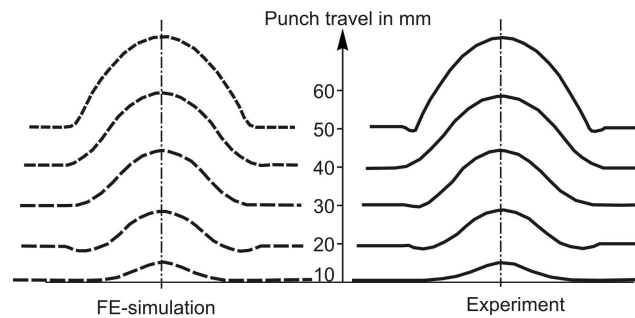


Fig. 6- 20: Comparison of the forming stages between FE simulation and experiment

Clearly, the forming stages obtained by FE simulation are in good agreement with the experimental results. It is seen that the pre-bulging effect was observed at the first period of the punch travel which is correspondent to 10 mm depth. Both FE and experimental results indicate that the bulging height attained the maximum value at a punch travel of 20 mm depth. When the punch reaches the value of 30 mm depth, this effect still exists, but the height of the bulging is significantly reduced. At the end of the HDD process, a slight deviation between the numerical and experimental result was observed. The experimentations have shown the existence of a small bulge on account of high counter pressure during the calibration phase. In contrast to that, no significant bulge effect is observed with the FE results.

Concerning the strain distributions, Fig. 6- 21 and Fig. 6- 22 show the numerically predicted and experimental radial and hoop strains along the profile of the forming parts. As can be seen, the numerical predictions of the radial and hoop strain are in good accordance with the experimentally determined results. The largest deviation was observed at the flange area of the forming part and was lower than 5 %. The reason is that the outer flange area appears slightly wrinkled while no wrinkle is observed with the FE results. The measured results also take into account this area and, thus, lead to this deviation.

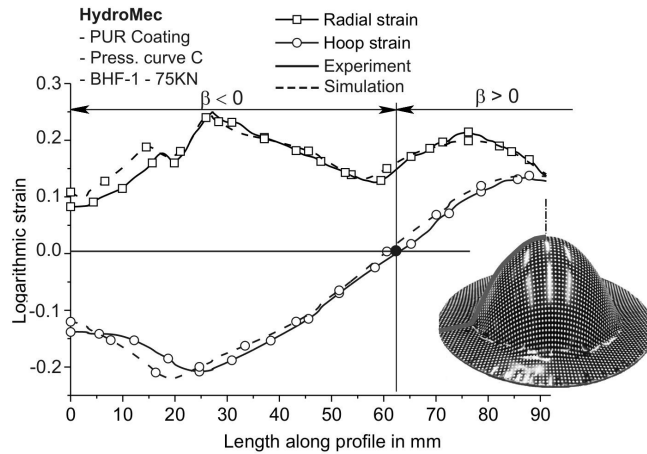


Fig. 6- 21: Comparison of strain distributions between simulation and experiment – PUR

The obtained strain distributions represent two strain states, namely tensile strain and tensile-compressive strain. The dividing line between these two is observed at the position where the tangential hoop strain is equal to zero, which corresponds to the 60 mm of the length along the part profile. During the HDD process, the counter pressure p pushes the OCSM against the punch face. This results in an increase of the frictional force between the blank and the punch surface. Hence, the relative movement of the blank with respect to the punch is restricted. As a result, a higher radial stresses can be transferred to the drawing zone from the punch head, *Khandeparkar (2007)*. The increased radial stresses will lead to higher radial strains. Due to the characterization of the parabolic geometry, the flange and the unsupported area are relatively large. As a result, this causes larger compressive stresses and in turn higher hoop strains, *Khandeparkar (2007)*.

In the case of the PES coating layer, the numerically predicted strains are in quite good agreement with the conducted experimentations, as shown in Fig. 6- 22. The thinning obtained with the FE simulation reaches a value of 35 % while tearing occurs around the top and the side wall of the forming part during experimentation. All the conducted experiments give evidence that the forming window of the PES coated sheet metal is very small. The upper limit of the BHF in this case is 75 KN. Tearing does not occur when the BHF gradually decreases, but wrinkles are observed in the circumferential direction.

Obviously, it is impossible to identify the forming window of the PES coated sheet metal in the HDD process due to the low formability of the steel substrate. The steel substrate DX51 of the PES coating is susceptible to strain ageing. The strain ageing has the effect of increasing the initial yielding stress to the upper yield stress. Beyond this, the yielding occurs in a discontinuous form and can be clearly seen in the tensile test as the so called Lüder's line. The amount of discontinuous strain is called the yield point elongation (YPE). For the steels that

have a significant YPE, more than 1 %, are normally unsuitable for forming due to non-smooth deformation and visible markings on the forming part, *Marciniak & Duncan (1991)*.

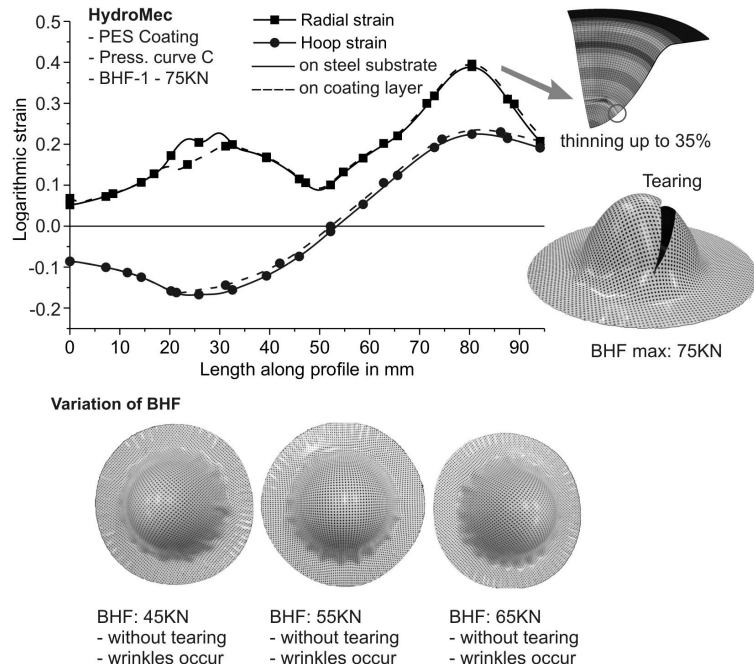


Fig. 6- 22: Comparison of strain distributions between simulation and experiment – PES

In Fig. 6- 23, the comparison of the thickness variations between the FE and the experiment results of the PUR coated parabolic reflector is shown. The FE predicted thickness varies along the profile of the parabolic part in the same manner as in the experimental one. The thickness variations are relatively homogenous. It can be seen that the sheet metal is thickened in the flange region. Afterward, it decreases steadily and reaches the maximum at the area around the top of the parabolic part. The maximal thinning obtained by experimentation is approximately 24 % in comparison to 26.6 % of the simulation. At the top of the part, where the sheet is in contact with the punch nose at the beginning of the process, the thinning is significantly reduced and reaches a value of 20 % compared to the initial thickness. The FE results are nearly coincident with the experimental results at the sidewall area of the part. The larger deviation is partially located at the flange and the punch head area. At these positions, the obtained FE result is approximately 5 % higher than the experimental result.

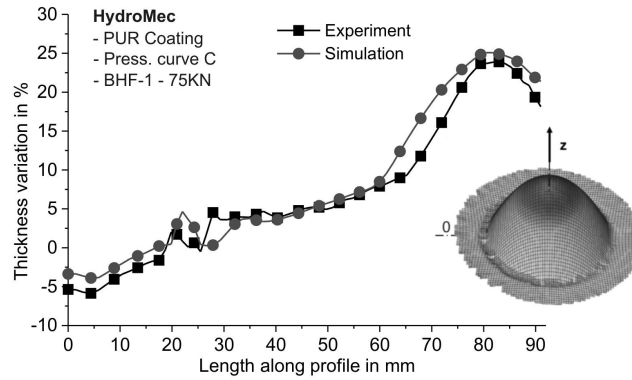


Fig. 6-23: Comparison of the thickness variation of the PUR coated reflector part

Clearly, all observations show that the numerically predicted strains are in good agreement with the experimentally determined results. By combining this with the given suggestions in the above section, the determination of the optimal process parameters that can provide the desired surface property is presented in the next section.

6.4.3 Influence of counter pressure on the strain distribution

In this section, the influences of the counter pressure p on the strain distribution, which determines the final surface quality of the reflector part, are investigated. The suitable pressure curve, which can provide the best surface quality in terms of gloss reduction and roughness degree, are determined.

The determination of the pressure curve is basically based on the given suggestion obtained by the analytical results in section 6.3.4. Accordingly, the maximal width of the tensile-strain region and the low strain level must be considered as evaluative criteria in order to assure low gloss reduction. As shown in the above section, the significantly strong point of the developed analytical model is that the strain distribution is rapidly computed. Nevertheless, the use of the analytical tool to determine the tensile-strain region is nearly impossible on account of the assumption of constant thickness. Therefore, the use of the verified FE strategy in combination with the analytical results for the determination of the process parameters is necessary.

In order to determine the type of the pressure curve that can satisfy both above requirements, three different pressure curves based on the proposed pressure curves in Fig. 2- 21 and Fig. 6- 12 are employed. The BHF in this case is kept constant as shown in Fig. 6- 24. These pressure curves characterize the different process strategies of hydro-mechanical deep drawing as indicated in the section 6.3.4. The preliminary investigations have shown that a too high pressure at the beginning of the punch travel strongly leads to pre-bulging effect, a reduced blank holder force are partly compensated by the load of the counter pressure onto the sealing area at the blank holder) and, consequently, causes the wrinkling of the deformed part.

Therefore, a relatively low pressure level is suggested at the beginning of the HDD process, Lange (1990).

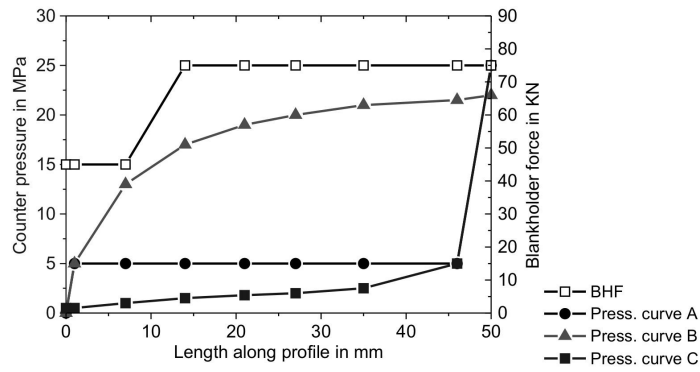


Fig. 6-24: Pressure curves depending on punch travel and BHF

Fig. 6-25 displays the strain distributions obtained by ABAQUS simulation depending on the fluid pressure curves in the case of PUR coating. The figure shows the counter pressure profile has a significant influence on the strain distribution of the reflector part. Taking into consideration the deformation modes in sheet metal forming, the strain distribution can be divided into two different zones, namely tensile–tensile strain (strain ratio $\beta > 0$) and tensile-compressive strain (strain ratio $\beta < 0$). The dividing point is located at the position where the tangential true strain equals zero. At this position, the strain state can be considered as plane strain (strain ratio $\beta = 0$).

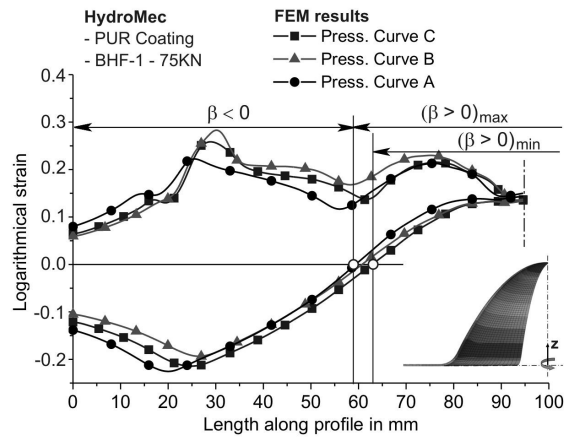


Fig. 6-25: Strain distributions depending on the counter pressure curve - PUR coating

The numerically predicted strain distributions have clearly indicated that the pressure curve A provides the broadest area of the positive strain ratio β compared to the other curves. The smallest tensile region occurs with the pressure curve C. Considering the strain level in critical areas, i.e. top and sidewall area of the part, the pressure curve A also provides a lower strain level compared to the one in case of the pressure curves B and C. This observation is also compatible with the analytical results as shown in Fig. 6- 13. As a result, the pressure curve A is chosen to meet the given need.

6.4.4 Influence of BHF on the strain distribution

For achieving a good balance between surface quality and geometrical accuracy, the HDD process must consist of optimal process parameters, *Finckenstein (1984)*. Therefore, the influences of the BHF on the strain distribution of the reflector part are further investigated in this section. Accordingly, the suitable BHF, which can provide the best strain state resulting in the lowest gloss reduction, are determined.

Similar to the determination of the counter pressure p , the optimal determined BHF also has to fulfill both criteria obtained by analytical results, i.e. maximal tensile-strain region and low strain level. To this end, the following procedure is proposed. The chosen pressure curve A is kept followed during the HDD in this case, whereas the correspondent BHF is changed with respect to the different magnitudes. By following the process, the maximally and minimally permissible BHF is defined. The proposed BHF curves are depicted in Fig. 6- 26. Depending on the characteristic of the pressure curve, the BHF curve is divided into two parts. At the beginning of the punch travel, a low value of the BHF is applied on account of low fluid pressure. Then, it gradually increases to a higher value. This value is kept constant till the end of the HDD process.

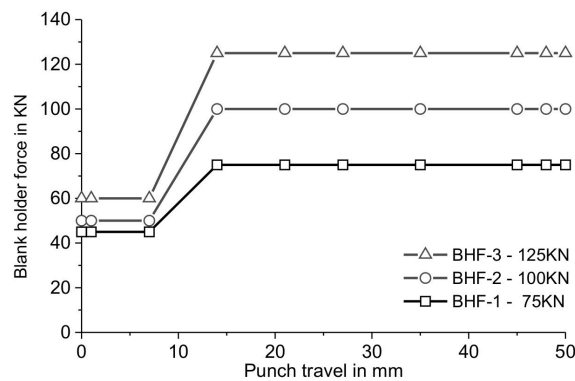


Fig. 6- 26: The investigated BHF curves

Fig. 6- 27 shows the numerically predicted strain distribution depending on the different BHF curves in case of PUR coating. As can be seen, the width of the tensile-strain region is considerably increased with increasing BHF. The more the BHF increases, the larger the tensile-strain region becomes. The obtained results give an indication that the highest BHF

curve 3 provides the largest width of the tensile region. The smallest one is obtained by the lowest permissible BHF that ensures the successful HDD process without any failures i.e. wrinkles or tearing.

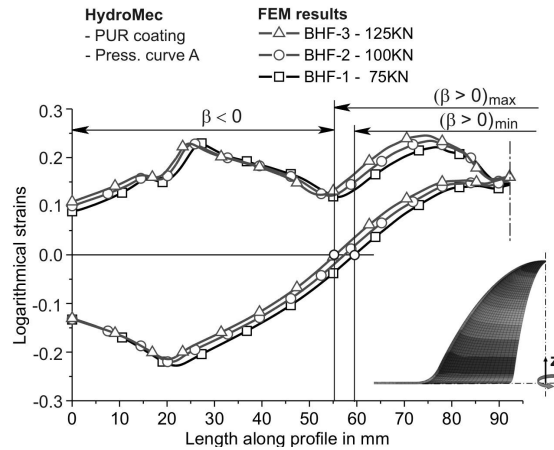


Fig. 6-27: Strain distributions depending on BHF - PUR coating

Based on the obtained results and the above analysis, the following combinations of the counter pressure p and the BHF curves are suggested in order get the best strain distribution that results in the lowest gloss reduction during the HDD process. The pressure curve A is chosen by taking into consideration the path of the counter pressure depending on the punch travel. By considering both criteria, i.e. maximal width of the tensile strain area and low strain level, the pressure curve A and the BHF curve 3 should be combined for the forming of PUR coated sheet metal. The suggestions are summarized in Table 6- 1 for ease of reference.

Table 6- 1: Combination of process parameters used in HDD process of OCSM

Investigated materials	Process parameters	Illustration
PUR coated sheet	- Pressure curve A - BHF-2 - BHF-3	

The numerical investigations have proven that the suggestions resulting from the analytical model can be applied for predefining the process parameters in the HDD process. In the next section, the HDD experiments are conducted in order to verify both analytical and numerical results and to evaluate the gloss reduction depending on the strain state and strain level.

6.5 Experimental validations

6.5.1 Validation of the influence of the counter pressure profile

The numerically predicted strain states have shown that the pressure profile A will contribute the best strain distribution that provides the largest tensile-tensile strain region and low strain level. As a result, the correspondingly obtained gloss reduction reaches the minimum value.

In order to validate these results, the HDD experiments are conducted using the PUR coated sheet metal. In these conducted experimentations, the BHF used is similar to the one as shown in the section 6.4.3. The validated procedure is similar to the one as shown in the above section. The computation using the pressure curve A has been validated in the section 6.4.3 as shown in Fig. 6- 21. For this reason, only computed and experimental results using pressure curve A and B need to be compared in this section.

In Fig. 6- 28 and Fig. 6- 29, the comparisons between the FE and the experimental results are displayed. As can be seen, the predicted strains are in good agreement with the experimentally determined strain distributions. It is seen that the width of the tensile deformation area obtained by the pressure profile B is significantly smaller than the others derived from the profile A. Clearly, the tensile-strain region obtained by the pressure curve B starts approximately at 63 mm of the length along the part profile compared to 59 mm in case of pressure curve A. In case of the pressure curve C, Fig. 6- 21, the smallest tensile-strain region is observed that corresponds to 62.5 mm of the length along profile.

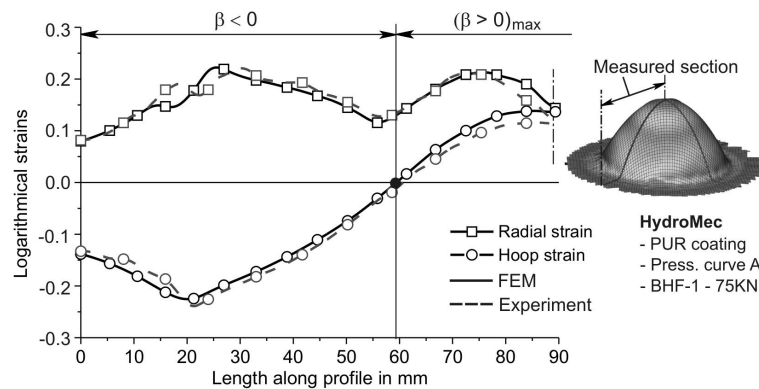


Fig. 6- 28: Comparison of the strain distribution obtained by pressure curve A

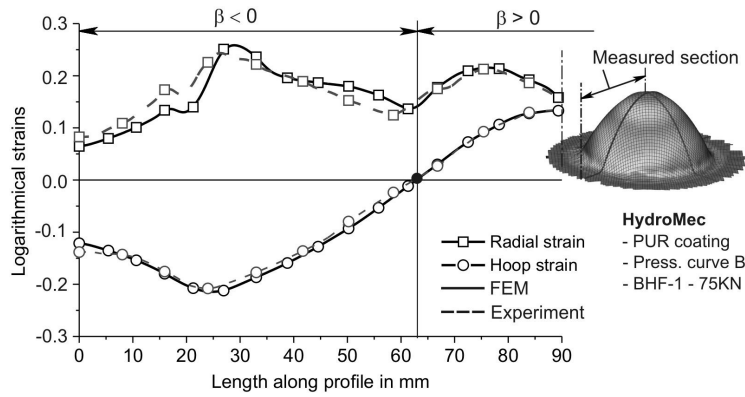


Fig. 6- 29: Comparison of the strain distribution obtained by pressure curve B

Clearly, the above observations show that the strain state and strain level are affected by the pressure path. However, the influences of using solely the suitable pressure are not large. In order to achieve the given requirements i.e. the maximal width of the tensile-strain region and low strain state, it is necessary to combine both the pressure curve and the BHF. The numerical influences of the BHF on the strain distribution are investigated in the above section. The following part shows the experimental validation of these investigations.

6.5.2 Validation of the influence of the BHF

In order to verify the influence of the BHF, the suggested pressure curve A is employed and kept followed during the investigation. The investigated BHF curves are variable as shown in Fig. 6- 26. The comparisons between the experimental and numerical results in the case of the computation with BHF-1 are illustrated in Fig. 6- 30. The radial, the hoop and the effective strain are chosen as the comparative parameters.

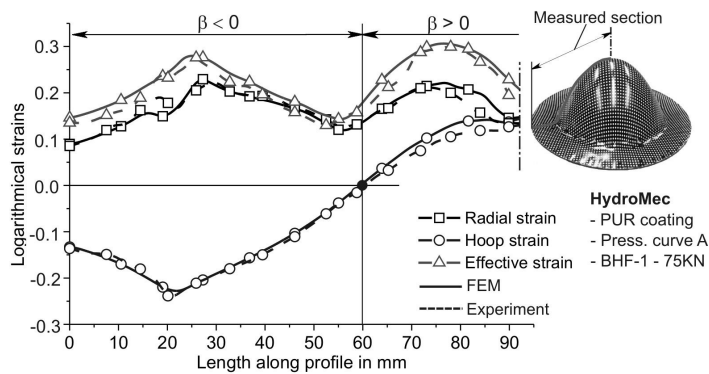


Fig. 6- 30: Comparison of strain distributions in the case of BHF-1

The comparisons of these parameters show that the numerical predictions are in good agreement with the experimentally determined results. The numerically predicted strain distributions give an indication of the slightly higher value than measured strains. The comparisons reveal the maximum deviation in the small area at the top of the part. Due to the complexity of the contact conditions between the punch head and the sheet metal under the influences of the counter pressure, this condition is only modeled using a constant friction coefficient during the HDD forming process. Hence, it leads to the deviation between both results. The deviation in this case is seen to be less than 4 %. For the BHF-1, the width of the tensile-strain region starts approximately at 60 mm of the length along the part profile.

The data in Fig. 6-31 and Fig. 6- 32 are the comparisons between the experimental measurements and the numerical strain predictions in the case of BHF-2 and BHF-3, respectively.

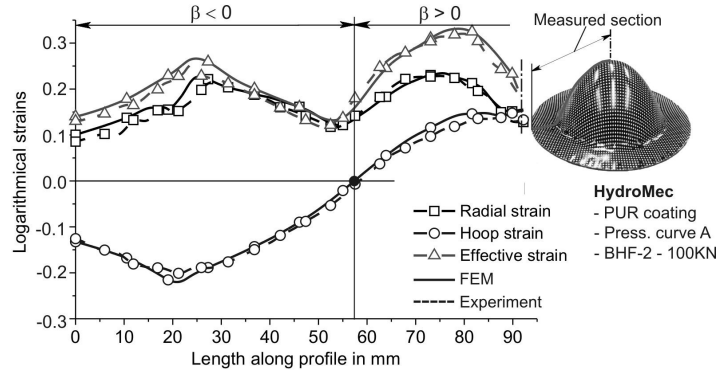


Fig. 6- 31: Comparison of the strain distributions in the case of BHF-2

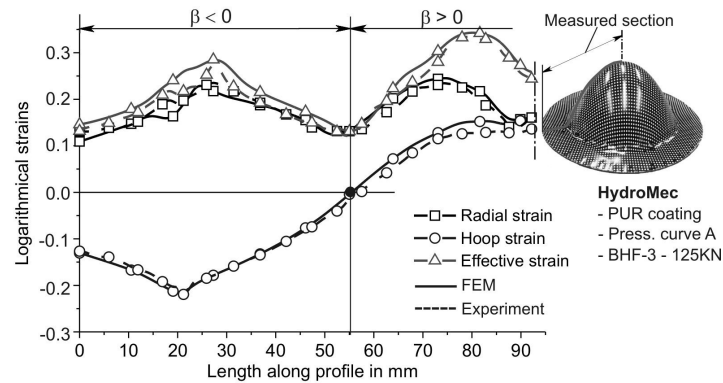


Fig. 6- 32: Comparison of the strain distributions in the case of BHF-3

Similar tendencies to the computation with BHF-1 are observed. The comparisons give an indication of only slight deviations between the numerical and experimental prediction.

Considering the width of the tensile-strain region, it is obvious that the lowest BHF-1 provides the smallest width of the tensile region. The resulting tensile-strain region in this case starts from the position of 60 mm of the length along the profile. For the BHF-2, this desired region becomes larger compared to the one of the BHF-1. The tensile-strain region in this case occurs at the position of 57.5 mm of the profile length. The BHF-3 results in the largest width of the tensile-tensile deformation region compared to the BHF-1 and BHF-2. The desired region in this case is observed at the position of 55 mm of the profile length.

Clearly, the width of the tensile-strain region is increased with increasing of the BHF under the same fluid pressure. The numerical and experimental results have proved the compatibility of the suggestion obtained by the analytical model. In the next section, the evaluations of the gloss reduction depending on the strain state and the strain level of the OCSM reflector part are presented.

6.5.3 Gloss reduction

According to the investigation in chapter four, the gloss reduction on the surface is significantly affected by the strain level and the strain states over the forming part. In this section, the gloss reductions affected by different process parameters i.e. BHF curves are evaluated in order to prove the above conclusions.

To this end, the HDD experimentations using the pressure curve A and different BHF curves are conducted. Two types of specimen, i.e. with and without grid pattern on the surface, are used. The specimens with grid pattern are used in order to measure the strain distributions after forming. The specimens without the grid pattern are employed in order to evaluate the change of the gloss property. The strain distribution is measured by means of an *Argus* optical apparatus. The change of the gloss degree is evaluated by using the reflector meter *NOVO-Curve*. It has to be noted that the accuracy of the gloss measurement on the curve surfaces strongly depends on the curvature radius of the surfaces. For this reason, the changes of the gloss property should only be evaluated at positions that can assure the accurate measurement.

The tested measurements have shown that the gloss degree of the region from the split point (tangential strain equal to zero) to the top of the part cannot be measured with acceptable accuracy on account of small and varied curvature radii. However, it can be predicted by using the obtained relation in chapter four. The gloss change in the tensile-compressive region was measured at four different points as shown in Fig. 6- 33. In the flange area, it is not necessary to consider the gloss reduction. Because of the geometrical complexity, it is necessary to design an extra stepped tooling system that can be mounted on the gloss measurement apparatus, Fig. 6- 33. By using this supplementary tool, it can be assured that the evaluated area and also the measured points are located at identical positions on the different parts. This plays an important role in the comparison of the measured results.

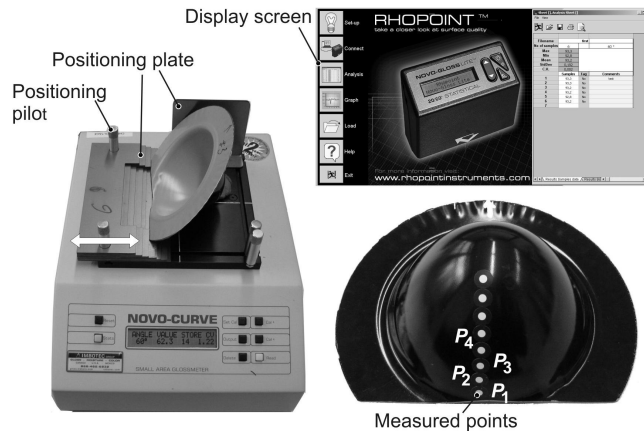


Fig. 6- 33: Measured tooling system and the specimen for measurement of gloss reduction

The measured points in the tensile-compressive region are numbered by P_i ($i = 1 \div 4$). For ease of comparison, the effective strains and hoop strains corresponding to the computation with BHF-1, BHF-2 and BHF-3 are taken into account. In Fig. 6- 34, the resulting equivalent strains, hoop strains and the position of the measured points are depicted.

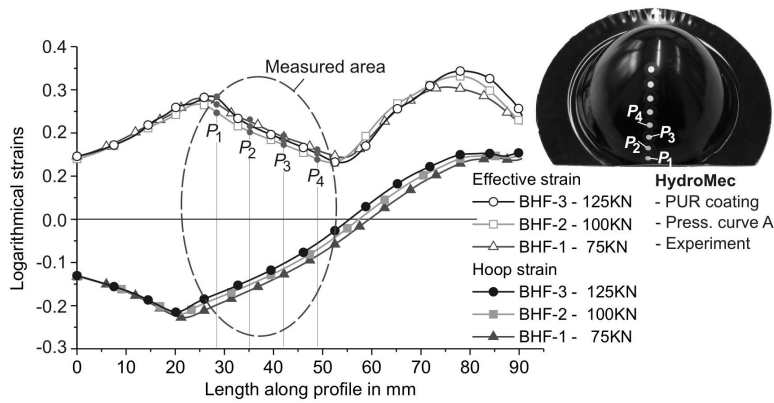


Fig. 6- 34: Effective strains and points for gloss measurement

In Fig. 6- 35, the obtained gloss reduction of the different points in the tensile-compressive strain region of the PUR coated reflector part are depicted.

As can be seen, the maximal loss of gloss occurs at the measured point P_1 that keeps the highest effective strain. The lowest gloss reduction is observed at the point P_4 that shows a significantly lower equivalent strain. However, the reductions of the gloss degree are not

large. In case of the BHF-1 for example, the deviation between the maximal and minimal gloss reduction reaches a value of 2.71 %. In the case of the BHF-2 and BHF-3, the correspondent deviations are in turn 1.52 % and 1.94 %. Taking into consideration the strain level, the BHF-1 results in a higher effective strain level as compared to the BHF- 2 and BHF-3. As a result, the BHF-1 leads to the highest gloss reduction. The lowest reduction of gloss degree occurs with the BHF-2.

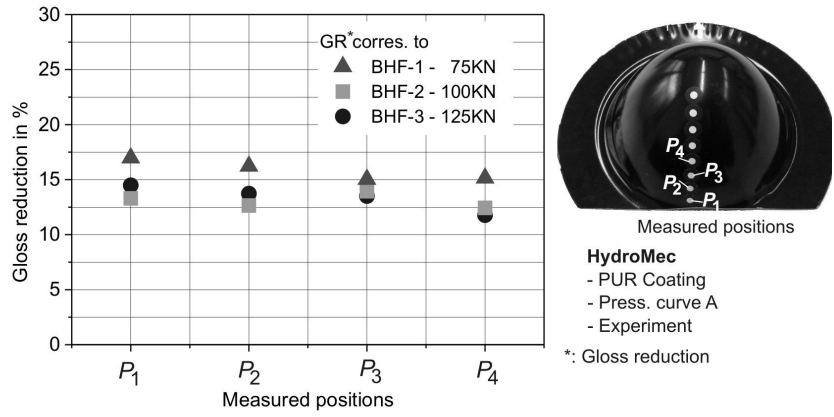


Fig. 6- 35: Gloss reduction on the surface of the reflector part

In summary, the evaluations of the gloss reduction after the HDD process give an indication of a good compatibility between the analytical and numerical results. The suggestions obtained by analytically developed tools can successfully be used to determine the optimal process parameters concerning the optical property of the HDD process using OCSM.

6.6 Conclusion

The HDD technique is suitable for the forming of the OCSM parabolic reflector part because of many advantages compared to the conventional forming technique. The conducted investigations have shown that the PUR coated parabolic reflector can be formed without any wrinkle at the sidewall area on account of a good formability of the DC04 steel substrate. In contrast to this, the PES coated sheet metal cannot be successfully formed due to low formability.

An algorithm and a MATLAB program based on the extension and adaptation of *Lo's* analytical model are developed. The developed program allows the computation of the strain distributions over the forming part. The significant advantage of this developed program is that the strain distributions and the influence of process parameters can be rapidly computed, within only 5 seconds. It is helpful to use this model to deeply comprehend and recognize the influences of process parameters such as BHF and counter pressure on the contributed strain path. Furthermore, useful suggestions based on analytical results have been drawn. These support a good guidance for carrying out the numerical investigation and optimization of the

process parameters. The validations of the analytical model and the FE simulation give an indication of a good compatibility between the analytical and numerical results. The obtained guidance can be used for the determination and optimization of the process parameters such as BHF and counter pressure. It is seen that the desired tensile strain region can be extended by combining the counter pressure and the BHF. As a result, the pressure curve type A and the BHF-2 or BHF-3 should be used as optimal process parameters to provide the largest biaxial tensile region.

7 Conclusions and future developments

In this research, important fundamentals on the processing of organically coated sheet metals (OCSM) by forming technology have been contributed. These fundamentals comprise the forming behavior of OCSM with special regard to forming limits, the change of optical properties during forming and the prediction of these effects by suitable failure criteria, gloss reduction diagrams (GRD) as well as numerical modeling (FEM). As OCSM, a polyurethane-based coating (PUR) and a polyester-based (PES) coating have been investigated.

Due to the effect that the coating layer and the substrate material feature different mechanical behaviors (e.g. formability), special forming limit diagrams of the coating layer (FLDC) of the OCSM was first established. In case of PUR and - under special strain condition – in case of PES, the failure of the coating occurs prior the substrate material. Hence, FLDC should be used instead of the forming limit diagrams of the substrate (FLD) in order to evaluate the formability concerning cracking of the coating layer due to excessive strains.

Regarding the optical properties, material-specific GRD have been determined in order to predict the reduction of coating gloss as a result of the forming process. It is found that the gloss reduction of the coated surface is caused by the strain states and the increase of deformation of both steel substrate and coating layer. The gloss reduction is increased with increasing of the deformation level characterized by the equivalent strain. Furthermore, the strain ratio has a major influence on the gloss reduction. It can be proved that gloss reduction increases significantly in case of negative strain ratios which is characteristic of deep drawing modes (compression-tension mode). Furthermore, the total thickness and the coating thickness also have considerable influences on the loss of gloss. The obtained relations can be summarized in GRD that can be used as the process window of the forming process of OCSM. Hence, GRD can be applied in conjunction with FEM to predict the change of the optical property of OCSM products after industrial forming processes.

In the frame of this research, the modeling and simulation of the forming process with OCSM by FEM is based on a detailed modeling of the coating layer instead of a simplified modeling (neglecting the coating layer) which is described in the literature. Related to the laboratory tests such as hydraulic bulge test, cylindrical and square cup deep drawing test, the developed FE model has shown the good applicability of the proposed modeling strategy. The numerical results are close to the experimental ones. Furthermore, it can be proved that a detailed modeling of the coating layer is more precise in the part areas that undergo bending. This is due to the more realistic modeling of the blank thickness and mechanical properties.

In order to prove the applicability of these findings, a parabolic reflector as praxis-oriented part geometry has been formed using OCSM. Since the parabolic reflector has a conical shape, hydro mechanical deep drawing (HDD) was applied. The HDD technique was investigated by an analytical model. This model, initially established by *Lo et al. (1993)*, was extended, adapted to parabolic part geometries and utilized as a *MATLAB* program for the computation of strain distributions in HDD processes. The considerable advantages of this developed program is that the strain distributions and the influence of process parameters such as BHF and counter pressure can be rapidly computed, within only 5 seconds. Hence, a

comprehensive screening of process parameters including interactions becomes possible for a deep understanding of the process and about measures of process optimization. For instance, a counter pressure curve with a low pressure level at the beginning of the process and maximum calibration pressure at the end of the process ensure the geometrical accuracy of the parabolic part. Using this curve as a basis, the BHF curves could be optimized regarding the optical part properties. In detail, the blank holder forces should be increased in order to increase the radial strains in the side wall of the part. Higher radial strains reduced compressive strains and - according to the fundamental findings - the gloss reduction. On the other hand, a high BHF lead to increased strain hardening limiting extensive radial strains in the unsupported area. Using this parameter setting, the parabolic reflector with limited gloss reduction could be successfully produced by HDD.

Future development

The prediction of the coating failures, i.e. cracking, is based on the imposed strains on the steel substrate and the coating layer. As mentioned above, the differences of the mechanical behaviors of the steel substrate and the coating layer, when these materials are in large deformation, and the non-uniformity imposed strains are also the cause of additional residual stresses in the coating layer. These stresses lead to additional coating failures in further processing. Thus, the development of an approach to predict the coating damage based on the residual stresses on both the steel substrate and the coating layer is also crucial.

Regarding these conclusions, the following aspects still need further investigation

- Investigation of the overall influence of the strain path and deformation level on the substrate surface (roughness evolution).
- Development of a general approach for the prediction of coating damage based on imposed stresses on the metal substrate and the organic coating layer.

References

- Alberti, N.; Fratini, L. (2004):* 'Innovative sheet metal forming processes: numerical simulations and experimental tests', *Journal of Materials Processing Technology* 150, pp. 2-9.
- Abaqus (2007):* Abaqus Analysis User's Manual, Version 6.7.
- Arcelor (2004):* ARCELOR Group: Organic coated steel, User's manual.
- Ahmetoglu, M.; Hua, J.; Kulukuru, S.; Altan, T. (2004):* 'Hydro-forming of sheet metal using a viscous pressure medium', *Journal of Materials Processing Technology* 46, pp. 97-107.
- Aust, M. (2003):* 'Hydromechanische Tiefziehen von Karosserieteilen', Dr.-Ing. Dissertation, Universität Stuttgart.
- Azodi, H.D.; Moslemi Naeini, H.; Parsa, M.H.; Liaghat, G.H. (2008):* 'Analysis of Rupture Instability in Hydro-mechanical Deep Drawing of Cylindrical Cups', *Int. J. Adv. Manuf. Technol.*, Vol. 39, No. 7-8, pp. 734-743.
- Bach, Fr.-W.; Behrens, B.-A.; Rodman, M.; Roßberg, A.; Vogt, O.; Huinink, T. (2006):* 'Werkstoff-und verfahrenstechnische Entwicklung von wirkmedienbasierten Umformprozessen für Magnesiumbleche', Abschlussbericht zum DFG-Schwerpunktprogramm SPP 1098, pp. 115-137.
- Bakhshi-Jouybari, M.; Hosseinipour, S.J.; Gorji, A.; Shamsi, A.; Zahedi, S.A. (2009):* 'Theoretical study and Finite element simulation of Tearing in Hydro-forming process', *Journal of Applied Sciences* 9, pp. 178-182.
- Bastos, A.C.; Ostwald, C.; Engl, L.; Grundmeier, G.; Simoes, A.M. (2004):* 'Formability of organic coatings - an electrochemical approach', *Electrochimica Acta* 49, pp. 3947-3955.
- Behrens, B. A.; Deiler, G.; Hübner, S.; Milch, M. (2005):* 'Trockenumformung organisch beschichteter Feinbleche', 5. Forum, Tribologische Entwicklungen in der Blechumformung, Darmstadt.
- Behrens, B.-A.; Deiler, G.; Yun, J.-W. (2004):* 'Endlackiertes Feinblech qualitätsgerecht umformen', *Blech Inform* 2, Special Fahrzeugproduktion, pp. 27-29.
- Bernspangb, L.; Hammam, T. (1993):* 'Verification of an explicit finite -element code for the simulation of the press forming of rectangular boxes of coated sheet steels', *Journal of Materials Processing Technology*. Vol. 39, No. 3-4, pp. 431-453.
- Bjerke'n, C. Kao-Walter, S.; Stahle, P. (2006):* 'Fracture mechanism of a thin elastic plastic laminate', *Proceeding of the 16th European Conference on Fracture*, Alexandroupolis, Greece, pp. 927-929.
- Bletzinger, K.-U. (2005):* 'Theory of shells', Vorlesung, Lehrstuhl für Statik, Technische Universität München.

- Boelen, B.; Den Hartog, H.; Van der Weijde, H. (2004): 'Product performance of polymer coated packing steel, study of the mechanism of defect growth in cans', *Progress in organic coatings* 50, pp. 40-46.
- Bortot, P.; Ceretti, E.; Fiorentino, A.; Giardini, C. (2007): 'Hydro-mechanical Deep Drawing of funerary vases: a suitable alternative to the traditional forming process', *Key Engineering Materials*, Vol. 44, pp. 485-492.
- Bräunlich, H.; Neugebauer, R.; Wolfhard, M.; Alsmann, M. (1998): 'Umformverhalten von bandbeschichteten Stahlfeinblechen', Vortrag zum Stahlkolleg, Studiengesellschaft Stahlanwendung e.V., Düsseldorf, Tagungsband 721, 26 pp.
- Bragallini, G.M.; Cavatorta, M.P.; Sainsot, P. (2003): 'Coated contacts: a strain approach', *Tribology International* 36, pp. 935-941.
- Bruder-Stroisznigg, M.; Wallner, G. M.; Strauß, B. (2004): Deformationsverhalten und Erscheinungsbild von bandbeschichteten Stahlblechen für Automobilanwendungen, *BHM* 149, Heft 9, pp. 313-317.
- Bürk, E. (1963): 'Das hydromechanische Ziehverfahren', *Blech*, Vol. 9, pp. 573-578.
- Carlsson, P. (2005): 'Surface engineering in sheet metal forming', PhD-Thesis, Uppsala University, Sweden.
- Chandra, S.; Prathap, G. (1989): 'A field-consistent formulation for the eight-node solid finite element', *Computers and Structures* 33, pp. 345-355.
- Chang, T.; Sproat, E. A.; Lai, Y. H.; Shephard, N. E.; Dillard, D.A. (1997): 'A test method for accelerated humidity conditioning and estimation of adhesive bond durability', *J. Adhes.* 60, pp. 153-162.
- Choi, H.; Muammer, K.; Ni, J. (2007): 'A study on the analytical modeling for warm hydro-mechanical deep drawing of lightweight materials', *Int. J. Mach. Tools & Manufacture* 47, pp. 1752-1766.
- Ceretti, E.; Giardini, C.; Contri, C.; Bortot, P. (2005): 'Hydro-mechanical deep drawing simulations: Model development and process parameters investigation', *Advanced Materials Research*, Vol. 6-8, pp. 353-360.
- Celeghini, M. (2001): 'Verfahren zur Wirkmedienbasierte Umformung von Blechwerkstücken und Verwendung eines Wirkmediums bei diesem Verfahren', European Patent EP 1270106 A1, Int. C1.7 B21 D26/02, C09K 3/12, Erlangen.
- colofer (2008): 'Die Verarbeitung', Markplanung und Entwicklung, Unternehmensbereich Kaltband/Veredelung – Organisch beschichtetes Stahlband, COLOFER[®], voestalpine GmbH.
- Dariani, B.M.; Fazli, A. (2006): 'Theoretical and experimental analysis of the axisymmetric hydro-mechanical deep drawing process', *Pro. IMechE*. Vol. 220, Part B: J. Engineering Manufacture, pp. 1429-1437.

- Deflorian, F.; Fedrizzi, L.; Rossi, S. (2000):* 'Effects of mechanical deformation on the protection properties of coil coating products', *Corrosion Science* 42, pp. 1283-1301.
- Dong, Y. (2002):* 'Effects of material properties and numerical simulation on thermoforming acrylic sheets', Master Thesis, The University of Auckland, New Zealand.
- Doerge, E.; Behrens, B.-A. (2007):* 'Handbuch Umformtechnik: Grundlagen, Technologie, Maschinen', Springer-Verlag, Berlin, ISBN-10 3-540-23441-1.
- DIN EN ISO 2813 (1999):* Beschichtungsstoffe: Bestimmung des Reflektometerwertes von Beschichtungen unter 20°, 60° und 85°, Beuth-Verlag, Berlin.
- DIN ISO 3668 (1996):* Lacke und Anstrichstoffe: Visueller Vergleich der Farbe von Beschichtungsstoffen (Farbabmusterung), Beuth-Verlag, Berlin.
- DIN ISO 4628 (1997):* Beschichtungsstoffe: Beurteilung von Beschichtungsschäden, Beuth-Verlag, Berlin.
- Eisenhour, T.A. (2007):* 'Experimental and numerical investigation of the bending characteristics of laminated steel', PhD-Thesis, Graduate Program in Aerospace and Mechanical Engineering, Notre Dame, Indiana.
- Fischer, F.; Klein, F. (1971):* 'Verformbarkeit organisch beschichteter Bänder', Deutsche Forschungsgesellschaft für Blechbearbeitung und Oberflächenbehandlung e.V. 3/71, pp. 61-63.
- Finkenstein, E. V. (1984):* 'Verbesserung der Form- und Maßgenauigkeit beim hydromechanischen Tiefziehen', *Z. Werkstatttechnik-Zeitung für industrielle Fertigung* 74, pp. 656-662.
- Finkenstein, E. V.; Brox, H. (1987):* 'Untersuchung metallisch-beschichteter Feinbleche unter technischen Umformbeanspruchungen', *Z. Werkstofftech.* 18, pp. 212-217.
- Friebe, H.; Galanulis, K.; Erne, O.; Müller, E. (2006):* 'FLC determination and forming analysis by optical measurement system', *Proceeding of the FLC-Zurich, ETH Zurich Switzerland*, pp.74-81.
- Gay, C. (2000):* 'Does stretching affect adhesion?', *International Journal of Adhesion* 20, pp. 387-393.
- Garcia-Garino, C.; Gabaldon, F.; Goicolea, J.M. (2006):* 'Finite element simulation of the simple tension test in metals', *Finite Elements in Analysis and Design* 42, pp. 1187-1197.
- Groche, P.; Schäfer, R. (2004):* 'Simulation der geometrischen Oberflächenwandlung beim Drücken optischer Bauteile', *Mat.-wiss. u. Werkstofftech.* 35, No. 7, pp. 454-460.
- Groche, P.; Huber, R.; Dörr, J. (2002):* 'Hydro-mechanical deep drawing of aluminum alloys at elevated temperature', *Annals of the CIRP*, Vol. 51, No. 1, pp. 215-218.
- Groche, P.; Klöpsch, C.; Huber, R. (2005):* 'Erweiterung der Verfahrensgrenzen beim hydromechanischen Tiefziehen von Aluminiumknetlegierungen durch thermische Unterstützung', In: Kopp, R. (Ed.): *Final report of the DFG-Priority Program 1074*

- Erweiterung der Formgebungsgrenzen bei Umformprozessen (Extension of process limit in forming processes), Verlagshaus Mainz GmbH, Aachen, pp. 184-191.
- Grellmann, W.; Seidler, S. (1998):* 'Deformation und Bruchverhalten von Kunststoffen', Springer-Verlag, Berlin, pp. 257-270.
- Haar, R. T. (1996):* 'Friction in sheet metal forming, the influence of local contact conditions and deformation', PhD-Thesis, University of Twente, Netherlands.
- Hama, T., Hatakeyama, T.; Asakawa, M. (2007):* 'Finite -element simulation of the elliptical cup deep drawing process by sheet hydro-forming', Finite Elements in Analysis and Design 43, pp. 234-246.
- Hatmann, S. (2001):* 'Numerical studies on the identification of the material parameters of Rivlin's hyperelasticity using tension-torsion tests', Acta Mechanica 148, pp. 129-155.
- Hasek, V.V.; Lange, K. (1980):* 'Grenzformänderungsschaubild und seine Anwendung bei Tiefzieh- und Streckziehvorgängen', Zeitschrift für industrielle Fertigung 70, pp. 575-580.
- Hattangady, N.V. (2003):* 'Automated modeling and remeshing in metal forming simulation', PhD-Thesis, Rensselaer Polytechnic Institute, Troy, New York.
- Hatanaka, K.; Fukui, M.; Mukai, Y.; Toyose, K. (1989):* 'Influence of drawing on organic coating adhesion property in aluminium', J. Jpn. Inst. Light Met. 39 (9), pp. 621-626.
- Hauptmann, R.; Doll, S.; Harnau, M.; Schweizerhof, K. (2001):* 'Solid-shell' elements with linear and quadratic shape functions at large deformations with nearly incompressible materials', Computers and Structures 79, pp. 1671-1685.
- Herold, U. (1984):* 'Verbesserung der Form- und Maßgenauigkeit kreiszylindrischer Werkstücke aus unterschiedlichen verfestigenden Werkstoffen durch hydromechanisches Tiefziehen', Dr.-Ing. Dissertation, Technische Universität Dortmund.
- Herrmann, M.; Richter, F. (2005):* 'Charakterisierung mechanischer Eigenschaften von Schichtsystemen und Oberflächen am Beispiel von Funktions- und Schutzschichten auf Kunststoffen', Neues Dresdner Vakuumtechnisches Kolloquium, Beschichtung und Modifizierung von Kunststoffoberflächen, Dresden, Tagungsband 15, pp. 145-149, ISBN 978-3-00-022604-5.
- He´tu, L.; Khandeparkar, T.; Wagner, S.; Liewald, M. (2006):* 'Hydromechanisches Tiefziehen von TWB's', wt-Werstatttechnik Online, Vol. 96, Heft 10, pp. 727-732.
- Hohlfelder, R.J. (1999):* 'Bulge and blister testing of thin film and their interface', PhD-Thesis, Stanford University, USA.
- Hora, P.; Tong, L. (2006):* 'Numerical prediction of FLDs using the enhanced maximum force criterion', FLC Zurich 2006, IVP, ETH Zurich, Switzerland.
- Homberg, W. (2000):* 'Untersuchungen zur Prozessführung und zum Fertigungssystem bei der Hochdruck-Blech-Umformung', Dr.-Ing. Dissertation, Technische Universität Dortmund.

- Lo, S.-W.; Hsu, T.-C.; Wilson, W.R.D. (1993): 'An analysis of the hemispherical-punch hydro forming process', Journal of Materials Processing Technology 37, pp. 225-239.*
- Hult, A.; Lange, J.; Luisier, A.; Schedin, E.; Ekstrand, G. (1999): 'Development of scratch tests for pre-painted metal sheet and the influence of paint properties on the scratch resistance', Journal of Material Processing Technology 86, pp. 300-305.*
- Hill, R. (1950): 'The mathematical theory of plasticity', London: Oxford Press.*
- Jänner, S. (2004): 'Organisch Beschichtetes Breitband, Technische Lieferbedingungen Kaltgewalztes und Oberflächenveredeltes Stahlband', colofer®, voestalpine GmbH.*
- Jäger, S. (2005): 'Untersuchung zum Umformen von Blechen und Rohren aus Magnesium AZ31', Dr.-Ing. Dissertation, Universität Stuttgart.*
- Jensen, M.R.; Olovsson, L.; Dankert, J. (2000): 'Numerical model for the oil pressure distribution in the hydro-mechanical deep drawing process', Journal of Materials Processing Technology 103, pp. 74-79.*
- Jensen, M.R.; Olovsson, L.; Dankert, J. (2001): 'Aspects of Finite Element Simulation of Axi-Symmetric Hydro-mechanical deep drawing', Journal of Manufacturing Science and Engineering, Vol. 123, pp. 411-415.*
- Jitsukawa, M.; Yamashita, M. (2003): 'Advanced coated steel sheets with excellent functions to satisfy ecological requirements', NKK Technical review, No. 88, pp. 58-72.*
- Keck, P.; Wilhelm, M.; Lange, K. (1990): 'Application of the finite element method to the simulation of sheet metal forming processes: Comparison of calculations and experiments', Inter. Journal for numerical methods in engineering, Vol. 30, pp. 1415-1430.*
- Keeler, S.P. (1965): 'Determination of forming limits in automotive stampings', Society of Automotive Engineers, Technical paper, No. 650535.*
- Kleiner, M. (2006): 'Abschlussbericht zum DFG Schwerpunktprogramm SPP 1098', 2000-2006, "Wirkmedienbasierte Fertigungstechniken zur Blechumformung", Technische Universität Dortmund.*
- Kleiner, M.; Schikorra, M. (2002): 'Forming limit curve for the prognosis of the surface quality of Coil-Coated products', Research project KI 619/12-1, Technische Universität Dortmund.*
- Kleiner, M.; Rogner, I. (2004): 'Substitution von Kunststoffen in der Scheinwerfermodulfertigung', Forschungsantrag, Institut für Umformtechnik und Leichtbau, Technische Universität Dortmund.*
- Khandeparkar, T. (2007): 'Hydro-mechanical deep drawing under the influence of high fluid pressure', PhD-Thesis, Institut für Umformtechnik, Universität Stuttgart.*
- Klocke, F.; Breuer, D.; Raedt, H.W. (2003): 'An advanced method to describe the forming limit of metals', SEM/NAMRI Trans., pp. 33-40.*

- Keßler, L. (1996):* 'Simulation der Umformung organisch beschichteter Feibleche und Verbundwerkstoffe mit der FEM', Dr.-Ing. Dissertation, Technische Universität Dortmund.
- Kim, H. Y. et al. (2002):* 'An experimental study on forming characteristics of pre-coated sheet metal', *Journal of Materials Processing Technology* 120, pp. 290-295.
- Kim, J.; Son, B.M.; Kang, B. S.; Hwang, S.M.; Park, H.J. (2004):* 'Comparison stamping and hydro-mechanical forming process for an automobile fuel tank using finite element method', *Journal of Material Processing Technology* 153, pp. 550-557.
- Kobayashi, S.; Oh, S.I.; Altan, T. (1989):* 'Metal forming and the finite-element method', Oxford University Press, New York, USA.
- Kopp, R.; Wiegels, H. (1999):* 'Einführung in die Umformtechnik', 2. Auflage, Verlag Mainz, Aachen.
- Langhammer, T. (2005):* 'Untersuchung zu neuen Konzepten für PKW-Kraftstoffbehälter', Dr.-Ing. Dissertation, Institut für Umformtechnik und Leichtbau, Technische Universität Dortmund.
- Lang, L.; Danckert, J.; Nielsen, K. B.; Kang, D.C.; Zhang, S.H. (2004a):* 'Key technologies of the simulation of the hydrodynamic deep drawing of irregular parts', *Journal of Materials Processing Technology* 150, Issues 1-2, pp. 40-47.
- Lang, L.; Danckert, J.; Nielsen, K. B. (2004b):* 'Investigation into the effect of pre-bulging during hydro-mechanical deep drawing with uniform pressure onto the blank', *International Journal of Machine Tools & Manufacture* 44, pp. 649-657.
- Lang, L.; Wang, Z.R.; Danckert, J.; Nielsen, K. B.; Kang, D.C.; Zhang, S.H.; Yuan, S.J. (2004c):* 'Hydro-forming highlights: sheet hydro-forming and tube hydro-forming', *Journal of Materials Processing Technology* 151, pp. 165-177.
- Lang, L.; Danckert, J.; Nielsen, K. B. (2005):* 'Multi-layer sheet hydro-forming: Experimental and numerical investigation into the very thin layer in the middle', *Journal of Materials Processing Technology* 170, pp. 524-535.
- Lang, L.; Danckert, J.; Nielsen, K. B.; Zhou, X. (2005a):* 'Investigation into the forming of a complex cup locally constrained by a round die on an innovative hydro-mechanical deep drawing method', *Journal of Material Processing Technology* 167, pp. 191-200.
- Lange, K. (1990):* 'Umformtechnik-Handbuch für Industrie und Wissenschaft', Band 3: Blechbearbeitung, Springer-Verlag, Berlin, ISBN 978-3-540-50039-1.
- Lawrenz, K.-J. (1978):* 'Untersuchungen zum Tiefziehverhalten organisch beschichteter Feibleche und die Prüfung dieser Verbundwerkstoffe', Dr.-Ing. Dissertation, Technische Universität Dortmund.
- Liang, Y.; Bi, X.; Wang, J. (2007):* 'Numerical simulation of laser-induced thin film delamination', *Thin Solid Film* 516, pp. 971-981.

- Ling, Y. (1996): 'Uniaxial true stress-strain after necking', AMP Journal of Technology Vol. 5, pp. 37-48.
- Li, K. P.; Cescotto, S. (1997): 'An 8-node brick element with mixed-formulation for large deformation analyses', Comput. Methods Appl. Mech. Engineering 141, pp. 157-204.
- Liechti, K.M.; Wu, J.-D. (2001): 'Mixed-mode, time-dependent rubber/metal debonding', Journal of the Mechanics and Physics of Solids 49, pp. 1039-1072.
- Mamalis, A.G.; Manolacos, D.E.; Baldoukas, A.K. (1996): 'On the Finite - Element modelling of the deep drawing of square sections of coated steels', Journal of Materials Processing Technology 58, pp. 153-159.
- Mamalis, A.G. (1997): 'Finite - Element modeling of the stretch forming of coated steels', Journal of Materials Processing Technology 68, pp. 71-75.
- Marc (2005): Marc/Mentat User's Manual, version 2005.
- Marciniak, Z.; Duncan, J.L. (1991): 'The mechanics of sheet metal forming', Butterworth-Heinemann, Oxford (GB), ISBN 0-7506-5300-0.
- Marciniak, Z.; Kuczynski, K. (1967): 'Limit strains in the process of stretch forming sheet metal', Int. J. Mech. Sci. 9, pp. 609-620.
- Mende, T. (2006): 'Clinchen von beschichteten Feinblechen unter besonderer Berücksichtigung des Einsatzes von Wirkmedien', Dr.-Ing. Dissertation, Technische Universität Dresden.
- Meuthen, B.; Jandel, A.-S. (2005): 'Coil Coating: Bandbeschichtung: Verfahren, Produkte und Märkte', 2. Auflage, Vieweg & Sohn Verlag, Wiesbaden.
- Mooney, M. (1940): 'A theory of large elastic deformation', J. appl. Phys. 11, pp. 582-592.
- Nakagawa, T.; Nakamura, K.; Amino, H. (1997): 'Various applications of hydraulic counter-pressure deep drawing', Journal of Material Processing Technology 71, pp. 160-167.
- Ogden, R.W. (1972): 'Large deformation isotropic elasticity – On the correlation of theory and experiment for incompressible rubber-like solid', Proc. R. Soc. Lond. A 326, pp. 565-584.
- Ogle, K.; Morel, S.; Meddahi, N. (2005): 'An electrochemical study on the delamination of polymer coating on galvanized steel', Corrosion science 47, pp. 2034-2052.
- Oppen, D. (1971): 'Problem der Metalloberflächenbehandlung im Hinblick auf die speziellen Qualitätsanforderungen bei kunststoffbeschichteten Bändern', Deutsche Forschungsgesellschaft für Blechbearbeitung und Oberflächenbehandlung e.V. pp. 49-52.
- Osakada, K. (2008): 'History of plasticity and metal forming analysis', 9th Inter. Conference on Technology and Plasticity, Gyeongju, Korea, pp. 22-43.
- Owen, D. R. J.; Pires, F.M.A.; Dutko, M. (2007): 'Computational strategies for polymer coated steel sheet forming simulation', Numiform '07, Proceedings of the 9th International

- Conference on Numerical Methods in Industrial Forming Processes. AIP Conference Proceedings, Volume 908, pp. 49-60.
- Palaniswamy, H.; Braedel, M.; Thandapani, A.; Altan, T. (2006): 'Optimal programming of Multi-point cushion system for sheet metal forming', Annals of the CIRP, Vol. 55, pp. 249-254.*
- Pepelnjak, T.; Kuzman, K. (2007): 'Numerical determination of the forming limit diagram', Journal of Achievements in Materials and Manufacturing Engineering, Vol. 20, pp. 375-378.*
- Polyakova, A.; Stepanov, E.V.; Provder, T.; Hiltner, A.; Baer, E. (2000): 'Relationship of coating failure to deformation in the deep drawn cup', The Journal of Adhesion 72, pp. 37-50.*
- Polyakova, A.; Hiltner, A.; Baer, E.; Provder, T. (2000a): 'Effect of formulation variables on coating properties and performance in the deep draw process', Journal of Coatings Technology, Vol. 72, No. 901, pp. 69-75.*
- Qi, H.J.; Boyce, M.C. (2005): 'Stress-strain behavior of thermoplastic polyurethanes', Mechanic of Materials 37, pp. 817-839.*
- Rivlin, R. S.; Saunders, D.W. (1951): 'Large elastic deformation of isotropic material', VII. Experiments on the deformation of rubber, Phil. Trans. R. Soc. A243, pp. 251-288.*
- Reddy, N.V.; Deep, K.S.; Agrawal, A.; Ramkumar, J. (2006): 'A mathematical model for determination of limiting blank holding force and cavity pressure in hydro-mechanical deep drawing', Pro. IMechE Vol. 221, Part B: Engineering Manufacture, pp. 155-162.*
- Roll, K. (1998): 'Stand der Blechumformung heute – Notwendige Weiterentwicklungen', Industriekolloquium SFB 362, pp. 129-132.*
- Sarkar, B., Jha, B.K., Mukerjee, D., Jha, S., Narasimhan, K. (2002): 'Thinning as a failure criterion during sheet metal forming', Journal of Failure Analysis and Prevention, Vol. 2, No. 2, pp. 63-65.*
- Schulze, B. (1994): 'Werkstoffkunde', 8. Überarb. Aufl., Springer-Verlag, Berlin.*
- Schikorra, M.; Hellinger, V.; Kleiner, M. (2002): 'Einsatz von Grenzformänderungsschaubild zur Bestimmung der Umformbarkeit von beschichteten Feinblechen', UTF Science 3, pp. 4-6.*
- Schreurs, P.J.G.; Van den Bosch, M.J.; Geers, M.G.D. (2005): 'Deformation limit of polymer coated metal sheet', 11th International Conference on Fracture, Turin, Italy, pp. 1-5.*
- Schreurs, P.J.G.; Van den Bosch, M.J.; Geers, M.G.D. (2009): 'On the prediction of delamination during deep-drawing of polymer coated metal sheet', Journal of Materials Processing and Technology 209, pp. 297-302.*
- Shah, R. L. (2006): 'Optimized upper bound analyses of polymer coated metal rod extrusion through conical die', Master thesis, Graduate studies of Texas A&M University, Texas, USA.*
- Siegert, K.; Aust, M. (2001): 'Tiefziehen von Blechformteilen bei extremen Hydraulischen Gegendrücken', Kolloquium Wirkmedien-Blechumformung, DFG Schwerpunktprogramm*

1098, Wirkmedienbasierte Fertigungstechniken zur Blechumformung, Dortmund, ISBN 3-00-008740-0, pp. 79-91.

Siegert, K.; Ziegler, M. (1998): 'Verfahren zum hydromechanischen Tiefziehen und zugehörige Einrichtung', Offenlegungsschrift DE 19724767, Int. Cl.6 B21 D22/22, Stuttgart.

Simha, R.; Papazoglou, E. (1989): 'Thermal expansively and bulk modulus of polymer composites: Experiment versus theory', Polymer Composites Vol. 10, No. 6, pp. 409-413.

Shi, M.F. (1991): 'Effect of strain gradient and curvature on forming limit diagrams for anisotropic sheets', J. mater. Shap. Tech. 9, pp. 253-268.

Slota, J.; Spijak, E. (2005): 'Comparison of the forming-limit diagram (FLD) models for drawing quality (DQ) steel sheets', Metalurgija 44, pp. 249-253.

Smith, K.B. (1999): 'Measuring of perception glossy surface', Pigment & Resin Technology, Vol. 28, No. 4, pp. 217-222.

Sowerby, R.; Duncan, J.L. (1971): 'Failure in sheet metal in biaxial tension', Int. J. Mech. Sci. 13, pp. 217-229.

Spathis, G.D. (1991): 'Polyurethane elastomers studied by the Mooney-Rivlin Equation for Rubbers', Journal of Applied Polymer Science, Vol. 43, pp. 613-620.

Spacek, J.; Smrcek, V.; Kosek, J. (1982): 'Werkzeug für hydromechanisches Tiefziehen, insbesondere von Ziehteilen ohne Flansch', Offenlegungsschrift DE 3151382, Int. Cl. 3 B21 D26/2, Prague.

Stojek, M.; Stommel, M.; Korte, W. (1998): 'FEM für die mechanische Auslegung von Kunststoff- und Elastomerbauteile', Springer-VDI-Verlag, Düsseldorf.

Strauß, B. (2008): 'Vorlackiertes Stahlband: Herstellung – Verarbeitung – Entwicklungstrends', 15. Sächsische Fachtagung Umformtechnik Dresden, SFU, pp. 141-154.

Strikos, I.; Jansen, S.; Schneider, W. (1999): 'Bildanalyse von lackierten Oberflächen', Farbe & Lack 105, pp. 241-244.

Sudo, M. (2005): 'Residual Stresses due to Deep-Drawing of Pre-Coated Aluminum-Alloy Sheets', Material Science Forums Vol. 490-491, pp. 358-363.

Takuda, H.; Mori, K.; Fujimoto, H.; Hatta, N. (1996): 'Prediction of forming limit in deep drawing of Fe/Al laminated composite sheet using ductile fracture criterion', Journal of Material Processing Technology 60, pp. 291-296.

Hama, T.; Hatakeyama, T.; Asakawa, M.; Amino, H.; Makinouchi, A.; Fujimoto, H.; Takuda, H. (2007): 'Finite-element simulation of the elliptical cup deep drawing process by sheet hydro-forming', Finite Elements in Analysis and Design 43, pp. 234-246.

Tang, S.C.; Chu, E.; Samanta, S.K. (1982): 'Finite element prediction of the deformed shape of an automotive body panel during preformed stage', Numerical methods in Industry forming process, Int. Conf. Proc. Swansea, pp. 629-640.

- Tekkaya, A. E. (2000):* 'State-of-the-art of simulation of sheet metal forming', *Journal of Materials Processing Technology* 103, pp.14-22.
- Tekkaya, A.E. (2002):* 'Sheet forming, Membrane theory', Vorlesung, Institut für Umformtechnik und Leichtbau, Technische Universität Dortmund.
- Van Tijum, R. (2006):* 'Interface and surface roughness of polymer-metal laminates', PhD-Thesis, University of Groningen, Netherlands.
- Toh, C.H.; Kobayashi, S. (1983):* 'Finite element process modeling of sheet metal forming of general shapes', *Grundlagen der Umformtechnik*, *Berichte aus dem Institut für Umformtechnik*, Band 74, Stuttgart, pp. 39-56.
- Thyssen (2003):* 'Bandbeschichtetes Feinblech PLATAL®/PLADUR®', Technical Report, ThyssenKrupp Stahl, Bestell-Nr. 2090.
- Thije, R.T. (2007):* 'Finite element simulations of laminated composite forming processes', PhD-Thesis, University of Twente, Netherlands.
- Treloar, L.R.K. (1958):* 'The physic of rubber elasticity', Oxford University Press, New York, USA.
- Traversin, M.; Kergen, R. (1995):* 'Close-loop control of the blank holder force in deep-drawing: finite element modeling of its effects and advantages', *Journal of Material Processing Technology* 50, pp. 306-317.
- Van Tyne, C. J.; Wichern, C.M.; De Cooman, B.C. (2005):* 'Surface roughness changes on hot-dipped galvanized sheet steel during deformation at low strain level', *Acta Materialia*, pp. 278-288.
- Uthaisangsuk, V.; Prahl, U.; Bleck, W.; Münstermann, S. (2007):* 'Experimental and numerical failure criterion for formability prediction in sheet metal forming', *Computational Materials Science* 39, pp. 315-323.
- Van der Aa, M. A. H.; P.J.G.; Baaijens, F.P.T. (2001):* 'Modeling of the wall ironing process of polymer coated sheet metal', *Mechanics of Materials* 33, pp. 555-572.
- Van der Aa, H.C.E.; Van der Aa, M.A.H.; Schreurs, P.J.G.; Baaijens, F.P.T.; Van Veenen, W.J. (2000):* 'An experimental and numerical study of the wall ironing process of polymer coated sheet metal', *Mechanic of Material* 32, pp. 423-443.
- Van den Bosch, M.J.; Schreurs, P.J.G.; Geers, M.G.D. (2007):* 'A cohesive zone model with a large displacement for interfacial fibrillation', *European Journal of Mechanics A/Solids* 26, 2007, pp. 1-19.
- Van den Bosch, M. J. (2007a):* 'Interfacial delamination in polymer coated metal sheet', PhD-Thesis, Eindhoven University of Technology, Netherlands.
- Van den Bosch, M.J.; Schreurs, P.J.G.; Geers, M.G.D. (2008):* 'Identification and characterization of delamination in polymer coated metal sheet', *Journal of the Mechanics and Physics of Solids* 56, pp. 3259-3276.

- Valenta, L.; Molnar, L. (2001): 'Vergleich des Neo-Hooke'schen und des Mooney-Rivlin'schen Materialmodells in der FEM-Berechnung', Periodica Polytechnica Ser. Mech. Eng. Vol. 45, No. 1, pp. 195-201.*
- Wang, J.; Vayeda, R. (2007): 'Adhesion of coating to sheet metal under plastic deformation', International Journal of Adhesion and Adhesives, Vol. 27, Issue 6, pp. 480-492.*
- Vogtenrath, G.; Klinge, M.; Von Laer, P. (1993): 'Herstellung, Eigenschaften und Anwendung von organisch beschichtetem Band und Blech', Stahl und Eisen 113, Nr. 5, pp. 91-98.*
- Wang, Z.; Nakamura, T. (2003): 'FEM analysis of contact mechanism in press-forming of lubricant pre-coated steel sheet', Journal of Materials Processing Technology, Vol. 140, pp. 514-519.*
- Wang, J.; Alexander, R.; Pauly, S. (2003-J): 'An experimental investigation of coating durability in forming pre-coated sheet metal', SME Trans XXXI, N Am Manuf. Res. Inst., pp. 57-63.*
- Wang, N.M.; Budiansky, B. (1978): 'Analysis of sheet metal forming by a Finite-element Method', Trans. ASME, I. Appl. Mech., Vol. 45, pp. 73-82.*
- Wagner, S.; Jäger, S.; Frank, H. (2001): 'Tiefziehen mit starren Werkzeug in Kombination mit einem nachfolgenden hydraulischen Tiefen', Proceeding of 1st Colloquium of the DFG Program SPP1098, 'Sheet metal forming with pressure medium', Dortmund, pp. 165-178.*
- Ward, I.M. (1983): 'Mechanical properties of solid polymers', 2nd edition, Wiley, New York, USA.*
- Wellendorf, A. (2003): 'Untersuchungen zum konventionellen und wirkmedienbasierten Umformen von komplexen Feinblechbauteilen', Dr.-Ing. Dissertation, Technische Universität Dortmund.*
- Williams, J.G.; Hadavinia, H. (2002): 'Analytical solutions for cohesive zone models', Journal of the Mechanics and Physics of Solids 50, pp. 809-825.*
- Wifi, A.S. (1976): 'An incremental complete solution of the stretch forming and deep drawing of a circular blank using a hemispherical punch', Int. J. Mech. Sci. 18, pp. 23-31.*
- Wolfhard, D.; Filthaut, C.; Rogner, I.; Shinkinger, B. (2003): Organisch vorbeschichtete Stahlfeinbleche für den Karosseriebau, ThyssenKrupp TechnoForum, Dezember 2003, pp. 14-19.*
- Xia, S.M.; Gao, Y.F.; Bower, A.F.; Lev, L.C.; Cheng, Y.-T. (2007): 'Delamination mechanism maps for a strong elastic coating on an elastic-plastic substrate subjected to contact loading', Inter. Journal of Solids and Structures 44, pp. 3685-3699.*
- Xu, S.; Weinmann, K.J.; Chandra, A. (1998): 'Analysis of forming limits using the hill 1993 yield criterion', J. Eng. Mater. Tech. 120, pp. 236-241.*

- Yossifon, S.; Tirosch, J. (1985): 'Rupture instability in hydro-forming deep –drawing process', Int. J. Mech. Sci, Vol. 27, No. 9, pp. 559-570.*
- Yadav, A. (2006): 'Processes for hydro-forming sheet metal', Part I: Sheet hydro-forming with a die, R&D Update, Stamping Journal, AN. FMA. Publication, February 2006, pp. 40-42.*
- Zhang, S.H.; Danckert, J. (1998): 'Development of hydro-mechanical deep drawing', Journal of Material Processing Technology 83, pp. 14-25.*
- Zhang, S.H.; Niesel, K.B.; Danckert, J.; Kang, D.C.; Lang, L.H. (2000): 'Finite element analysis of the hydro-mechanical deep drawing process of tapered rectangular boxes', Journal of Material Processing Technology 102, No. 1, pp. 1-8.*
- Zhang, S.H.; Jensen, M.R.; Niesel, K.B.; Danckert, J.; Kang, D.C.; Lang, L.H. (2000a): 'Analysis of the hydro-mechanical deep drawing of cylindrical cup', Journal of Material Processing Technology 103, pp. 367-373.*
- Zhang, S.H.; Jensen, M.R.; Niesel, K.B.; Danckert, J.; Kang, D.C.; Lang, L.H. (2003): 'Effect of anisotropy and pre-bulging on hydro-mechanical deep drawing of mild steel cups', Journal of Material Processing Technology 142, pp. 544-550.*
- Zhou, L. Q. (2006): 'Forming limits of electrodeposited nickel coating in the left region', Journal of Materials Engineering and Performance, Vol. 15, Issue 3, pp. 287-294.*
- Zwaag, S. V.D. (2007): 'Self healing materials', Springer-Verlag, Dordrecht, Netherlands ISBN 978-1-4020-6250-6 (e-book).*

Lebenslauf

Persönliche Daten

Name: Ha-Duong Pham
Geburtsdatum und -ort: 04. April 1978 in Hanoi, Vietnam
Familienstand: verheiratet
Staatsangehörigkeit: vietnamesisch

Ausbildung

1983 - 1988 Yen My Grundschule in Hanoi, Vietnam
1988 - 1992 Yen My Mittelschule in Hanoi, Vietnam
1992 - 1995 Ngoc Hoi Gymnasium in Hanoi, Vietnam
1995 - 2000 Maschinenbaustudium an der TU Hanoi, Vietnam
Vertiefungsrichtung: Umformtechnik
Abschluss: Diplom-Ingenieur
2000 - 2002 Masterstudium an der TU Hanoi
Vertiefungsrichtung: Umformtechnik
Abschluss: Master of Science

Berufliche Tätigkeiten

2000 - 2006 wissenschaftlicher Mitarbeiter am Lehrstuhl für Umformtechnik der Fakultät Maschinenwesen der TU Hanoi, Vietnam
03/2004 – 09/2004 Praktikum beim Forschung-Ingenieur-Zentrum BMW München, Abteilung für Technologie Lackierte Karosserie, TK – 533 Büro, BMW AG München, Bundesrepublik Deutschland
Seit 10/2006 Doktorand (DAAD-Stipendiat) am Institut für Umformtechnik und Leichtbau, TU Dortmund, Bundesrepublik Deutschland

Sonstiges

03/2006 – 09/2006 Deutsch-Kurs für DAAD-Stipendiaten beim Carl Duisberg Centrum, Dortmund, Bundesrepublik Deutschland